

Plasma Surface Interactions in LaB₆ Hollow Cathodes with Internal Xe Gas Discharge

Thesis by:

Pedro Pablo Guerrero Vela

In Partial Fulfillment of the Requirements for the Degree of
Doctor of Philosophy in Space Engineering

The logo for the California Institute of Technology (Caltech), featuring the word "Caltech" in a bold, orange, sans-serif font.

CALIFORNIA INSTITUTE OF TECHNOLOGY

Pasadena, California

2019

Defended on May 8th, 2019

© 2019

Pedro Pablo Guerrero Vela
ORCID: 0000-0001-5766-2038

All rights reserved

ACKNOWLEDGEMENTS

First and foremost, I would like to express my deepest gratitude to my advisor at JPL Dr. James E. Polk for giving me the opportunity to work in the exciting field of electric propulsion technologies and for his continuous support and guidance throughout the entirety of my PhD work.

I would also like to thank my Caltech advisors Prof. Joanna M. Austin and Prof. Daniel I. Meiron for their advice and guidance, Prof. Dale I. Pullin and Prof. Joseph E. Shepherd for their valuable feedback as part of my candidacy and thesis defense committees, and Prof. Michael Ortiz and Prof. Pilar Ariza for providing me the life changing opportunity to be part of the Caltech community.

Given the multidisciplinary nature of electric propulsion technologies, collaborations with scientists from other fields have been essential to obtain fruitful results for this work. I am thankful to the following individuals who assisted me in this project and/or kindly helped by providing me with their expertise: Prof. Katherine Faber, Prof. Rosa Carmina Monreal, Prof. Michael Trenary, Prof. William A. Goddard, Prof. Kimberly A. See, Dr. Chi Ma, Benjamin Herren, Dr. Matthias Richer, Ellen Yan and Dr. Channing C. Ahn.

A special mention goes to the JPL staff without whom this work and my experience would not have been the same: Dr. Dan Goebel, Dr. Yiangos Mikellides, Dr. Alejandro Lopez Ortega, Dr. Lee Johnson, Dr. Richard Hofer, Dr. John Brophy, Dr. Ira Katz, Dr. Colleen Marrese-Reading, Dr. Robert Lobbia, Dr. Vernon Chaplin, Dr. Ryan Conversano, Giulia Becatti, Ray Swindlehurst and Nowell Niblett.

I thank all the staff at Galcit, especially Dimity Nelson, Denise Ruiz, Christine Ramirez and Lydia Suarez, for their administrative support, and the Caltech International Student Program personnel, specifically Laura Flower Kim and Daniel Yoder, for their timely and invaluable help with international student affairs. I am also grateful to the Caltech library personnel, the DocuServe group and specifically Dr. Donna T. Wrublewski for their assistance in finding relevant

literature for my research.

I also acknowledge the financial support of the joint NASA-GRC and JPL development of the HERMeS Hall thruster by NASA's Space Technology Mission Directorate through the Solar Electric Propulsion Technology Demonstration Mission project.

Finally, I want to emphasize how lucky I feel for having the endless support of my friends and family. It has been a long path to the completion of my PhD work and I am grateful for your encouragement throughout this journey. Thanks to all of you!

ABSTRACT

The ultimate goals of space vehicles are to move faster, further, and more reliably in the space environment. Electric propulsion (EP) has proven to be a necessary technology in the exploration of our solar system ever since its working principle was empirically tested in space in 1964. Thanks to the high exhaust velocities of ionized propellant gases, EP enables efficient utilization of the limited supply of propellant aboard spacecrafts. This technology has opened the possibility of long distance autonomous space missions.

EP devices require electron sources to ionize the propellant gas and to neutralize charges that are leaving the spacecraft. In modern EP thrusters, this is achieved by the use of hollow cathodes – complex devices that employ low work function materials to emit electrons. Hollow cathodes using polycrystalline LaB₆ inserts are attractive candidates for long duration EP based space missions. However, the physics behind LaB₆ hollow cathode operation has not been studied in detail, which limits the possibility of their optimization. This work presents an integrated experimental and computational approach to investigate LaB₆ hollow cathode thermal behaviour and the interplay between LaB₆ insert surface chemistry and xenon plasma.

Our investigation of the thermal behaviour of LaB₆ cathodes led to the unexpected discovery of a thermal transient when a new insert is first used. Specifically, we observed that the cathode temperature decreases by approximately 300 degrees over 50 hours before reaching steady state. This finding suggests a beneficial dynamic evolution of the cathode’s chemical state when it interacts with its own plasma. This evolution is intrinsic to cathode operation and can only be precisely understood when the multiphysic nature of the cathode is self-consistently simulated. Thus, we built a numerical platform capable of combining the plasma, thermal and chemical behavior of a discharging hollow cathode. Simulations incorporating different neutralization models, inelastic ion-surface interaction and heterogeneous chemical evolution led to two major conclusions. First, simulations predicted a significant reduction of the LaB₆

work function (0.42 eV) compared to previously reported baseline values, which is of paramount importance for EP thruster efficiency and operational lifetimes. Second, simulations suggested that the interaction between xenon low energy ions (< 50 eV) and the LaB_6 surface occurs following a two step neutralization mechanism. The predicted work function reduction was experimentally confirmed by photoemission spectroscopy. Furthermore, using a combination of crystallographic analysis, scanning electron microscopy and profilometry, we demonstrated that work function reduction is caused by the creation of a crystallographic texture at the LaB_6 surface upon interaction with Xe plasma. In addition, we postulated the existence of a work function enhancing mechanism of secondary importance, which can be explained by forced cationic termination of plasma exposed crystals.

Our results revealed the unexpected phenomenon of work function reduction upon plasma exposure of LaB_6 . These findings suggest that LaB_6 hollow cathodes may outperform current technologies and become the component of choice in EP thrusters for future space missions.

PUBLISHED CONTENT AND CONTRIBUTIONS

Guerrero, P., Polk, J.E., et al. (2017). "Work function reduction in lanthanum hexaboride hollow cathodes operated in gas discharges". In: *35th International Electric Propulsion Conference*. (Atlanta, GA, USA). IEPC-2017-399 URL: http://erps.spacegrant.org/IEPC_2017/IEPC_2017_399.pdf . Journal paper in preparation.

P.G. contributed to the conception of this work, design and development of the experimental setup, execution of the experiments, data analysis, writing of the manuscript, and preparation of figures.

Guerrero, P., Mikellides, I.G., et al. (2018). "Hollow cathode thermal modelling and self-consistent plasma solution: work function evaluation for a LaB₆ cathode.". In: *53rd AIAA/SAE/ASEE Joint Propulsion Conference*. (Cincinnati, OH, USA). DOI: 10.2514/6.2018-4511

P.G. contributed to the conception of this work, design and development of the experimental setup, execution of the experiments, data analysis, writing of the manuscript, and preparation of figures.

Guerrero, P., Mikellides, I.G., et al. (2019). "Hollow cathode thermal modelling and self-consistent plasma solution: two step neutralization modelling.". In: *36th International Electric Propulsion Conference*. (Vienna, Austria). Journal paper in preparation.

P.G. contributed to the conception of this work, design and development of the experimental setup, execution of the experiments, data analysis, writing of the manuscript, and preparation of figures.

Guerrero, P., Polk, J.E., et al. (2019). "LaB₆ hollow cathode work function enhancement: insight into the chemical processes.". In: *36th International Electric Propulsion Conference*. (Vienna, Austria). Journal paper in preparation.

P.G. contributed to the conception of this work, design and development of the experimental setup, execution of the experiments, data analysis, writing of the manuscript, and preparation of figures.

Mikellides, I.G., Goebel, D.M., Jorns, B.A., Polk, J.E., **Guerrero, P.** (2015). "Numerical Simulations of the Partially Ionized Gas in a 100-A LaB₆ Hollow Cathode". In: *IEEE Transactions on Plasma Science* 1 (43), pp. 173-184. DOI: 10.1109/TPS.2014.2320876

P.G. contributed to the design and development of the temperature measurement experimental setup, execution of the experiments and data analysis.

Polk, J.E., Goebel, D.M., **Guerrero, P.** (2015). "Thermal Characteristics of a Lanthanum Hexaboride Hollow Cathode". In: *34th International Electric Propulsion Conference. (Kobe, Japan)*. IEPC-2015-44 URL: http://erps.spacegrant.org/uploads/images/2015Presentations/IEPC-2015-44_ISTS-2015-b-44.pdf

P.G. contributed to the design and development of the temperature measurement experimental setup, execution of the experiments and data analysis.

Yanes, N.J., **Guerrero, P.**, Friss, A.J., Polk, J.E., Jorns, B.A., Austin, J. (2016). "Ion Acoustic Turbulence and Ion Energy Measurements in the Plume of the HERMeS Thruster Hollow Cathode.". In: *52nd AIAA/SAE/ASEE Joint Propulsion Conference. (Salt Lake City, UT, USA)*. DOI: 10.2514/6.2016-5028

P.G. contributed to the conception of this work, design and development of the experimental setup and execution of the experiments.

Mikellides, I.G., **Guerrero, P.**, Ortega, A.L., Goebel, D.M., Polk, J.E. (2018). "Spot-to-plume Mode Transition Investigations in the HERMeS Hollow Cathode Discharge Using Coupled 2-D Axisymmetric Plasma-Thermal Simulations". In: *53rd AIAA/SAE/ASEE Joint Propulsion Conference. (Cincinnati, OH, USA)*. DOI: 10.2514/6.2018-4722

P.G. contributed to the conception of this work.

Polk, J.E., Lobbia, R., Barriault, A., **Guerrero, P.**, Mikellides, I.G., Ortega, A.L. (2017). "Inner Front Pole Cover Erosion in the 12.5 kW HERMeS Hall Thruster Over a Range of Operating Conditions". In: *35th International Electric Propulsion Conference. (Atlanta, GA, USA)*. IEPC-2017-409 URL: https://iepc2017.org/sites/default/files/speaker-papers/iepc2017sla_measurements_final_0.pdf .

P.G. contributed to the conception of this work, design and development of the

cathode experimental setup and execution of the experiments.

Becatti, G., Goebel, D.M., Polk, J.E., **Guerrero, P.** (2017). "Life Evaluation of a Lanthanum Hexaboride Hollow Cathode". In: *Journal of Propulsion and Power* 4 (34), pp. 893-900. DOI: 10.2514/1.B36659

P.G. contributed to the conception of this work.

2.5.3.1	Work function estimation, method 1: Matching net J_D	37
2.5.3.2	Work function estimation, method 2: Minimization of $\text{sum}(\text{abs}(J_D(\phi) - J_{D, \text{measured}}))$ per orifice. . .	38
2.5.4	Measured work functions	38
2.5.5	Work function reduction mechanism	44
2.5.5.1	Lanthanum recycling hypothesis	44
2.5.5.2	Crystallographic texture hypothesis	49
2.5.5.3	Chemical enhancement hypothesis	49
2.6	Conclusions	50
2.7	Appendix: Validation of the temperature measurements	53
2.7.1	Thermocouple accuracy and stability	53
2.7.2	Thermocouple installation impact on the thermal characteristics of the insert.	54
	Bibliography	57
	Chapter III: Hollow cathode thermal modelling and self-consistent plasma solution; work function evaluation for a LaB_6 cathode and two step neutralization modelling.	60
3.1	Abstract	60
3.2	Introduction	61
3.3	Methods	68
3.3.1	Overview of the coupled self-consistent simulation approach	68
3.3.2	Hollow cathode thermal model	70
3.3.2.1	Geometry and materials	70
3.3.2.2	Thermal modelling	71
3.3.2.3	Thermal fluxes – the interface with the plasma solver	73
3.3.3	Thermal model validation	74
3.3.4	Hollow cathode plasma model (text by Dr. Yiangos Mikellides, coauthor in the paper.)	78
3.3.5	Plasma model validation (text by Dr. Yiangos Mikellides, coauthor in the paper.)	84
3.3.6	Heat flux model	88
3.3.6.1	Energy accommodation coefficient	89
3.3.6.2	Neutralization model	91
3.3.7	Iterative solution (text by Dr. Yiangos Mikellides, coauthor in the paper.)	92
3.4	Results	93
3.4.1	Baseline thermal model, $\alpha_{\text{EAC}}^0 = 1$, one step neutralization	93
3.4.2	Sensitivity to errors in plasma model results	95
3.4.3	Sensitivity to thermal model assumptions	96

3.4.4	Sensitivity to plasma model parameters	98
3.4.5	Sensitivity to energy accommodation coefficient	99
3.4.6	Sensitivity to work function distribution	100
3.4.7	Sensitivity to neutralization model	102
3.5	Discussion	102
	Bibliography	107
	Chapter IV: LaB ₆ hollow cathode work function enhancement: insight into the chemical processes.	112
4.1	Abstract	112
4.2	Introduction	113
4.3	Methods	117
4.3.1	Test article and facility – insert, cathode and chamber	118
4.3.2	Operating conditions	118
4.3.3	Surface morphology characterization – scanning electron microscopy (SEM) and profilometry	120
4.3.4	Direct work function measurement – ultraviolet photoelectron spectroscopy	122
4.3.5	Phase identification – X-ray powder diffraction and electron backscatter diffraction	123
4.3.6	Crystallographic texturing – X-ray powder diffraction	125
4.4	Results	125
4.4.1	Cathode operating conditions	125
4.4.2	Morphology identification – scanning electron microscopy (SEM)	126
4.4.3	Topology characterization – profilometry	129
4.4.4	Direct Work function measurement – ultraviolet photoelectron spectroscopy	133
4.4.5	X-ray powder diffraction results	133
4.4.6	Electron backscatter diffraction results	133
4.5	Discussion	133
4.6	Conclusions	145
	Bibliography	149
	Chapter V: Conclusions and future work	150
5.1	Conclusions	150
5.2	Future work	152

LIST OF ILLUSTRATIONS

<i>Number</i>	<i>Page</i>
1.1 Implications of the rocket equation	3
1.2 LaB ₆ crystal structure.	7
1.3 LaB ₆ phase diagram.	8
1.4 Work function of different LaB ₆ crystal faces computed from DFT simulations.	10
2.1 LaB ₆ hollow cathode schematic	24
2.2 Insert finite element model with three thermocouples wells	25
2.3 Thermal transient for a new insert with the nominal orifice	27
2.4 Thermal transient with the nominal orifice after exposing the cathode to the atmosphere for several hours	28
2.5 Thermal transient associated with hot reignition	29
2.6 Thermal transient evolution with discharge current	30
2.7 Abnormal thermal transient after a hot reignition	31
2.8 Detail of the contaminant deposited on the inside of the insert	32
2.9 Steady state temperature distribution for each cathode configuration and each thermocouple	33
2.10 Temperature profiles approximated by a second degree polynomial fit to the thermocouple data for each operating condition	35
2.11 Cathode effective emitting area sensitivity analysis	36
2.12 Estimated work function with temperature data	39
2.13 $J_D(\phi_{\text{opt}}) - J_{D,\text{measured}}$, zero return current and $\phi_{\text{Schottky}} = 0$ eV	40
2.14 Work function as a function of depth measured at three different positions along the insert inner surface	42
2.15 Insert piece inside the KRATOS Ultra XPS at Caltech	42
2.16 Carbon atomic abundance on the insert	43
2.17 Mean free path estimation for boron and lanthanum in the insert region	47

2.18	OrCa2D simulation results for the plasma potential along the cathode centerline	48
2.19	Thermal transient and inferred work function for a new insert	51
2.20	Thermal heat fluxes along the insert of the cathode	54
2.21	Spring loaded thermocouple assembly	56
3.1	Thermionic emission sensitivity analysis for Richardson-Dushman law	64
3.2	Self-consistent platform overview	69
3.3	Temperature distribution created with COMSOL (example)	70
3.4	Ta total hemispherical emissivity	71
3.5	Cathode geometry	72
3.6	Axisymmetric model of the hollow cathode	72
3.7	Dependence of the maximum temperature of the insert surface with the total number of elements in the Comsol thermal model	74
3.8	Dependence of the maximum temperature of the insert surface with the number of azimuthal sectors used in the COMSOL thermal model	75
3.9	Dependence of the maximum temperature of the insert surface with the radiation resolution used in the Comsol thermal model	76
3.10	Representation of the cathode thermal model, plasma and surfaces at the interface	77
3.11	Location where the thermocouples were installed	78
3.12	COMSOL thermal model validation results	79
3.13	Schematic of the computational domain used in the OrCa2D simulations	80
3.14	OrCa2D numerical simulation domain	81
3.15	Steady-state solution for the plasma potential, electron temperature and neutral gas density	84
3.16	Comparison of a LaB6 hollow cathode operating at 100 A and 12 sccm with a BaO cathode operating at 13.3 A and 3.7 sccm. OrCa2D simulation results.	86
3.17	Comparison of the electron number densities along the centerline of the two cathodes between theory and experiment.	87
3.18	Comparison of the plasma potential and electron temperature along the centerline of the 100-A LaB6 cathode.	87

3.19	EAC as a function of ion-surface mass ratio and ion energy.	90
3.20	Evolution of the temperature input to OrCa2D and output from COMSOL	94
3.21	Converged temperature results for the <i>baseline</i> thermal model. . .	95
3.22	COMSOL thermal model validation results	97
3.23	Converged temperature results, thermal model sensitivity analysis	98
3.24	Converged temperature results, sensitivity analysis for V_K	99
3.25	Converged temperature results, sensitivity analysis for EAC	100
3.26	Work function profiles studied in this work	101
3.27	Converged temperature results, sensitivity analysis for work function distributions	102
3.28	Converged temperature results, sensitivity analysis for EAC and neutralization model	103
3.29	Contribution of the Schottky effect for the final self consistent solutions.	105
4.1	Modified insert geometry used in this study	118
4.2	Vacuum chamber used in the experiment	119
4.3	Cathode assembly inside vacuum chamber	120
4.4	Test sample (part A)	121
4.5	UPS spectra for the LaB ₆ test article after plasma exposure.	123
4.6	Thermal transient for a new, two part insert	127
4.7	Thermal transient during shut down	127
4.8	Part 1: cathode operational parameters measured during 50 hr test	128
4.9	Part 2: cathode operational parameters measured during 50 hr test	128
4.10	Test sample (part B) after the 50 hr test	129
4.11	On the left, SEM image collected from a sample after manufacturing. On the right, SEM pictures from the test sample after exposure to plasma	130
4.12	Surface profiles acquired before plasma exposure	131
4.13	Surface profiles acquired after plasma exposure	132
4.14	Work function measurements acquired with UPS	134
4.15	Test sample XRD spectra results, comparison with LaB ₄	135
4.16	Test sample XRD spectra results, comparison with LaB ₆	136

4.17	EBSD phase identification map of the sample in the upstream and downstream location of the test sample	137
4.18	SEM picture of the test sample at the downstream end	141
4.19	Test sample XRD spectra results. Intensity comparison	142
4.20	Idealized surface morphology for effective emissive area estimation	145
4.21	Test sample profile after plasma exposure along line 3	146

LIST OF TABLES

<i>Number</i>		<i>Page</i>
3.1	Summary: cathode parts and materials	72
4.1	XRD diffraction peak location analysis	140
4.2	XRD diffraction peak intensity analysis	143

NOMENCLATURE

§§§

\bar{z}	Dimensional coordinate along centerline of the cathode
\dot{m}_{Xe}	Xenon mass flow rate
ϕ	Work function
ϕ_{Schottky}	Modification of the work function due to the Schottky effect
ε	Total hemispherical emissivity
D	Richardson-Dushman law constant
e	Electron charge
J_{D}	Net discharge current
j_{ther}	Thermionic emission density
k_{B}	Boltzmann constant
T	Temperature
$T_{\text{insert}}(z)$	Temperature distribution along the hollow cathode insert
V_{D}	Discharge voltage
V_{K}	Keeper voltage
DFT	Density functional theory
EBSD	Electron back scatter diffraction
EP	Electric propulsion
HIP	Hot isostatic pressing
IAT	Ion acoustic turbulence
MPD	Magnetoplasmadynamic
SEM	Scanning electron microscope
XRD	X-ray powder diffraction

Chapter 1

INTRODUCTION

Exploration beyond the boundaries of Earth has captured human imagination since ancient times. With billions of galaxies in the observable universe, space offers a wealth of discoveries, opportunities, and resources. Technological advances in the 20th century have allowed humans for the first time in history to pioneer space exploration. However, in order to travel further in space, more progress has to be made in propulsion technology.

In order to cover the vast distances between objects in space, it is necessary to use a propulsion system that efficiently utilises the limited supply of propellant aboard the spacecraft while maintaining reasonable flight times (human time scales). Efficiency, in this context, means the maximal utilization of the propellant mass available for thrust purposes. The energetic requirements necessary to complete a space mission are specified by the quantity Delta- V . Therefore, a propulsion system is more efficient when it can obtain a given Delta- V with less propellant. The ideal rocket equation, first derived by mathematician William Moore in 1813, describes the motion of vehicles in space (see Fig. 1.1). It shows that the propellant has to be ejected from the vehicle at the highest possible speed in order to optimize its use.

Conventional chemical propulsion is limited by the amount of energy released in the combustion reaction. The maximum exhaust velocities that can be achieved with known fuels and oxidizers are only a few km/s. Therefore, this technology is considered “energy-limited”. However, given that propellants are their own energy source, the power supplied to the propellant is independent of the mass of the vehicle. This enables very high thrust-to-weight ratios to be attained.

In order to enable space missions with high Delta- V , such as the Dawn mission to Vesta ($\Delta V \simeq 11$ km/s [1]), the limitations of chemical propulsion need to be overcome. Electric propulsion (EP) was envisioned as a solution for high Delta- V

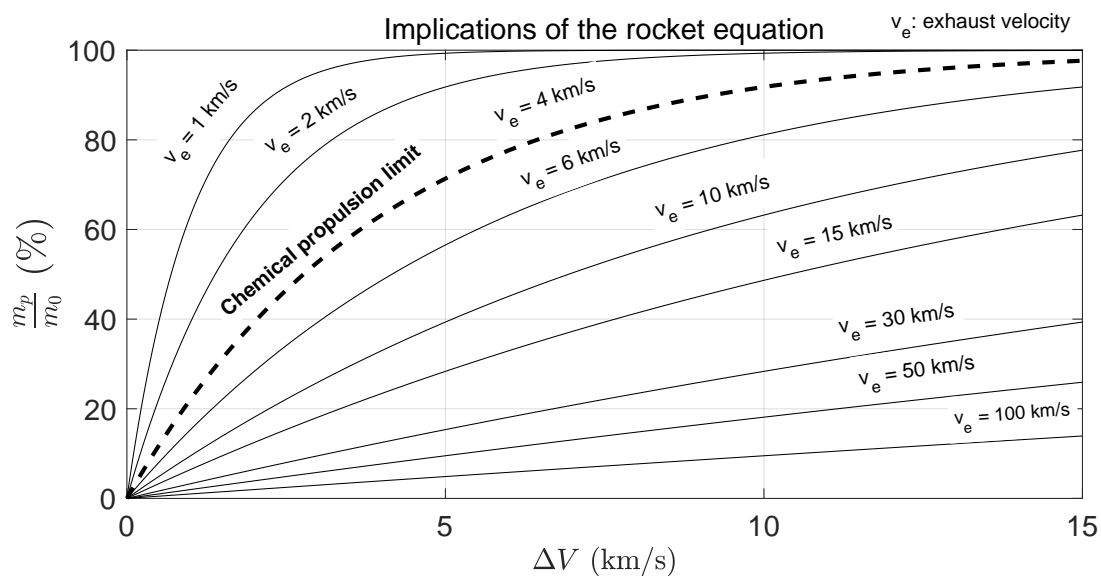


Figure 1.1: Implications of the rocket equation. m_p is the propellant mass, m_0 is the initial mass of the vehicle.

missions in the first half of the 20th century and later demonstrated in space in 1964 [2, 3]. EP is not “energy-limited” – an arbitrarily large amount of energy can be used to accelerate the propellant, thus, much higher exhaust velocities than with chemical propulsion can be obtained. In the Dawn mission, the ion propulsion system accelerated xenon propellant to approximately 30 km/s. However, EP requires an external power source and power processing units (PPU) to deliver energy to the propellant. PPUs are heavy pieces of equipment. Thus, increasing the power deposited to the propellant requires an increase of the mass of the vehicle. This requirement makes EP “power-limited.” Space vehicles equipped with EP thrusters typically have low thrust-to-weight ratios and therefore, they are low acceleration vehicles. EP enables space missions that are otherwise unrealistic, however the major drawback of its usage is long flight times. In the case of Dawn, the maximum thrust attainable was only 91 mN and therefore a long burn time of about 2 000 Earth days ($\sim 50\,000$ hr) was required to complete the mission. Electric thruster components must endure the long flight times required to accomplish the ever more demanding space missions. With tens of kilo-hours as a usual target,

component lifetime is one of the most important parameters to take into account when designing electric thrusters.

1.1 Electric propulsion overview

In EP, propellant gases are accelerated by direct electric heating and/or electromagnetic body forces. Conceptually, EP is divided into three categories – electrothermal, electrostatic and electromagnetic propulsion systems. This division is based on the different physical mechanisms used to accelerate the propellant. The most widely used electric thrusters are electrothermal (arcjets and resistojets). Pulsed magnetoplasmadynamic (MPD) thrusters have only flown on a few technology demonstrator missions and are still in the laboratory development phase. Hall-effect thrusters and gridded ion thrusters are electromagnetic propulsion systems that have been under development since the 1960s. Today, increasing numbers of commercial companies are developing Hall and ion thrusters, and only these two have been used for deep space missions.

In order to produce thrust, most EP devices need to ionize the propellant gas and accelerate the resultant ions by applying an electric field or a combination of electric and magnetic field. The ions are then ejected at very high speeds out of the spacecraft, forming the thruster plume. As the ions leave the thruster, charges accumulate in the space vehicle. These charges need to be neutralized, otherwise the spacecraft would continuously charge and attract the ions back with increasing strength, ultimately rendering zero thrust. Cathodes are fundamental components of these EP systems. First, they provide the electrons necessary to ionize the propellant, and second they are responsible for neutralizing the plume. Therefore, advancing cathode technologies are of central interest for the research community in EP and the motivation for this work.

1.2 Review of cathode technologies

In the early days of electric propulsion, cathodes were made of directly heated filaments of refractory metals, mainly tungsten. When heated, these metals emit

electrons thermionically. Thermionic emission for a given material is determined by the amount of energy required to extract electrons – a property termed “work function.” Due to the relatively high work function of these metals (e.g. 4.55 eV for tungsten), filament cathodes required working temperatures of up to 2600 K [4]. These high operating temperatures however led to rapid evaporation of the cathode material, limiting filament cathode lifetimes. Additionally, in order to reach the required emission temperature, the filaments were directly heated by passing current through them. This was achieved by mounting the filament in an open configuration which exposed the emitting material to high energy ions, thus further impacting the cathode lifetime because of sputtering – a wear mechanism based on the ejection of material due to the interaction of its surface with high energy particles. Collectively, the high operating temperature and sputtering permitted only hundreds of hours of available operation for this primitive cathode design.

To address the short lifetime of filament cathodes, the hollow cathode design was created. In this design electrons are emitted by a so-called emitter, which is enclosed and protected by an orifice plate and a keeper (see section 2.2). Electrons flow from the emitter to the thruster discharge or plume with a relatively low potential drop because a high conductivity plasma is created inside and outside the cathode. The cathode plasma extends outwards until it merges with the thruster plasma, thus creating a suitable medium for charges to move between cathode and thruster. The closed hollow cathode architecture presents several key improvements with respect to the primitive filament cathode approach. First, it creates the cathode plasma efficiently, which is important for electron transport. Second, continuous emission is only possible thanks to a carefully designed thermal architecture coupled with low work function emitters, which makes them energetically efficient and improves the thruster energy demand as a whole. Finally, hollow cathodes are very compact because their emission is not controlled by space-charge limitations. This characteristic is highly desirable as it enables very high current densities to be extracted from the cathode with yet small overall size.

Many advanced materials have been developed and improved over the years to be used as thermionic emitters in hollow cathodes. Low work function materials

allow abundant electron emission per gram of material evaporated, thereby extending the lifetime of the cathode. Thus, the most important feature for a cathode emitter is to have low work function. Furthermore, a key characteristic of hollow cathodes is that they are self-heating devices, i.e. the emitting surfaces of the cathode are heated by the internal plasma and do not require an external heat source. From a practical standpoint, this can only be achieved with materials that require relatively low operating temperatures to emit electrons. Thus, low work function materials also enable the self-heating property of hollow cathodes. The ideal emitter material also needs to be resistant to contamination from impurities in the propellant gas or feed system. Emitters whose efficiency is influenced by small amounts of contaminants in the propellant gas are not desirable.

Hollow cathodes can be grouped into two categories based on the technology of the emitter material: composite and bulk emitters, also known as dispenser and crystalline cathodes respectively. Composite emitters are based on low work function surfaces created with electronegative adatoms deposited on an appropriate substrate. The adatoms form a dipole at the surface which reduces the energy required for electrons to be emitted thermionically. Composite cathodes use compounds with extremely low work functions. One of the best known composite cathodes is the BaO-W cathode, widely used in space applications. However, a major disadvantage of these systems is the limited amount of substance that can be held by the substrate. Bulk cathodes use single crystals or polycrystalline materials that exhibit low work function. The main advantage of crystalline cathodes is the abundance of material available for emission. As the surface of the emitter evaporates away, the newly exposed surface exhibits the same emission profile. The most widely used material in bulk cathode technologies is polycrystalline LaB₆.

1.3 Properties of LaB₆

Boron-based materials have been studied since the 1950s due to their excellent chemical bonding, crystal structure and phonon and electron conduction properties [5]. The first experimental use of LaB₆ as an effective thermionic emitter is commonly attributed to Lafferty [6], who estimated a polycrystalline work function value of

2.66 eV. Many uses for LaB₆ as a cathode material have been found since, including but not limited to X-ray sources, electron beam pumped lasers, thermionic energy converters, ion beam sources, halogen atomic beam detectors, negative ion surface ionizers, scanning electron microscopes, transmission microscopes, electron probes, scanning Auger systems and electron lithography systems.

LaB₆ is a refractory ceramic material characterized by high melting point (2988 K [7]), strength, chemical and thermal stability, low vapor pressure, electronic work function, resistivity, thermal expansion coefficient, and high current and voltage capabilities, among other properties. The crystal structure of LaB₆ is simple cubic with octahedral space group $Pm\bar{3}m$ and central La cations (Fig. 1.2). The lattice parameter (number 1 in Fig. 1.2) is 4.1569 Å, the intraoctahedral parameter is 1.766 Å (2) and the interoctahedral parameter is 1.659 Å (3) [8]. The phase diagram can be found in Fig. 1.3.

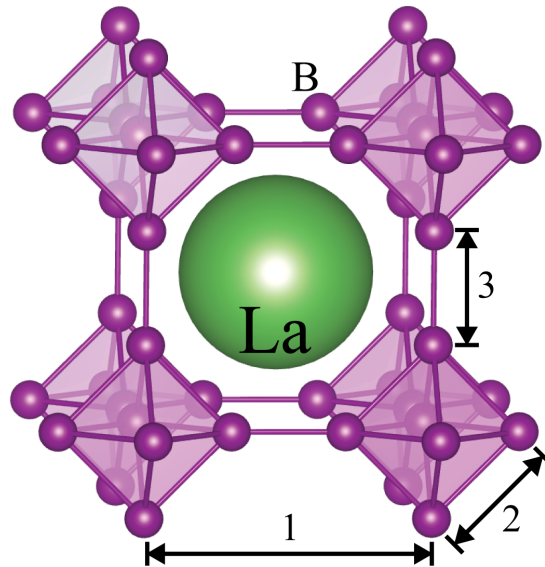


Figure 1.2: LaB₆ crystal structure. Image produced with VESTA [9] using data from [10].

The excellent thermionic behavior of LaB₆ is due to its surface structure, which in turn derives from the bulk structure. Per unit cell, LaB₆ contains one La atom and one B₆ octahedron unit. Boron atoms in the B₆ units are bonded with

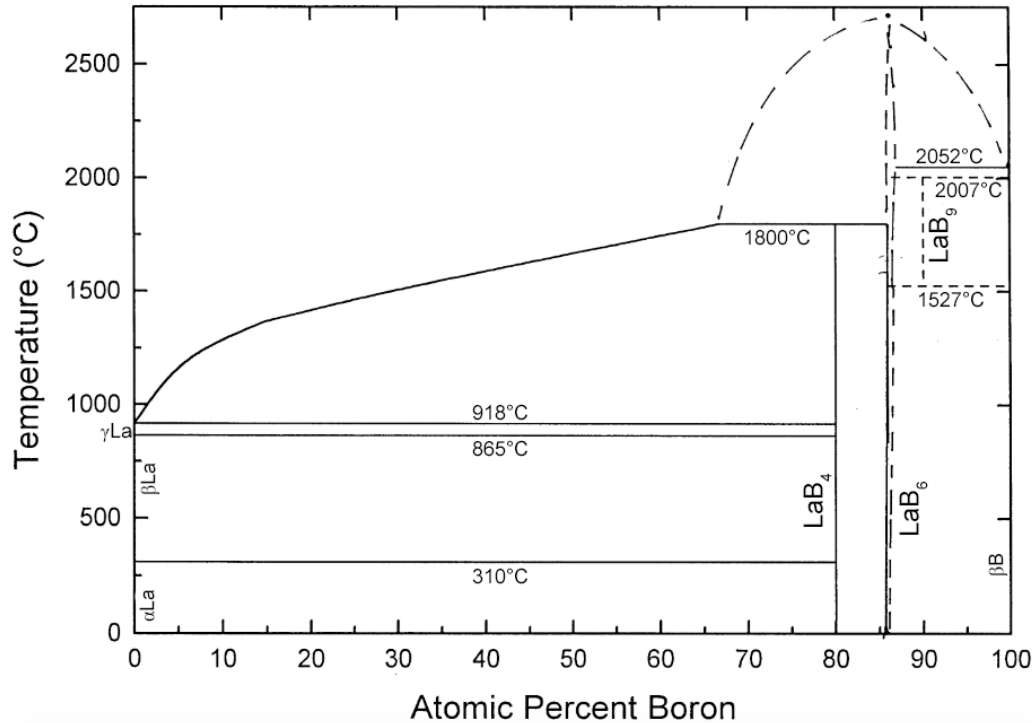


Figure 1.3: LaB₆ phase diagram. Reprinted with permission from the copyright holder [11]. Adapted.

intraoctahedral covalent bonds. Each B₆ unit is bonded to adjacent cells B₆ units covalently as well. This boron network is electron deficient, a situation that gets resolved with the transfer of 2 electrons per unit cell from the La atoms [12, 13]. The third electron of the trivalent metal atoms enters into a metallic conduction band that bonds La atoms between each other metallically. LaB₆ contains covalent B-B bonds, ionic La-B bonds and metallic La-La bonds [14] and this peculiar network of bonds is responsible for the unique set of macroscopic properties of the material.

Polycrystalline LaB₆ has an estimated work function of 2.66 eV [6]. Polycrystalline materials have complex surfaces composed of different crystals, with individual crystals exhibiting different work functions. In the case of LaB₆, the work functions of a selection of crystals have been reported [15], see Fig. 1.4. Furthermore, the topmost atomic layer of crystalline solid compounds consists of one of the crystal

chemical constituents. The composition of the topmost atomic layer is an important determinant of the work function. In the case of LaB₆ the crystals can be terminated in the La or B atomic layer. The electronegativities of La and B on the Pauling scale are 1.1 and 2.04 respectively. Therefore, La terminations are cationic and B terminations are anionic. Depending on the crystal, this termination naturally occurs in one or the other [16]. Theoretical studies have established that LaB₆ crystals terminating in La have a significantly lower work function compared to those terminating in B [17]. Relaxation of the lattice near the surface is another effect to take into account when computing work function. The increase in the interatomic distance between the constituent elements affects the electron density distribution at the surface and hence the work function.

Given the sensitivity of work function to the surface state, it is unsurprising that adsorbed chemicals can affect either positively or negatively the thermionic behavior of LaB₆. Chemicals known to affect emission negatively include O₂, H₂O, CO and carbon, and so are considered “poisons” for LaB₆. Cesium is the best known work function enhancer for LaB₆, either by itself or in combination with oxygen. Values as low as 1.35 eV for cesium coadsorbed with oxygen in the (100) LaB₆ face have been reported [18].

With the recent advances of quantum mechanical modelling and increases in computational power, density functional theory (DFT) has become a powerful tool to understand electronic density distribution in condensed matter physics problems. In particular, it is now possible to compute the work function of materials from DFT simulation results [19]. Experimental measurement of the effect of surface state (including adsorbates) on the work function is extremely difficult. DFT can provide an alternative way to determine these effects. The simulation capabilities of this method enable to investigate the wide variety of scenarios that appear in the chemistry of the cathode thermionic emitter. In this work results from DFT calculations were used to formulate hypothesis that explain the observed trends in the cathode work function [20, 17, 16].

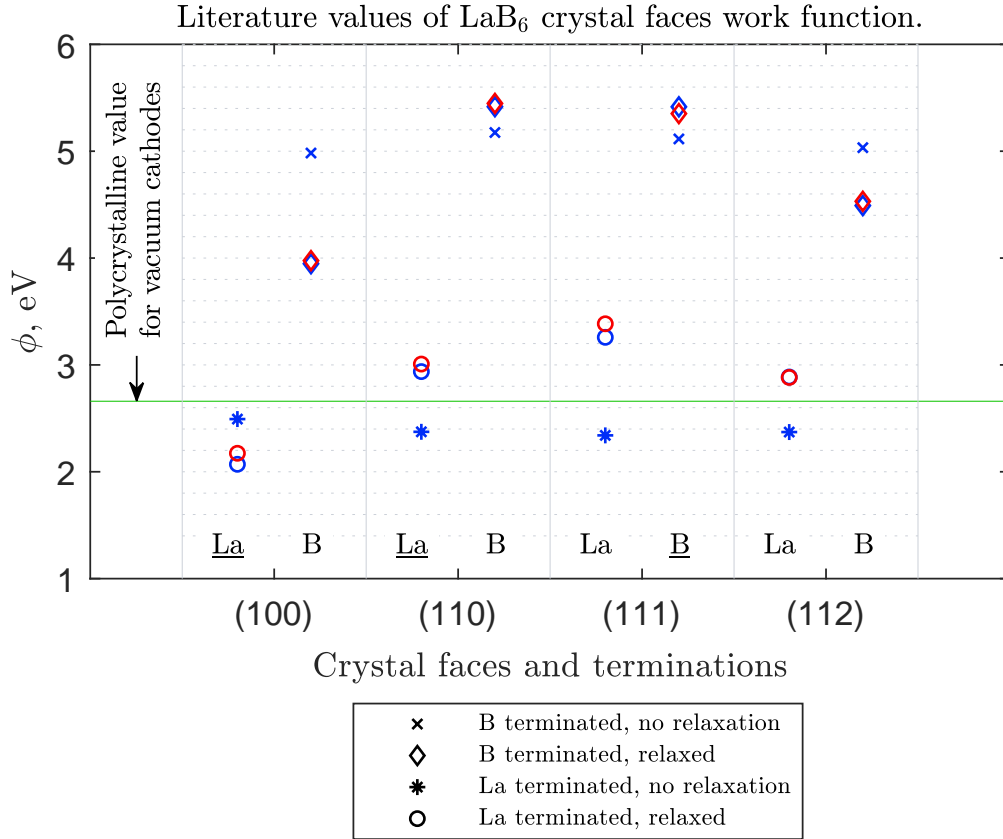


Figure 1.4: Work function of different LaB₆ crystal faces computed from DFT simulations. Data in blue is from [20]. Data in red is from [17]. Polycrystalline value is from [6]. Known natural terminations are underlined [16].

1.4 Research objectives

The main focus of this work is to characterise and understand the processes involved in establishing the working temperature of the electron emitter in a LaB₆ hollow cathode fed with xenon gas. The main research goals are:

1. Characterization of the cathode insert temperature when operated with an internal gas discharge.
2. Development of an integrated plasma and thermal model for hollow cathodes.

3. Determination of the physical phenomena responsible for the temperature distribution of the cathode.

LaB₆ has been extensively studied now for almost 70 years in different fields [16]. While these studies revealed many aspects of its structure and behavior in different contexts, none of them addresses how it is affected by plasma. Most of the studies that focus on the emission properties of LaB₆ are concerned with emission in vacuum. To our knowledge, no study has focused on the interaction between low energy (< 100 eV) noble gas ions and polycrystalline LaB₆ surfaces. This is the environment that exists inside a hollow cathode with a polycrystalline LaB₆ insert fed with noble gas.

Given the dependence of EP thrusters on cathodes for their operation, the lifetime of EP thrusters can be determined by their cathode lifetime. In the hollow cathode configuration, one of the main processes that determine lifetime is the evaporation of the emitter material, which is caused by the working temperature of the emitter. The emitting surface temperature is established by thermionic emission, which in turn depends on the work function of the material. The work function of the emitter is a material property that depends on the chemical structure of the material at the surface and therefore, it can be influenced by any process that affects the surface. In the complex hollow cathode configuration, several processes can affect the surface of the emitter. One of these processes is the redeposition of evaporated chemicals from the insert that can interact with the plasma and be recycled back to the emitting surface, changing its composition. In addition, the plasma can directly interact with the surface of the emitter and affect its thermionic properties by modifying its crystallographic structure.

1.5 Thesis outline and summary

This thesis has been organised into three chapters and a final summary and future work section. The three chapters are conference papers which are being prepared for submission to peer-reviewed journals. Chapter 2 introduces experimental work on the operating characteristics of a polycrystalline LaB₆ hollow

cathode. Results from this work served as a foundation for the development of a multidisciplinary simulation methodology for operating cathodes described in Chapter 3. In Chapter 2 we also hypothesise the possible chemical mechanisms that could explain the empirical observations. Chapter 4 presents a comprehensive study of the chemical evolution of plasma exposed LaB₆ cathode surface that sheds light on the physical basis of the cathode thermal behavior.

In order to understand the interaction between the cathode plasma and the polycrystalline LaB₆ emitter surface, we developed a state-of-the-art experimental setup consisting of a stand-alone instrumented hollow cathode placed inside a vacuum chamber capable of unattended operation. This configuration allows down to 10^{-5} Torr of high vacuum, which closely approximates the conditions that the cathode experiences when it runs in thrusters. Further, we developed a data acquisition system to capture all relevant parameters used for cathode diagnostics with one-second time resolution. Using this system, we discovered a thermal transient behavior of the cathode for which there was no previous evidence or explanation. Specifically, we observed that the temperature of the insert drops over the first few tenths of hours. This temperature drop is consistent with an approximately 0.4 eV decrease in the work function of the electron emitter (Chapter 2).

To further understand the relationship of the temperature drop and the material work function, the different experimentally measured variables that define the cathode operating condition need to be traced back to the thermionic emission characteristics of the cathode. This task is challenging, given the coupled multiphysics nature of a hollow cathode. The cathode plasma, the thermal architecture, and the chemistry evolution form a complex network of interrelations. The temperature of the insert is established by the plasma heat fluxes, the thermal characteristics of the entire cathode, and its environment. The plasma heat fluxes depend on the following: the distribution of electrons and ions inside the cathode (plasma structure), the work function of the material, the energy accommodation coefficient (inelastic collisions between ions and atomic structure of the surfaces) and the specific neutralization mechanism that occurs upon ion-surface interaction.

The plasma structure is established by the temperature of the insert, its work function, and other effects that appear when plasma is created and interacts with the emitter surface, i.e., return current of electrons and ions, and the Schottky effect (lowering of the effective work function due to the presence of the plasma electric field on the emitting surface).

We attribute the temperature drop to a work function reduction produced by the interaction between the cathode plasma and the insert. To uncover the precise work function reduction, we developed a computational platform where all three physical effects – plasma, thermal and chemical – are simultaneously studied. This self-consistent cathode modelling approach is described in Chapter 3. A thermal model of the entire cathode was created and validated experimentally for this work. We use the plasma solver OrCa2D to simulate the distribution of electrons and ions inside the cathode [21, 22, 23, 24, 25, 26, 4]. At the interface between these two models, we compute the heat fluxes that will ultimately heat the cathode structure and establish its temperature. At this step we defined the effect of the energy accommodation coefficient and neutralization model. The platform requires the input of the experimentally measured discharge current and voltage, keeper voltage, and xenon mass flow rate to specify the boundary conditions. We use an initial plasma structure to start the simulation. This plasma structure is created using a combination of work function and temperature distribution that produces a viable numerical solution while satisfying the boundary conditions. With the plasma distribution we then compute the heat fluxes that will produce a temperature distribution once input into the thermal model. The model then outputs the temperature distribution of the cathode. If the temperature distribution of the insert does not match the one previously used to create the plasma structure, a new temperature distribution is input into the plasma solver. This new temperature distribution is closer to the one output by the thermal model. This cyclic simulation process continues until the temperature distribution produced by the thermal model is the same as the one input into the plasma solver in the previous iteration.

Using the self-consistent cathode model, a converged solution of the coupled

system was found. However, upon initial attempts, the simulated temperature distribution did not agree with our temperature measurements. We then studied the effect of the energy accommodation coefficient and a two-step neutralization mechanism on the self-consistent solution. The energy accommodation coefficient (EAC) is primarily influenced by the mass ratio of the ions and the atoms at the surface. For the Xe–LaB₆ system, a value no less than 80% is expected. With that EAC value no agreement with experimentally measured temperatures was found. However, we found that incorporating a two-step neutralization mechanism yields agreement with experimental measurements. This mechanism could also govern the neutralization process in other cathode technologies where low work function emitters are employed. This approach constitutes the first successful attempt to simulate a LaB₆ hollow cathode with 2D axisymmetric models for the plasma and heat transfer to the cathode that are self-consistently coupled.

Finally, we sought to understand the underlying chemical basis of the observed work function reduction upon exposure to plasma (Chapter 4). To this end, we investigated the chemical, crystallographic and morphological changes of the cathode emitting surface after it is exposed to the cathode internal plasma. Since crystallographic analyses require flat surfaces for optimal performance, we designed and fabricated a new two-part emitter geometry with a flat portion of surface.

In order to characterise the effect of plasma on the morphology evolution of the surface, we employed scanning electron microscopy (SEM). In SEM, accelerated electrons are forced to collide against a surface. When the electrons interact with the sample, they are decelerated by inelastic collisions, producing a variety of signals. One of these signals is the secondary electron emission, which is used to produce SEM images. We further used a stylus profilometer to quantify the effect of plasma on the topology evolution of the surface. Stylus profilometers measure the surface profile of a sample by physically moving the tip of a probe along the sample surface.

Chemical characterisation and direct work function measurement were performed using spectroscopic methods including ultraviolet photoemission spectrometry (UPS) and X-ray photoemission spectrometry (XPS). UPS is a surface analysis

technique which provides both elemental and chemical state information on virtually any material. XPS is similar to UPS except that it uses X-rays rather than ultraviolet light to excite electrons. X-rays penetrate deeper into the materials and therefore electrons from core levels can be excited. UPS and XPS can be used to directly measure the material work function.

Finally, we employed two complementary diffraction methods – electron backscattering diffraction (EBSD) and X-ray diffraction (XRD) – to identify different crystallographic phases and explore the evolution of the relative exposed crystal faces after cathode interior plasma interaction.

EBSD is a surface analysis technique that allows quantitative microstructural analysis in SEM up to a nanometer scale. In this method, a beam of electrons is focused at the point of interest on a tilted sample. Upon inelastic interaction between the impinging electrons and the atomic structure of the sample surface, scattered electrons form a divergent source of electrons close to the surface of the sample that contains information about the crystalline structure of the sample.

XRD is another surface analysis method that provides information about the crystalline nature of materials at penetration depth of around 10 μm . Similarly to EBSD, XRD employs constructive interactions between X-rays and atomic structures producing patterns that can be recorded and used against database information to deconvolve the different phases present in the sample.

Results from different analytical approaches collectively revealed that the observed work function reduction is likely due to the emergence of a crystallographic texture in the LaB_6 insert induced by the interaction with Xe plasma. In addition, we hypothesize that forced cationic termination may be a secondary factor contributing to the work function reduction in operating cathodes.

1.6 Impact of results

Together, this work provides an in depth insight into the thermal behavior and effect of plasma exposure on polycrystalline LaB_6 inside a hollow cathode. Results revealing the unexpected phenomenon of work function reduction upon plasma

exposure on LaB₆ suggest that the evaporation rates of LaB₆ hollow cathodes may be much lower than previously thought and therefore their lifetime much longer. Given the importance of lifetime for EP components, LaB₆ could outperform current technologies and become the component of choice in EP thrusters for future space missions.

We show that material compatibility is still an unresolved issue for LaB₆. Graphite cups around the LaB₆ insert can still lead to contamination of the thermionic emitting surface. The effect of this contamination was manifested by an increase in the insert temperature. This observation together with the temperature transients suggest that common cathode experimental practice needs to be updated in order to obtain significant value from experiments. Furthermore, the problem of material compatibility has been shown to be very detrimental for cathode lifetime and therefore, we urge a solution to be found before unexpected premature failures start occurring.

From the cathode modelling standpoint, this work demonstrates the following: assuming the cathode plasma solution is accurate, the classical model to compute thermal fluxes from the plasma solution is not accurate. In fact, we were only capable of finding a reasonable agreement with experimentally measured insert temperatures when we used a two step neutralization model for the return current of ions to the cathode. This is a major finding as the involvement of a two step neutralization process was not previously recognized. Furthermore, this modelling approach may be applicable to other low work function cathode technologies.

Our contribution to the understanding of the correct chemical picture behind the work function evolution in LaB₆ emitters upon plasma exposure should also be noted. We have shown that the only phase present after plasma exposure at room temperature is LaB₆. We also prove that a crystallographic texture appears after plasma exposure. Together, these pieces of evidence are in agreement with the hypothesis of Uijttewaal [20] who proposes a correlation between low work function crystal faces and high surface stability. This idea establishes the thermodynamic base for the crystallographic evolution upon plasma exposure.

BIBLIOGRAPHY

- [1] John R. Brophy, Marc D. Rayman, and Betina Pavri. “Dawn: An Ion-Propelled Journey to the Beginning of the Solar System”. In: *2008 IEEE Aerospace Conference*. IEEE, Mar. 2008, pp. 1–10. DOI: 10.1109/AERO.2008.4526264 (cit. on p. 2).
- [2] E. Y. Choueiri. “A Critical History of Electric Propulsion: The First 50 Years (1906-1956)”. In: *Journal of Propulsion and Power* 20.2 (Mar. 2004), pp. 193–203. DOI: 10.2514/1.9245 (cit. on p. 3).
- [3] James S Sovey, Vincent K Rawlin, and Michael J Patterson. “Ion Propulsion Development Projects in U.S.: Space Electric Rocket Test I to Deep Space 1”. In: *Journal of Propulsion and Power* 17.3 (May 2001), pp. 517–526. DOI: 10.2514/2.5806 (cit. on p. 3).
- [4] Dan M Goebel et al. “Hollow cathode theory and experiment. I . Plasma characterization using fast miniature scanning probes”. In: *Journal of Applied Physics* 98.11 (2005), p. 113302. DOI: 10.1063/1.2135417 (cit. on pp. 5, 13).
- [5] Torsten Lundstrom. “Borides: Solid-State Chemistry”. In: *Encyclopedia of Inorganic Chemistry*. Chichester, UK: John Wiley & Sons, Ltd, Mar. 2006. DOI: 10.1002/0470862106.ia023 (cit. on p. 6).
- [6] J. M. Lafferty. “Boride Cathodes”. In: *Journal of Applied Physics* 22.3 (Mar. 1951), pp. 299–309. DOI: 10.1063/1.1699946 (cit. on pp. 6, 8, 10).
- [7] A. M. Alper. *Phase Diagrams*. Elsevier, 1976, pp. 91/159, 142/3. DOI: 10.1016/B978-0-12-053204-9.X5001-2 (cit. on p. 7).
- [8] Chun-hua Chen et al. “Structural refinement and thermal expansion of hexaborides”. In: 366 (2004), pp. 2003–2005. DOI: 10.1016/S0925-8388(03)00735-7 (cit. on p. 7).
- [9] Koichi Momma and Fujio Izumi. “VESTA 3 for three-dimensional visualization of crystal, volumetric and morphology data”. In: *Journal of Applied Crystallography* 44.6 (Dec. 2011), pp. 1272–1276. DOI: 10.1107/S0021889811038970 (cit. on p. 7).
- [10] Alexander Dean Elliot. “Structure of pyrrhotite 5 C (Fe 9 S 10)”. In: *Acta Crystallographica Section B Structural Science* 66.3 (June 2010), pp. 271–279. DOI: 10.1107/S0108768110011845 (cit. on p. 7).

- [11] M. E. Schlesinger, P. K. Liao, and K. E. Spear. “The B-La (Boron-lanthanum) system”. In: *Journal of Phase Equilibria* 20.1 (1999), pp. 73–78. DOI: 10.1361/105497199770335974 (cit. on p. 8).
- [12] Longuet-Higgins. “The electronic structure of the borides M B 6”. In: *Proceedings of the Royal Society of London. Series A. Mathematical and Physical Sciences* 224.1158 (July 1954), pp. 336–347. DOI: 10.1098/rspa.1954.0162 (cit. on p. 8).
- [13] Barbara Albert and Harald Hillebrecht. “Boron: Elementary Challenge for Experimenters and Theoreticians”. In: *Angewandte Chemie International Edition* 48.46 (Nov. 2009), pp. 8640–8668. DOI: 10.1002/anie.200903246 (cit. on p. 8).
- [14] R. A. Andrievski Y. G. Gogotsi. *Materials Science of Carbides, Nitrides and Borides*. Vol. 68. 1999. DOI: 10.1007/978-94-011-4562-6 (cit. on p. 8).
- [15] M Gesley and L.W. Swanson. “A determination of the low work function planes of LaB6”. In: *Surface Science* 146.2-3 (Nov. 1984), pp. 583–599. DOI: 10.1016/0039-6028(84)90451-5 (cit. on p. 8).
- [16] Michael Trenary. “Surface science studies of metal hexaborides”. In: *Science and Technology of Advanced Materials* 13.2 (Apr. 2012), p. 023002. DOI: 10.1088/1468-6996/13/2/023002 (cit. on pp. 9, 10, 11).
- [17] Jian Wang et al. “Work functions of metal hexaborides: Density functional study”. In: *Modern Physics Letters B* 32.2 (2018), pp. 1–8. DOI: 10.1142/S0217984918500070 (cit. on pp. 9, 10).
- [18] S.A. Chambers et al. “Cesium and oxygen coadsorption on LaB6, single crystal surfaces”. In: *Surface Science* 118.1-2 (June 1982), pp. 75–92. DOI: 10.1016/0039-6028(82)90015-2 (cit. on p. 9).
- [19] Johannes Voss et al. “Thermionic current densities from first principles”. In: *Journal of Chemical Physics* 138.20 (2013). DOI: 10.1063/1.4805002 (cit. on p. 9).
- [20] M A Uijtewaal, G. A. de Wijs, and R. A. de Groot. “Ab Initio and Work Function and Surface Energy Anisotropy of LaB 6”. In: *The Journal of Physical Chemistry B* 110.37 (Sept. 2006), pp. 18459–18465. DOI: 10.1021/jp063347i (cit. on pp. 9, 10, 16).
- [21] Ioannis G Mikellides and Ira Katz. “Wear Mechanisms in Electron Sources for Ion Propulsion , 1 : Neutralizer Hollow Cathode”. In: *Journal of Propulsion and Power* 24.4 (2008). DOI: 10.2514/1.33461 (cit. on p. 13).

-
- [22] Ioannis G Mikellides et al. “Hollow cathode theory and experiment. II . A two-dimensional theoretical model of the emitter region”. In: *JOURNAL OF APPLIED PHYSICS* (2005), pp. 1–14. DOI: 10.1063/1.2135409 (cit. on p. 13).
- [23] Ioannis G Mikellides et al. “Plasma processes inside dispenser hollow cathodes”. In: *Physics of Plasmas* 13.May (2006), p. 063504. DOI: 10.1063/1.2208292 (cit. on p. 13).
- [24] Ioannis G Mikellides et al. “Wear Mechanisms in Electron Sources for Ion Propulsion , II: Discharge Hollow Cathode”. In: *Journal of Propulsion and Power* 24.4 (2008). DOI: 10.2514/1.33462 (cit. on p. 13).
- [25] Ioannis G Mikellides et al. “The discharge plasma in ion engine neutralizers : Numerical simulations and comparisons with laboratory data”. In: *Journal of Applied Physics* (2010), pp. 1–12. DOI: 10.1063/1.3514560 (cit. on p. 13).
- [26] Ioannis G Mikellides. “Effects of viscosity in a partially ionized channel flow with thermionic emission”. In: *Physics of Plasmas* (2009), pp. 1–10. DOI: 10.1063/1.3056397 (cit. on p. 13).

Chapter 2

WORK FUNCTION REDUCTION IN LANTHANUM HEXABORIDE HOLLOW CATHODES OPERATED IN GAS DISCHARGES

2.1 Abstract

Thermal characterization of lanthanum hexaboride (LaB_6) hollow cathodes has revealed lower than expected electron emitter temperatures when the cathode reaches steady state. This phenomenon is observed at discharge currents ranging from 5 to 35 A and xenon mass flow rates of 5 to 25 sccm in cathodes with three different orifice diameters. Thus, the accepted value of the work function for polycrystalline LaB_6 , 2.66 eV, does not describe well the emission characteristics of LaB_6 hollow cathodes operating with internal gas discharges at steady state. The measured temperatures and a model of the hollow cathode emitter and xenon discharge were used to estimate the value of the work function in these experiments, yielding a value ranging from 2.1 to 2.44 eV. Measurements of the work function as a function of depth on a hollow cathode emitter using X-ray photoelectron spectroscopy and ion beam milling indicate that the work function for lanthanum-rich stoichiometry is lower than 2.66 eV. We postulate several mechanisms that could explain this enhancement. This observation has consequences on the design, study approach, and operation of these cathodes and potentially other cathodes with hollow configuration. Furthermore, it opens the question of why the work function is enhanced. Regardless of the answer to these questions, LaB_6 cathodes are now important competitors to other conventional cathode technologies.

2.2 Introduction

NASA's vision for human exploration for the near future includes the Deep Space Transport (DST). One of the ultimate objectives is piloted Mars missions

employing this architecture. However, this ambitious goal is extraordinarily difficult given the large mass necessary to reach Mars and provide habitable conditions for the astronauts. A very high efficiency propulsion system such as high-power electric propulsion can yield mass reductions that enable near-term deep space missions. NASA is investing in high power, light weight solar arrays and high power Hall thruster systems to enable this vision. Reaching further with heavier payloads is the key objective of this new endeavor. In order to successfully accomplish this challenge, a new scalable propulsion system has been under development at NASA since 2012. The goal is to develop the components for an Advanced Electric Propulsion System (AEPS) with a total system power of 40 kW. A key building block of the system is the Hall Effect Rocket with Magnetic Shielding (HERMeS). Hollow cathodes are at the heart of the system, with LaB₆ being one of the cathode technologies under development.

Increased understanding of the detailed physical processes underlying Hall thruster operation has eliminated some of the possible failure modes that can limit the thruster lifetime. One example of a significant breakthrough in Hall thruster technology is the so-called magnetic shielding, a technique that employs carefully engineered magnetic fields to protect surfaces close to the plasma discharge from erosion. Nonetheless, a number of failure modes associated with different Hall thruster components are yet to be resolved, several of which are related to the thruster cathodes. It is important that the Hall thruster service life, aimed to exceed 35k hr, is not limited by the cathode lifetime. Thus, understanding cathode failure modes is of paramount importance for future NASA activities.

LaB₆ hollow cathodes have a demonstrated capability for long life operation. They also exhibit other advantages: they are more resistant to poisoning by reactive gases than dispenser cathodes and they are scalable to high discharge densities [1]. LaB₆ emitter lifetime is ultimately limited by evaporation related to high temperature operation and thermal loads.

Thermionic electron emission is the principal mechanism by which hollow cathode discharges operate [2]. The thermodynamic work necessary to free electrons from the cathode insert inner surface is determined by the emitting surface work

function ϕ (ϕ is the work function of the material with a nominal value of 2.66 eV for LaB₆). The fraction of electrons in the emitter with sufficient energy to escape the work function barrier at the surface is related to the surface temperature by Eq. 2.1. Thus, precise knowledge of the emitting surface temperature distribution is essential to fully understand the current emission capability. In addition, insert evaporation, one of the main failure modes that affects state of the art cathodes, is exponentially related to the material temperature.

The thermionic emission current density (j_{ther}) is defined by the Richardson-Dushman equation:

$$j_{\text{ther}}(\phi, X) = DT(X)^2 \exp\left(\frac{-e(\phi - \phi_{\text{Schottky}})}{k_{\text{B}}T(X)}\right) \quad (2.1)$$

with the parameter $D = 29 \text{ A/cm}^2 \text{ K}^2$ correcting for the temperature dependence of the work function, $T(X)$ is the temperature at any point X in the insert, k_{B} is Boltzmann constant. ϕ_{Schottky} is the reduction in the work function due to the external electric field and e is the electron charge.

Precise temperature measurements are challenging due to the high temperature at which these cathodes normally operate, often close to 2000 K. Further, LaB₆ cathodes consist of many components that cluster in assemblies, which makes them difficult to instrument. Previous efforts have established two approaches for measuring temperatures inside hollow cathodes, namely thermocouples and fiber optic pyrometers.

Type C commercial thermocouples have the highest operating temperature range (0-2320 °C), which makes them an attractive option for cathode instrumentation. The downside is that they typically have a 1% precision. Fiber optic systems, on the other hand, require calibration, which can be very difficult to accomplish at that high temperature without using thermocouples.

In this paper, we present the results from using type C thermocouples to measure temperatures inside LaB₆ cathode inserts for a variety of cathode operating conditions and three different orifice diameters. Thermocouple accuracy, stability and placement strategy were assessed both experimentally and by computational

simulations using the in-house plasma solver OrCa2D and COMSOL Multiphysics[®]. Surprisingly, the data revealed that the commonly accepted work function value for polycrystalline LaB₆ (2.66 eV [2]) cannot adequately describe the emission characteristic of the cathode at steady state. Instead, lower work functions are necessary to fit the measured temperatures and discharge currents to the Richardson-Dushman equation. We propose several mechanisms that could be responsible for these atypically low work function values, including formation of stable phase LaB₄, forced cationic termination of LaB₆ crystals, formation of a crystallographic texture, and surface absorption of some contaminant that actually enhances the LaB₆ work function.

2.3 Description of the measurement approach

The cathode used in these experiments has been described in [1]. Briefly, it consists of a cathode tube with a cylindrical LaB₆ emitter (the “insert”) positioned at the downstream end in front of an orifice plate, which serves to increase the internal gas pressure (Fig. 2.1). The downstream portion of the cathode tube is surrounded by a heater used to preheat the insert material for ignition. The heater is covered by tantalum foil shielding to minimize heat loss through radiation at start or during normal operation. Finally, the assembly is enclosed in one more concentric electrode, termed the keeper, which is used as an ignitor electrode or to maintain a secondary discharge to keep the cathode operating in the event of extinction of the main discharge.

In this work, three orifice plates with different orifice diameters were used – small, medium and large. Medium refers to the nominal orifice plate envisioned for HERMeS, and the small and large orifice diameters were 80% and 160% of nominal, respectively. The insert was perforated using electro-discharge machining (EDM) in order to place three ~1.6 mm diameter Idaho Laboratories Type C sheathed thermocouples longitudinally. The thermocouples were distributed evenly in the azimuthal direction and were installed at three different depths in the insert (Fig. 2.2). Herein, we use TC1, TC2, and TC3 to refer to the temperatures measured by the thermocouples positioned at the highest, middle, and lowest

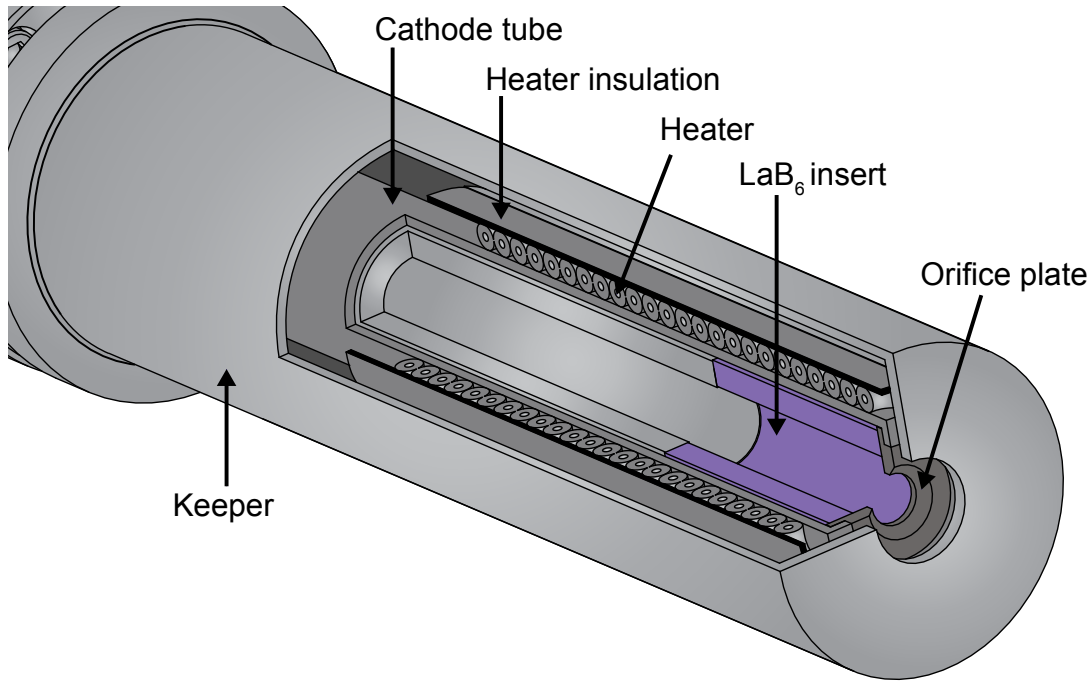


Figure 2.1: LaB₆ hollow cathode schematic.

depth, respectively (see Fig. 2.2). A second order polynomial was used to fit the three measurements to give an approximation of the temperature profile. In order to assure good thermal contact between the thermocouples and the location where temperature is measured, the thermocouples were installed using a pre-loaded spring strategy. By using this approach, each individual thermocouple can accommodate the thermal expansion of the different components of the cathode assembly and still guarantee that the bottom of the thermocouples are against the insert wells at any point in time during the experiments.

In the appendix, we discuss the thermocouple placement, accuracy and stability. We conclude from these analyses that the error introduced by the temperature measurement approach is the thermocouple accuracy plus a small temperature reduction associated with the distance between thermocouple junctions and the insert surface. Nonetheless, we plan to use fiber optic pyrometric techniques using a calibration source independent of thermocouples to measure the temperature profiles of the insert. This approach will remove all doubts about the temperature

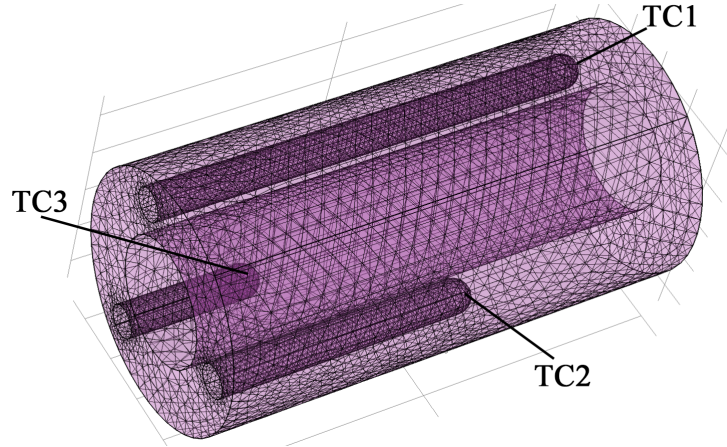


Figure 2.2: Insert finite element model with three thermocouples wells.

measurement accuracy.

A copper cylindrical anode 50.8 mm in diameter and 25.4 cm long was placed ~ 20 mm from the keeper face, concentric with the assembly. Experiments were performed inside a 4 m³ stainless steel vacuum chamber equipped with two 25.4 cm diameter cryopumps which produce a base pressure of 9×10^{-8} Torr. Data were acquired using a custom built system based on a Opto22 SNAP-PAC-EB brain that measures voltages, currents, and xenon mass flow rates with precision of 10 mV, 10 mA and 0.01 sccm with respect to calibrated values, respectively, and a 2 s refresh rate. Thermocouple signals were also acquired with the aforementioned equipment, which performs the cold junction temperature correction.

2.4 Experimental Results

We initially sought to acquire the temperature distribution using the three thermocouple approach described above. When the cathode was set to a specific operating condition, a temperature transient was observed before the temperatures stabilized. Interestingly, we found that the duration of the transient is longer than expected and depends on the previous history of the cathode: if the cathode is in steady state and a small change to either the discharge current, J_D , or the xenon mass flow rate, \dot{m}_{Xe} , is applied, the cathode temperature adapts rapidly with only

a few tens of degrees of overshoot or undershoot with respect to the steady state temperature. In such cases, the duration of the transient is around 30 min to a few hours. A detailed description of the transient behavior is provided in the following section.

Due to the variation in the time required to reach steady state and the large number of operating points to be tested, we developed a data acquisition and control (DAQ) strategy which autonomously determines when the cathode reaches steady state. The system defines steady state as the point where the temperature difference in two consecutive 15 min intervals is less than 1 °C for all three thermocouples.

2.4.1 Transient behavior

2.4.1.1 Initial start with a new LaB₆ insert

Using the automatic DAQ setup described above, we first assessed the system behavior upon initial start with a new LaB₆ insert. The ignition was performed at $J_D = 25$ A and $\dot{m}_{Xe} = 14.75$ sccm. Data showed that for a new insert, it takes tens of hours to reach steady state (Fig. 2.3). After that long transient, we observed a small amplitude, low frequency periodic fluctuation in the measured temperatures (although this phenomenon is not fully resolved in Fig. 2.3).

In addition, the data showed a peak temperature of 1737 °C and that the condition $\frac{\Delta T_{\text{mean}}}{\Delta t} = 0$ occurred around 65 hr after ignition, where T_{mean} is the mean temperature of all three thermocouples.

2.4.1.2 Initial start after atmospheric exposure

To further elucidate the unexpected cathode behavior, we studied the cathode thermal transients upon ignition after exposure to the atmosphere for several hours. To this end, we stopped the cathode discharge ($J_D = 0$ A) and let the cathode cool down completely (until thermocouples read ambient temperature) and then opened the vacuum chamber. After several hours, we evacuated the chamber and

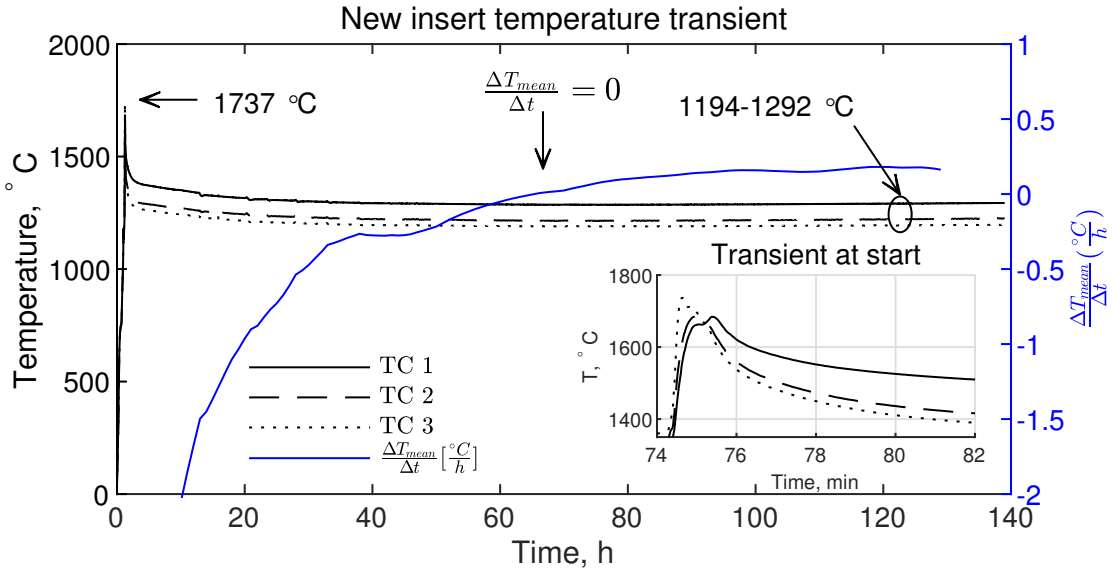


Figure 2.3: Thermal transient for a new insert at $J_D = 25$ A and $\dot{m}_{Xe} = 14.75$ sccm with the nominal orifice. In the inset it is shown the details of the temperature transient during the first few minutes of operation after the discharge power supply has been enabled.

reignited the cathode with $J_D = 25$ A and $\dot{m}_{Xe} = 14.75$ sccm. This reignition operation was performed manually, therefore, the temperature right before ignition is not the same for the three cases shown in Fig. 2.4. Only TC1 is shown for each start, which typically is the hottest of all three at ignition.

As shown in Fig. 2.4, all three starts after atmospheric exposure had initial temperatures between 1459 and 1506 °C. There does not seem to be a clear relationship between temperature right before ignition and temperature right after ignition, although the coldest start reached the highest peak temperature. A more carefully designed experiment is necessary to gain a further understanding of the thermal transient at ignition. Note here that the temperature evolution right at the start produces an overshoot. Together, these results suggest that desorption of oxides is increased if the temperature before ignition is higher.

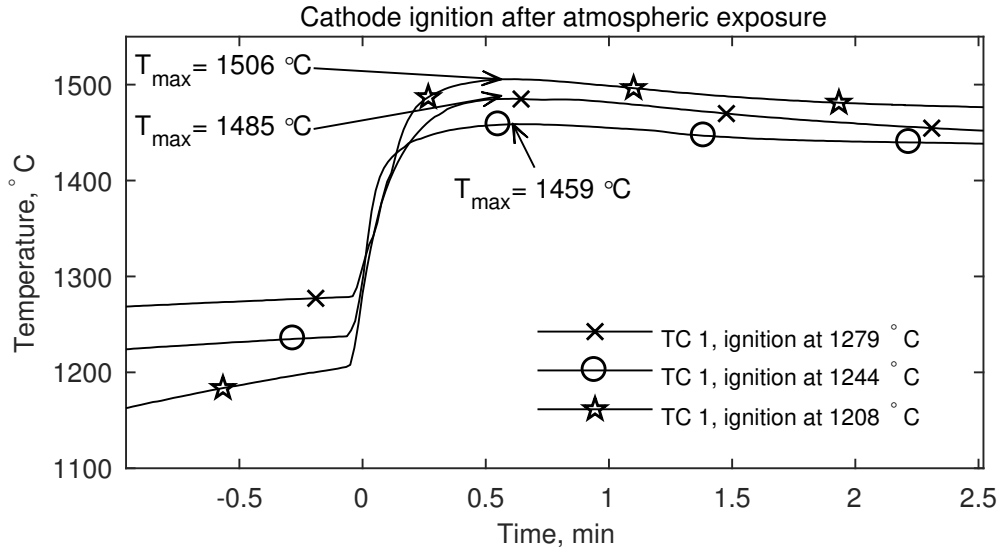


Figure 2.4: Thermal transient at $J_D = 25$ A and $\dot{m}_{Xe} = 13$ sccm with the nominal orifice after exposing the cathode to the atmosphere for several hours.

2.4.1.3 Transients associated with hot reignitions

We define hot reignition as the process of igniting the cathode after a sudden shutdown ($J_D = 0$ A), and allowing only a few hundred degrees cool-down before reigniting it. At that point, switching on only the keeper or the keeper and the heater might be necessary to reignite the cathode. Fig. 2.5 shows the temperature evolution during two different hot reignition experiments, synchronized at Time = 0 min.

Before shutting down the cathode, neither of the experiments had reached steady state, i.e., there is a temperature difference of 26 °C (Fig. 2.5). Both experiments were performed with the nominal orifice plate and $J_D = 25$ A and $\dot{m}_{Xe} = 13$ sccm.

When a reignition attempt was made by shutting down the cathode and allowing it to cool down to 1229 °C, the discharge reignited without a temperature overshoot. Later on, when the cathode was shut down and the temperature dropped to 1195 °C, the cathode reignited and reached a peak temperature of 1410 °C. A third hot reignition test was performed, reaching a minimum temperature of

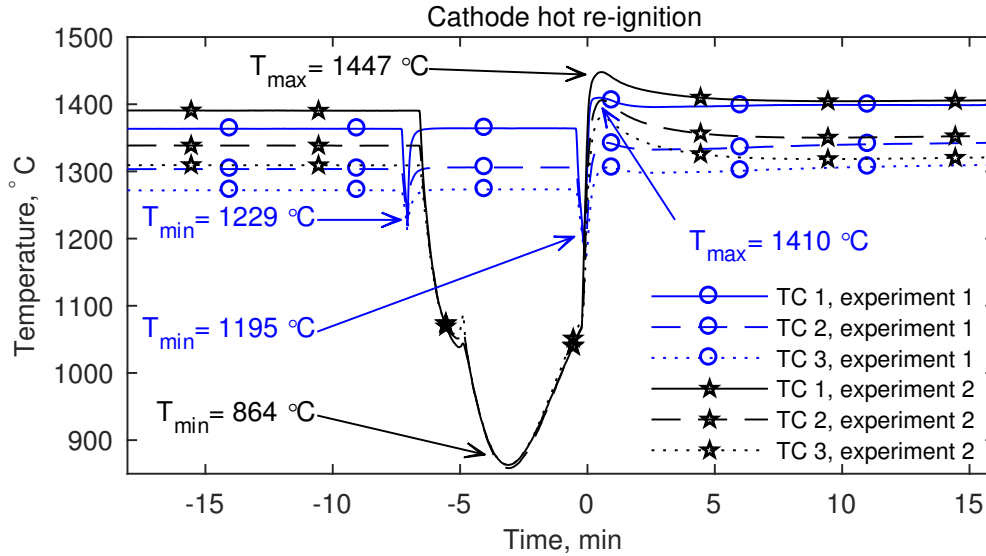


Figure 2.5: Thermal transient associated with hot re-ignition at $J_D = 25$ A and $\dot{m}_{Xe} = 13$ sccm with the nominal orifice. TC1 temperature shown for both experiments.

864 °C right before reignition, and the cathode peak TC1 temperature measured 1447 °C.

2.4.1.4 Transients associated with discharge current step events

Finally, we tested the cathode behavior with discharge current step events. To this end, we first ignited the cathode and allowed it to reach steady state, as determined by the DAQ system. At that point small changes in J_D of 2.5 A were suddenly imposed. These changes in the discharge current were applied with both ascending and descending currents. The DAQ transitioned from one operating point to the next only when a steady state condition had been reached. The thermal transient associated with a few of the step events is shown in Fig. 2.6. We observed that the direction of the discharge change (whether positive or negative) did not determine the direction of the temperature deviation with respect to the value that the temperature would ultimately reach at steady state. In some instances there was an overshoot (between 5 A to 7.5 A, 7.5 A to 10 A and 10 A to 12.5 A) whereas

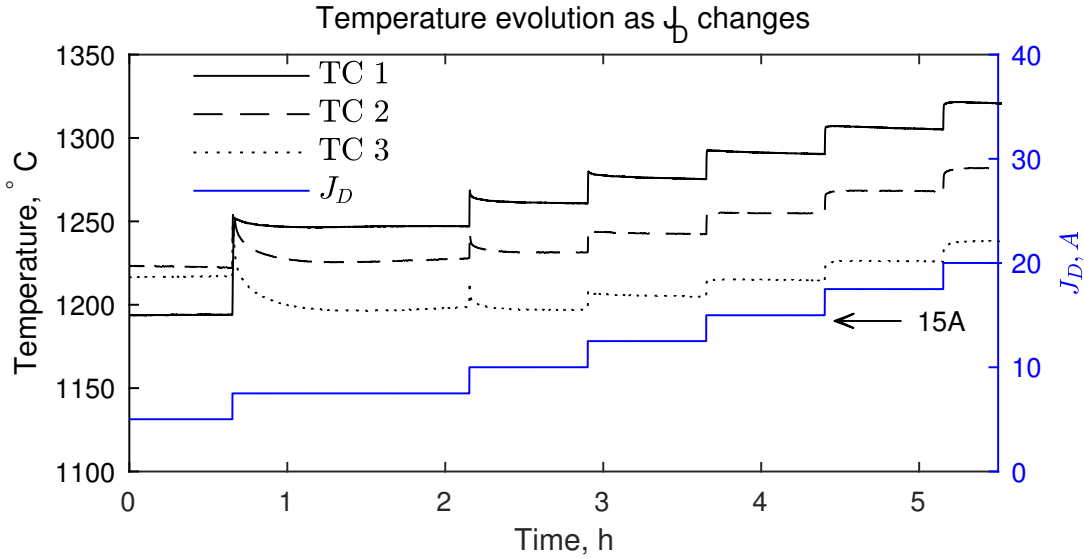


Figure 2.6: Thermal transient evolution with J_D at $\dot{m}_{Xe} = 10$ sccm with nominal orifice.

at others there was an undershoot (between 15 A to 17.5 A and 17.5 A to 20 A). There is one case in which the temperature transitions with no over- or undershoot (12.5 A to 15 A), right in the middle of overshoot and undershoot trends.

2.4.1.5 Sudden change of steady state for one operating condition

In addition to the results above, experiments revealed an unexpected phenomenon. We observed that while running the cathode at fixed operating conditions, steady state temperatures changed from one start to the next (Fig. 2.7). Following these experiments, we found a ring of black deposits in the downstream region of the insert inner surface (Fig. 2.8). When the deposit was removed, the steady state temperature dropped by almost 100 °C. We hypothesized that the source of this black coating is a graphite cup located at the cathode downstream end. Thus, we replaced the graphite cup with a 25.4 μm thick tantalum cup and ran the cathode for tens of hours and several starts. Borescope inspection of the insert inner surface following these runs did not reveal any deposits, confirming that the source of the coating was indeed graphite. As a 100 °C increase in the insert temperature

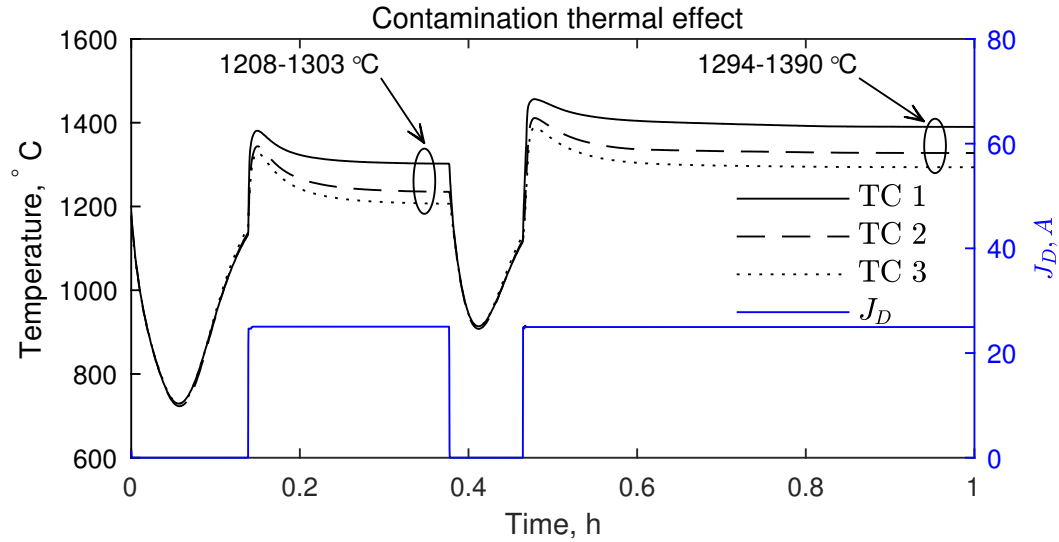


Figure 2.7: Abnormal thermal transient after a hot reignition with the nominal orifice at $J_D = 25$ A and $\dot{m}_{Xe} = 14.75$ sccm.

significantly impacts evaporation, and consequently the lifetime of the cathode, we suggest that graphite deposition has an important negative impact in the service life of the cathode. Our results strongly suggest that downstream graphite cups should be eliminated or at least redesigned in future cathode designs.

2.4.2 Steady state temperatures

The steady state temperature distribution of the cathode insert was obtained for each orifice diameter at discharge currents of 5, 10, 15, 20, 25, 30, and 35 A, and for each discharge current, \dot{m}_{Xe} was set at 5, 10, 15, 20 and 25 sccm. For the large orifice, the 5 A case was not studied as the cathode was in plume mode for that condition over the whole \dot{m}_{Xe} range under consideration. Temperature maps constructed from those data are shown in Fig. 2.9.



Figure 2.8: Detail of the contaminant deposited on the inside of the insert.

2.5 Discussion

2.5.1 Effect of orifice size on temperature

In order to assess which orifice configuration offers the best performance, we estimated the temperature profiles along the insert by fitting the data with a second degree polynomial (Fig. 2.10). For each orifice plate and cathode operating point, a different temperature profile is obtained. As minimizing LaB_6 evaporation is critical for cathode lifetime, the main parameter of interest is lower mean temperature. However, given the sensitivity of evaporation rate to temperature, deviations from the mean are also of a great importance. In addition, in order to consume the insert uniformly over time one would need to maintain a homogeneous temperature distribution along the insert. As shown in Fig. 2.10, the large orifice configuration has the highest peak temperatures for every operating condition. This is not a desirable mode of operation, as it will evaporate the insert material faster for a

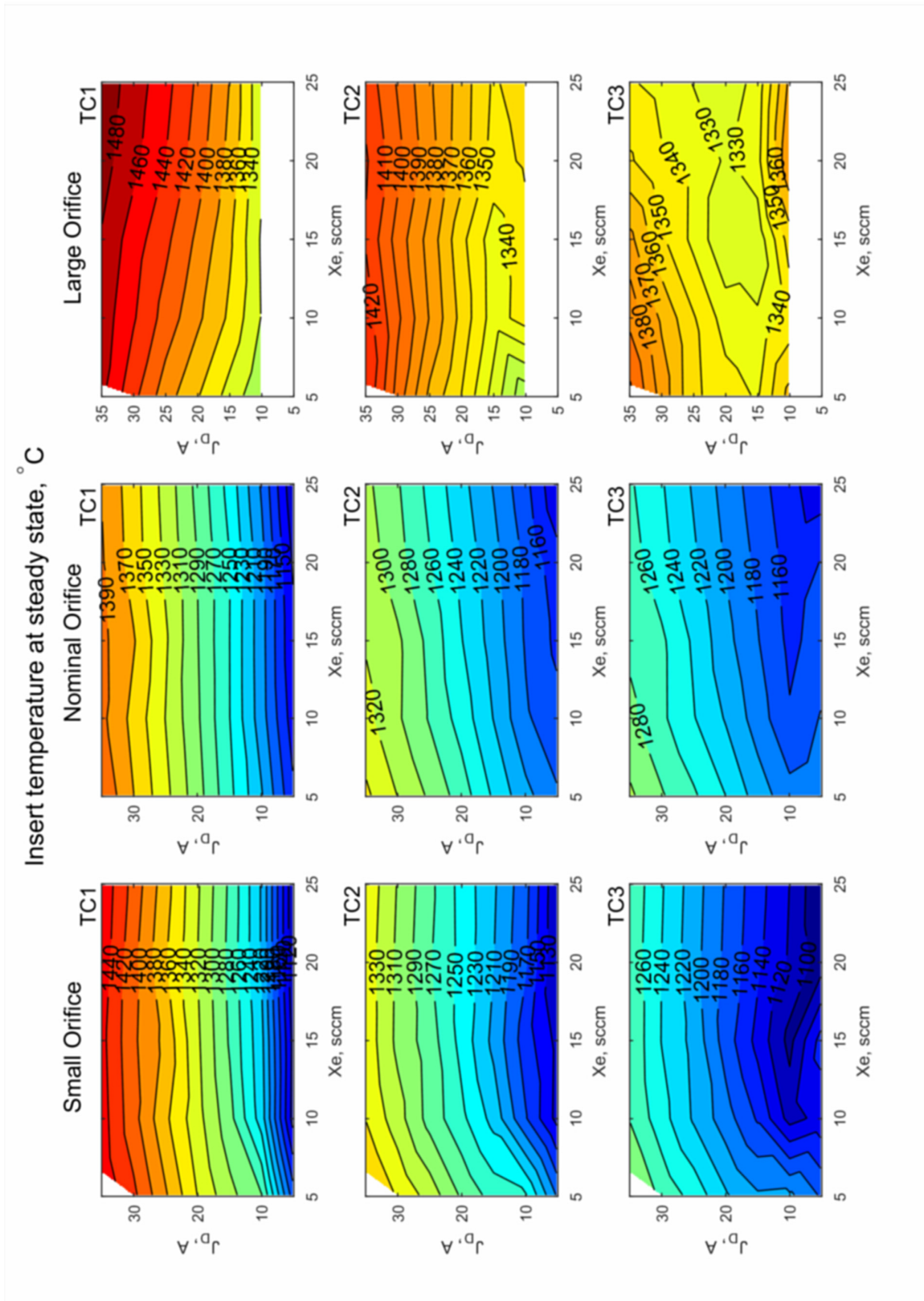


Figure 2-9: Steady state temperature distribution for each cathode configuration and each thermocouple.

given discharge current. The profiles for discharge current above $J_D = 15$ A have the smallest difference between maximum and minimum temperatures for any given profile. Minimizing the temperature gradient along the axis of the insert is desirable because the insert should then erode more uniformly over thousands of hours. Nonetheless, this is a consideration of lesser importance compared to minimizing the peak temperature for the same discharge current.

On the other hand, the small orifice shows the biggest temperature range over the same operating condition space. Peak temperatures are lower than for the large orifice case, but higher than for the nominal orifice size for discharge currents above 5 A. Differences between maximum and minimum temperatures along the insert are the largest of the three configurations for all discharge currents above 5 A.

The nominal orifice diameter offers the lowest temperature peaks for discharge currents above 5 A and differences between maximum and minimum temperatures that lie between those of the larger and smaller orifices. This configuration is the most appealing one in terms of thermal distribution. In this analysis, the evolution of the insert inner diameter and consequent effect on the temperature profile has not been taken into consideration when choosing the best configuration for the lifetime of the insert. That analysis would require knowledge of how the temperature profile evolves as the LaB₆ insert erodes.

2.5.2 Cathode temperature sensitivity to effective emissive area

The reduced temperature of the cathode at steady state could be related to an increase in the effective emissive area of the insert. Such increase in the effective area could be produced by an increase in the roughness of the insert created by the plasma. To assess the extent to which surface area increase can affect the thermal behaviour of the cathode, we analyzed the relationship between surface area and temperature for a cathode emitting at 25 A of total discharge for two values of the work function, 2.1 and 2.67 eV (Fig. 2.11). Profilometry analysis of the insert surface suggested that roughness caused by plasma exposure is unlikely to cause more than a 2-fold increase of the effective emissive area (see Chapter 4). The

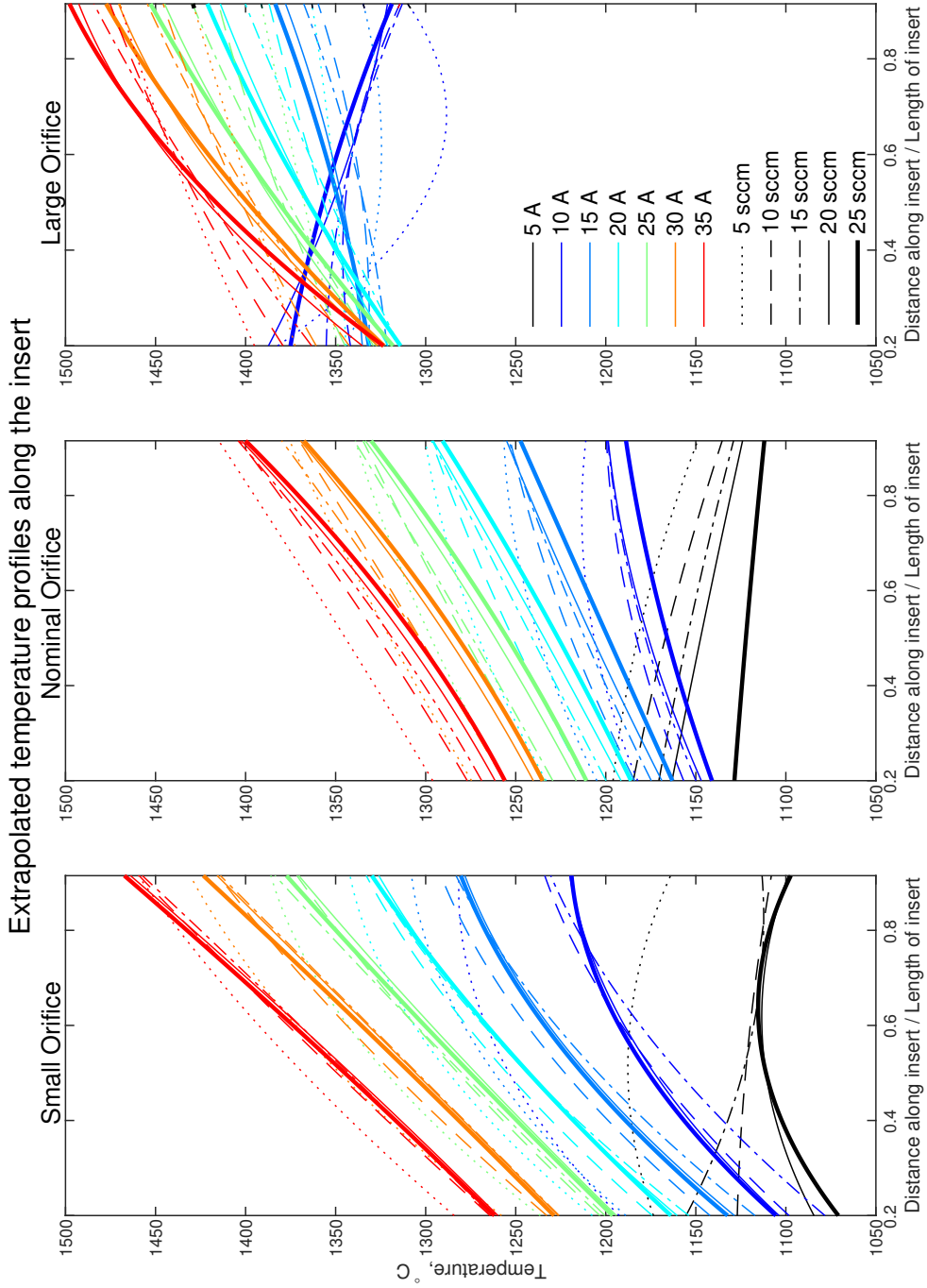


Figure 2.10: Temperature profiles approximated by a second degree polynomial fit to the thermocouple data for each operating condition. $\dot{m}_{Xe} = 5, 10, 15, 20, 25$ sccm shown with increasing color darkness for each discharge current.

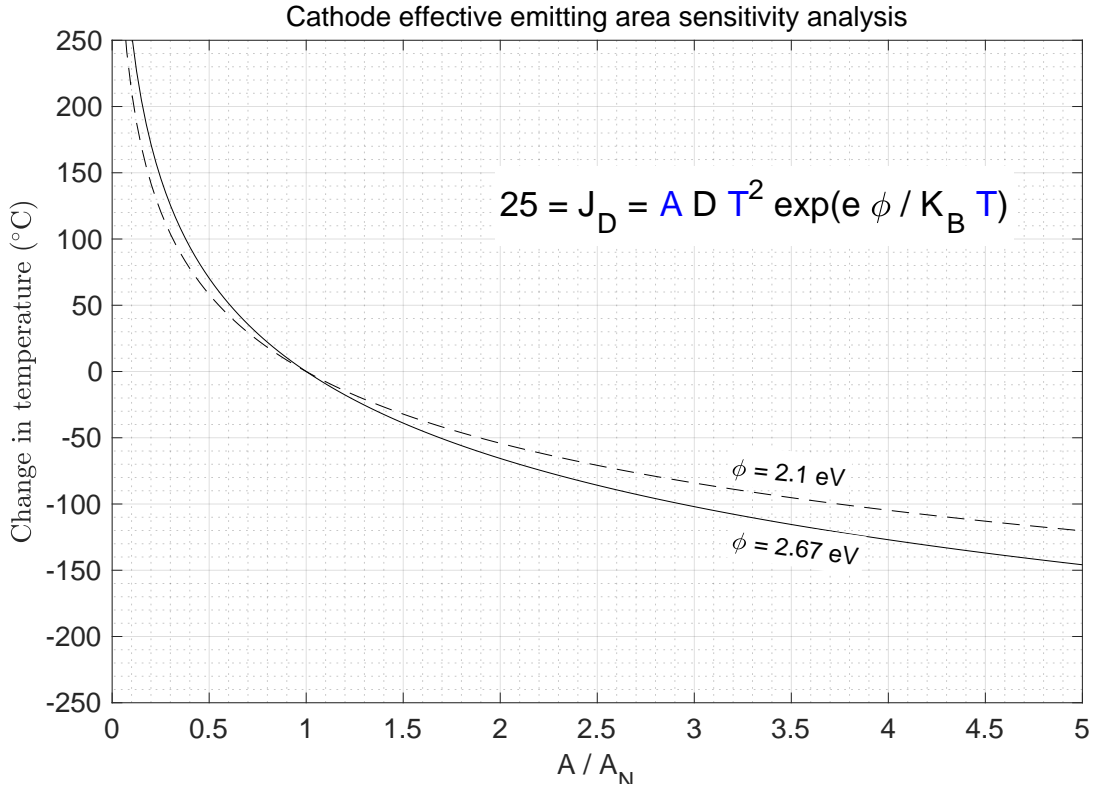


Figure 2.11: Cathode effective emitting area sensitivity analysis. A is the effective area used in the Richardson equation, A_N is the nominal emitting area based on the diameter of the emitter.

expected reduction of temperature in this case is no more than 70 °C. In the case of the nominal orifice plate in Fig. 2.10, the observed reduction is on the order of 300 °C. A 300 °C temperature reduction corresponds to more than 20-fold increase in the effective emissive insert area. Even though we cannot rule out increased effective emissive area of the insert as a contributing factor, it cannot explain the magnitude of temperature reduction of the cathode at steady state observed.

2.5.3 Inferred work function

At every point on the insert emitting surface (S), the balance between the flux of emitted electrons and the flux of ions and electrons from the plasma back to the surface determines the net current density. Integrating these three components

over the cathode area yields the total discharge current,

$$J_D = \iint_S (j_{\text{ther}}(\phi, X) - j_e(X) + j_i(X)) dS, \quad (2.2)$$

where S is the insert emitting surface, X is a point on the surface S , and $j_e(X)$ and $j_i(X)$ are the current densities of electrons and ions that return to the emitting surface and effectively increase and reduce the demand for emitted electrons (j_{ther}) for the same J_D , respectively. j_{ther} is the thermionic emission current density as modeled by Eq. 2.1.

If we try to match Eq. 2.2 assuming $\phi_{\text{Schottky}} = 0$ eV, zero ion or electron return current, $\phi = \phi_{\text{LaB}_6} = 2.66$ eV and an axisymmetric temperature distribution from Fig. 2.10, we realize that there is not enough emission to generate the measured discharge current J_D . Two terms which help increase the net current to the cathode for the same temperature distribution have been neglected in this calculation. One of them is ϕ_{Schottky} which typically has a value on the order of 0.1 eV, see Chapter 3 for more details. Even considering that, the ion return current would have to be more than 50% of the discharge current to balance Eq. 2.2, which is not realistic.

Therefore, we concluded that one possible explanation for this apparent lack of current capability could be explained if we assume that the work function in the material is lower than the value of 2.66 eV. In the following subsections we will present two different estimates for the work function for every orifice size and operating condition.

2.5.3.1 Work function estimation, method 1: Matching net J_D

Computing the work function necessary to match J_D assuming ϕ_{Schottky} , $j_e(X)$ and $j_i(X)$ are zero results in the distributions shown in Fig. 2.12. The work function seems to decrease with increasing discharge current until a minimum value is reached, at which point the trend is reversed and the work function increases. The effect of the \dot{m}_{Xe} seems of lesser importance for higher than 15 sccm flows. In the late 1970s, Storms and Mueller [3] reviewed all previous measurements of the work function for near-stoichiometry polycrystalline LaB₆ and found that there was no

consensus on a single value. Instead, they defined a range of 2.52 to 2.87 eV which encompassed the measured values. The work function found with method 1 is far from this range for most of the operating conditions studied.

2.5.3.2 Work function estimation, method 2: Minimization of $\text{sum}(\text{abs}(J_D(\phi) - J_{D, \text{measured}}))$ per orifice.

If we assume that ϕ_{Schottky} , $j_e(X)$ and $j_i(X)$ are zero and that there is a single value of the work function for a given orifice size, and select a value that minimizes the error of the absolute difference between the measured discharge current and the calculated discharge current over the entire current-flow rate parameter space, we obtained values 2.24 eV, 2.2 eV, and 2.36 eV for the small, nominal and large cathode orifice configurations.

Plots in Fig. 2.13 show the quantity $J_D(\phi) - J_{D, \text{measured}}$ for every operating condition. The shape of the distribution of this plot is similar to the one that can be obtained when computing the work function for each orifice size by minimization of the standard deviation of the error, or $\text{std}(J_D(\phi) - (J_{D, \text{measured}}))$, which is the proper method to calculate deviation from mean. Results show that given the assumptions, a single uniform work function for each cathode configuration does not adequately describe the cathode performance for all the operating conditions. However, they show that the difference is zero, or close to zero for a significant portion of the map. With a more realistic analysis that included ϕ_{Schottky} , $j_e(X)$ and $j_i(X)$, it might be possible to identify a single work function value that could produce zero error for those portions of the map.

2.5.4 Measured work functions

Given the striking difference in LaB₆ work function value between our estimates and the literature, we next sought to directly measure the work function and chemical composition of the emitting surface of an insert that had been used in the hollow cathode experiments and compare it to the estimates from the temperature data. To this end, we used the Kratos Axis Ultra XPS instrument at

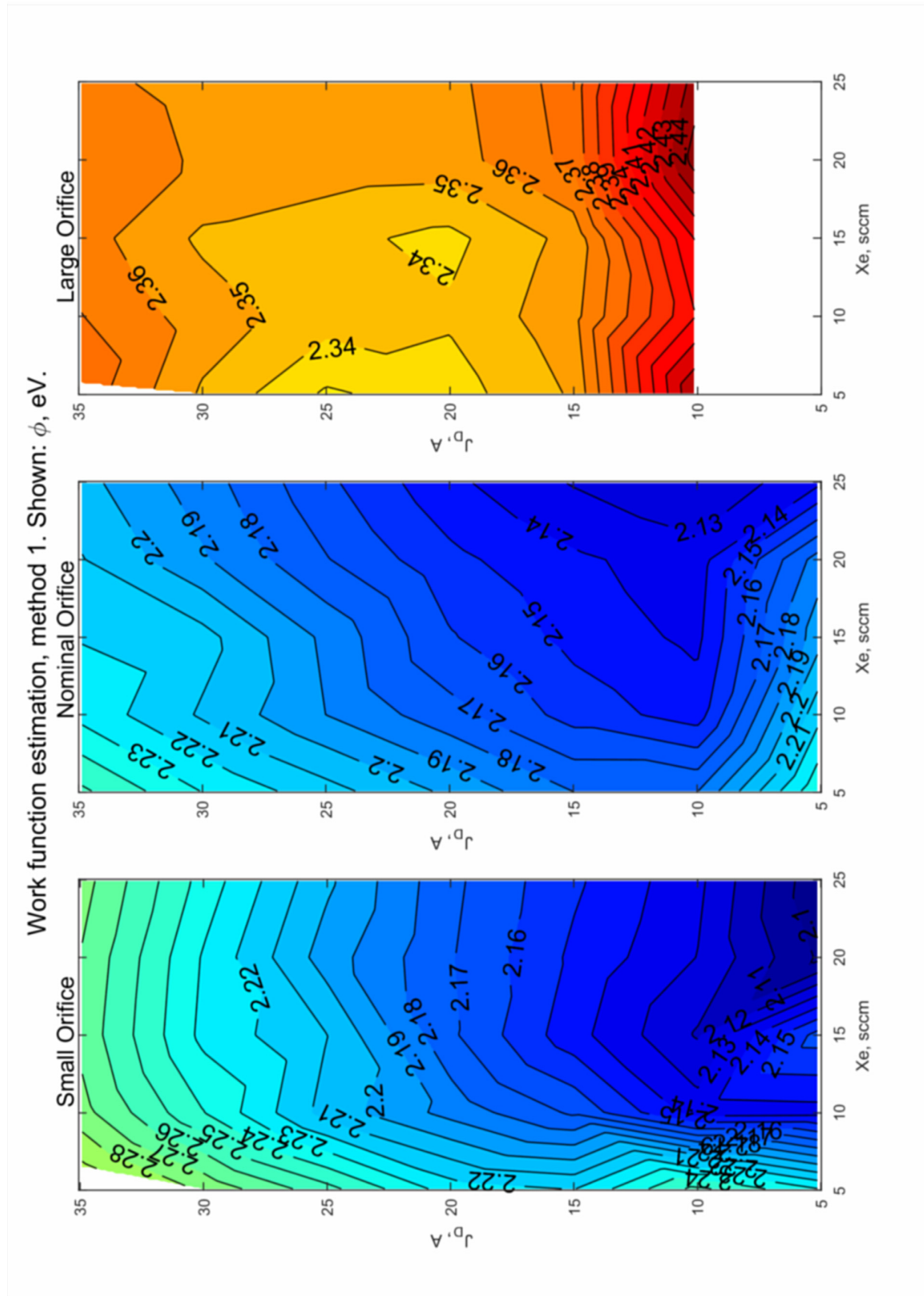


Figure 2.12: Computed work function with inferred insert temperature distribution, zero return current and $\phi_{\text{Schottky}} = 0$.

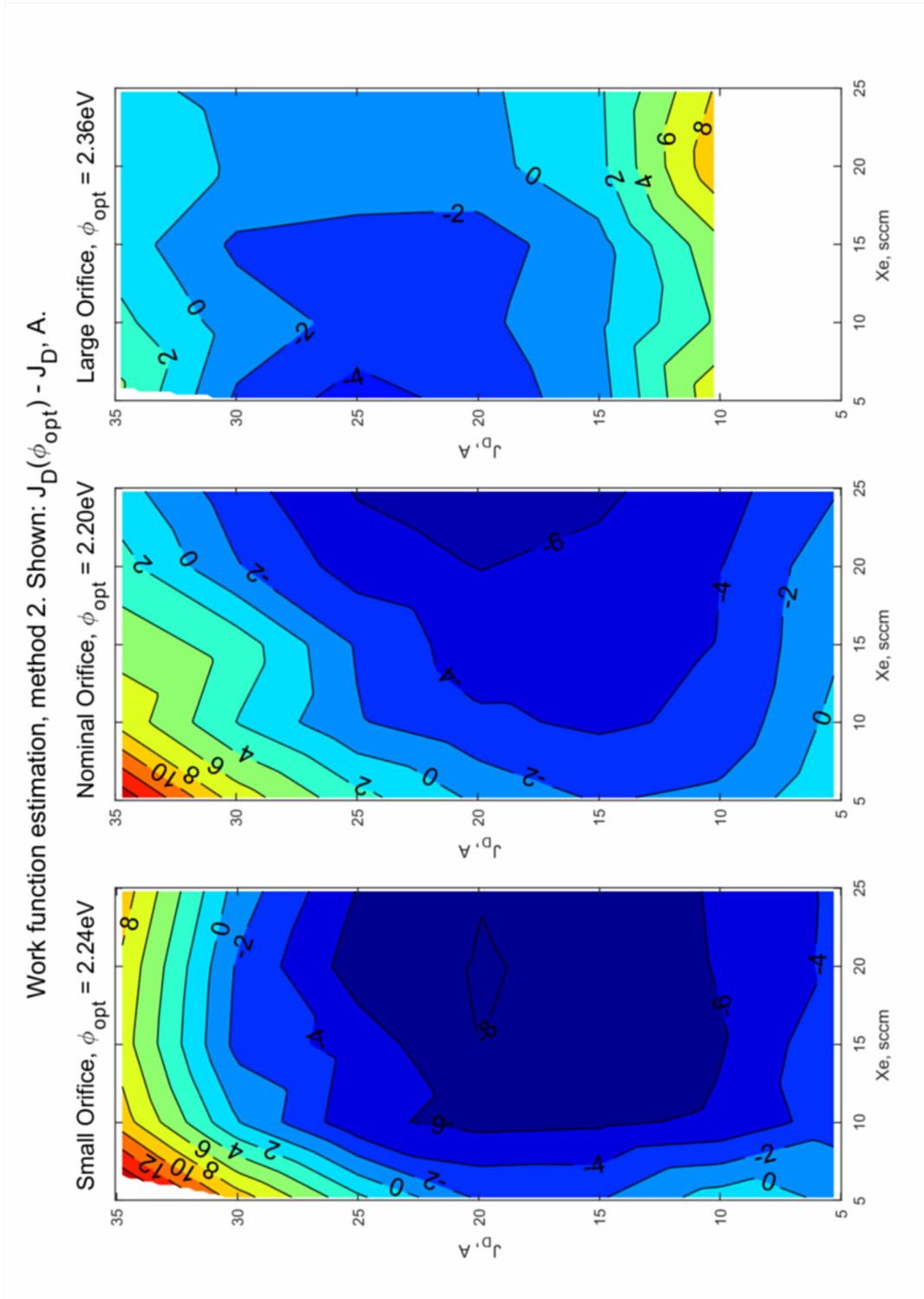


Figure 2.13: $J_D(\phi_{\text{opt}}) - J_D$, measured, zero return current and $\phi_{\text{Schottky}} = 0$ eV.

the Molecular Materials Research Center at the California Institute of Technology. This technique employs X-ray and ultraviolet photo-electron spectroscopy (XPS and UPS) to determine the secondary electron photoemission cutoff. For more information about the approach and calibration, see [4, 5]. We selected 3 spots along the emitting surface of the insert, identified as P1, P2 and P3 in Fig. 2.15, and measured the work function and photoemission spectra for each of them as a function of depth. The analysis area was approximately $900 \mu\text{m}^2$. The grains in the polycrystalline sample are only a few μm in average, so the results are averaged over many grains of the polycrystalline sample. We used an argon ion gun with 500 V, 200 μA beam energy to remove material from the upper layer and study the sample at different depths. We calibrated the etch rate at 500 V using a Dektak XT profilometer. The results indicate that LaB_6 is sputtered with the 500 V Ar beam at a rate of $5.6 \text{ nm mm}^2/\text{min}$. This rate is independent of exposure time and target area. Higher energy beams were studied but we observed evidence of ion implantation, rendering the data unusable for work function measurements.

The work function results (Fig. 2.14) show that the sample has a higher work function right at the surface and it drops with depth. The carbon levels were measured to test for the effect of surface contaminants on the work function. Results showed that the value of the work function as measured by XPS (and UPS) strongly depends on surface contamination (Fig. 2.16). With a decrease in surface carbon content, the measured value of the work function drops drastically, as can be seen for spots P2 and P3. The carbon content for spot P1 is the highest of the three and the measured work function is significantly higher. For the three locations and all depths, the stoichiometry was found to be La-rich.

The work function in spots P2 and P3 peaks in Fig. 2.14 at around 2 nm deep. The sample had to be exposed to the atmosphere for XPS maintenance before these points were taken. Figure 2.16 shows that the carbon abundance around 2 nm increased for spot P2 after the exposure, which could be the cause for the sudden increase in work function. This hypothesis is not conclusive given that spot P3 did not show an increase in the carbon composition. Oxygen and carbon surface contaminants have been reported to increase the work function by Oshima

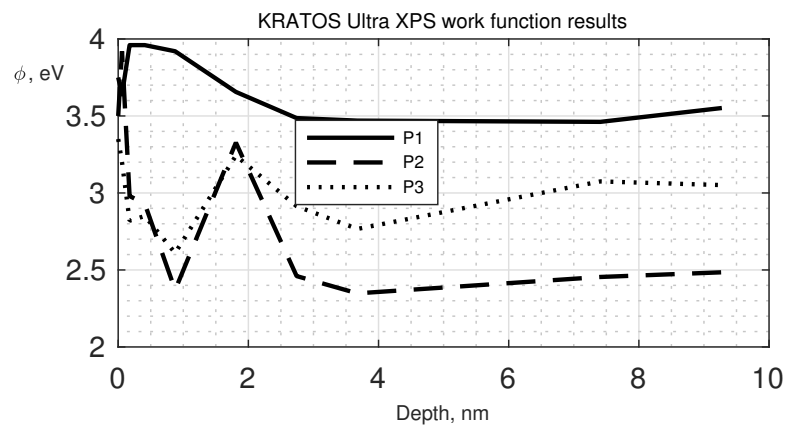


Figure 2.14: Work function as a function of depth measured at three different positions along the insert inner surface.

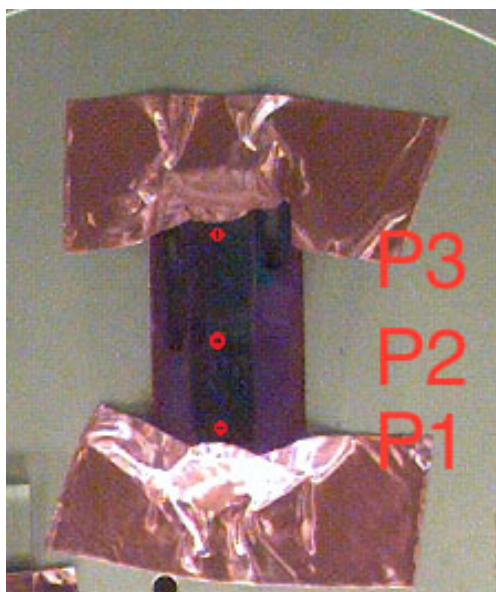


Figure 2.15: Insert piece inside the KRATOS Ultra XPS at Caltech.

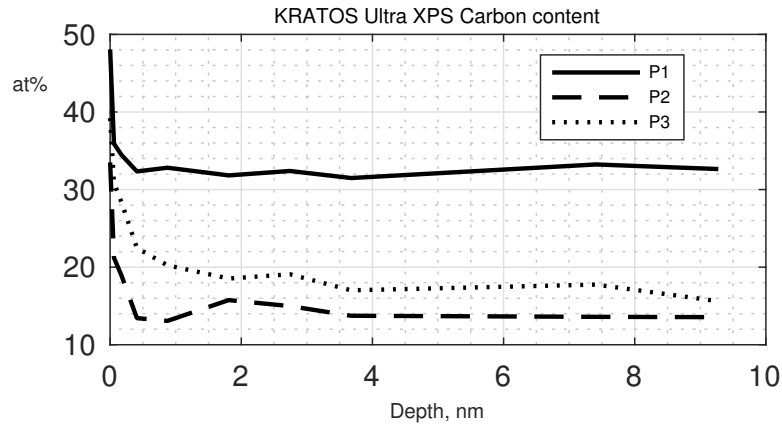


Figure 2.16: Carbon (C 1s) relative atomic abundance on the insert at three different positions along the insert inner surface. C 1s, La 3d and B 1s core levels were used for the normalization.

et al. [6], which is in agreement with our findings.

The presence of carbon and work function increase would explain the nearly 100 °C increase of the cathode temperature at steady state with the black ring deposit discussed above (Fig. 2.8). In this case the carbon coating was so dense that effectively the area of the ring would be emitting with the work function of graphite, ~ 4.6 eV [7].

Figure 2.16 indicates the presence of carbon deep inside the insert surface. This result was not expected, as the chemical analysis certification from the manufacturer claimed that the insert was prepared from carbon-free LaB₆ powder. It is not clear whether the carbon contaminating the emitting surface comes from another component of the cathode assembly or from the press sintering process associated with the insert manufacturing.

A controlled experiment measuring cathode thermal transients at ignition after abrupt shutdown from steady state and repetitive ignitions with and without atmospheric exposure could reveal whether the cathode gets contaminated with a thin film of adventitious carbon from air exposure, and whether this contamination results in higher temperature peaks during the ignition thermal transient. This would suggest a higher work function induced by the carbon film on the surface.

2.5.5 Work function reduction mechanism

We propose that the observed atypically low work function values may be explained by several mechanisms. First, we hypothesize that lanthanum redeposition on the emitter surface due to ionization and transport processes in the hollow cathode interior plasma may result in the formation of a La-rich surface due to La forced termination of LaB_6 crystals or LaB_4 deposits, resulting in lower work function. A similar recycling effect for barium has been found in dispenser hollow cathodes as well, and makes their operation in gas discharges quite different from cathodes in vacuum devices [8, 9]. Alternatively, it is well established that an enrichment of low work function crystals has a net beneficial effect on the work function of the polycrystalline solid [10]. Therefore, the observed enhanced thermionic emission may result from the formation of a specific crystallographic texture over time. Finally, a chemical outgassed by some of the cathode components could interact beneficially with the polycrystalline surface and reduce the work function.

2.5.5.1 Lanthanum recycling hypothesis

We hypothesize that the apparent reduction in work function observed on LaB_6 cathodes operated in gas discharge environments compared to cathodes operated in vacuum is due to production of a lanthanum-rich surface by recycling of lanthanum in the internal plasma. In xenon hollow cathodes, lanthanum evaporated from the cathode surface is ionized in the dense xenon plasma and returned to the surface by the electric field. The lanthanum ionization mean free path is of the order of the characteristic length scale of the collisional plasma region, so a large fraction of the evaporated lanthanum atoms are likely ionized before they can escape. Ionized lanthanum can be driven back to the cathode emitting surfaces and can interact with the LaB_6 substrate. La-terminated crystals exhibit lower work function than B-terminated ones, primarily due to strengthening of the surface dipole by the La-cationic effect [11, 12]. Additionally, this La-enriched topmost layer could reduce the effect of relaxation that increases the work function in the La-terminated crystals (110), (111) and (111). Thus, enrichment of La on the

insert surface due to recycling could explain the enhanced work function found in this work. An alternative mechanism that may also result in enhanced emission is the formation of a different La-B structure with higher La content and therefore potentially lower work function such as LaB₄.

In order to investigate the ionization of lanthanum atoms inside the interior plasma region of the cathode, we used the hollow cathode plasma simulation code OrCa2D [13]. OrCa2D solves conservation laws for three species present in a partially ionized gas: electrons, singly charged xenon ions, and xenon neutrals. A time-splitting method in which all the equations are solved consecutively at every time-step is employed. Inside the cathode, the Navier-Stokes equations for neutral xenon are solved using an implicit backward Euler scheme, which includes the viscous terms. It has been shown that the flow of neutrals transitions from a low to a high Knudsen number downstream of the cathode orifice. Thus, a fluid approximation is not applicable in the cathode plume. Free molecular flow, in which neutrals move in straight paths, is assumed downstream of a specified axial location, typically chosen to be in the cathode orifice where the Knudsen number approaches unity. Mass and momentum conservation is preserved across the transition boundary. The Euler equations for mass and momentum of xenon ions are solved in the entire computational domain. The presence of ion momentum terms was recently included to account for the increased ion densities and currents in high-current cathodes. The effects of ionization, charge exchange and electron-ion collisions are considered in the equations and modeled as source or drag terms. Finally, the plasma parameters for electrons are determined from the solution of the electron energy equation and the combination of the current conservation equation with the vector form of Ohm's law.

We simulated the plasma structure for the nominal cathode configuration at $J_D = 25$ A, $\dot{m}_{Xe} = 14.75$ sccm and two work functions using the temperature measurements reported in this work. The value for the work function of 2.3 eV represents the upper bound of the range of possible work functions for which OrCa2D converges. Above this value, the emitted current can not satisfy charge continuity in the plasma region. The value 2.1 eV was chosen as the lower bound

because the thermionic current emitted was 62 A, which is almost 250% of J_D , and this was considered unrealistic. Results from the OrCa2d code can be used to compute the ionization mean free path (λ) for La and B (Fig. 2.17) using ionization cross section data from Kim [14] and Drawin [15]. Results showed that for this cathode configuration and the specified work function, the mean free path for La is on the order of the orifice diameter, and therefore lanthanum atoms have a high probability of being ionized before they leave the cathode inner region. In contrast, the mean free path for ionization of boron is an order of magnitude bigger than the orifice diameter, thus its ionization rate is negligible.

Fig. 2.18 shows the plasma potential along the centerline of the cathode as simulated by OrCa2D for different work functions (using the anomalous plasma resistivity model [16], for the value 2.67 eV, the temperature was increased above measured values to match the discharge current). Plasma potential can be measured with emissive and Langmuir probes with a few volts precision, which would provide an independent assessment of the work function value with 0.01 eV of precision using OrCa2D simulation results. As we increase the work function while maintaining a constant temperature distribution in the simulations, the net emission decreases according to Eq. 2.1, which requires a decreasing electron return current to maintain the discharge current of 25 A. In this case the code raises the plasma potential so fewer electrons return to the insert from the plasma, which produces the distinctive curves shown. Results for the electron return current J_e for $\phi = 2.1, 2.2$ and 2.3 eV are 33.7, 14.2 and 2.6 A, respectively.

The thermal transient experienced by the cathode with step changes in current that was presented in Fig. 2.6 and the work function predictions shown in Fig. 2.12 are consistent with an evolving emitter surface chemistry due to lanthanum redeposition. During the first steps in increasing current the insert temperature overshoots, which is consistent with cathode transitioning from a higher work function to a lower work function operating point. During the first moments, right after the abrupt change in discharge current is imposed on the cathode by the power supply, the cathode still has a higher work function than the value to which it evolves when steady state is reached at that new operating point. The

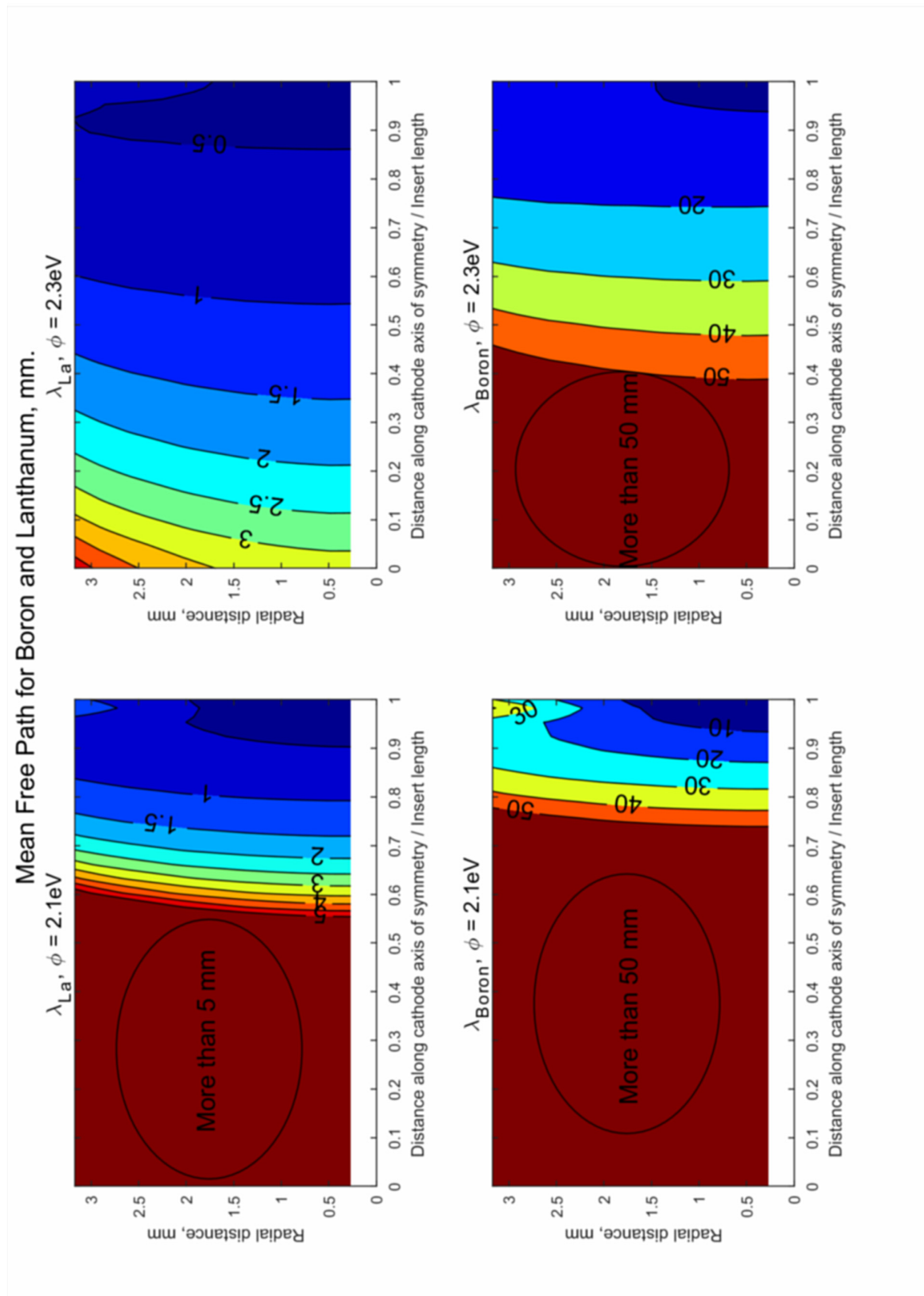


Figure 2.17: Mean free path estimation for boron and lanthanum in the insert region, $J_D = 25\text{ A}$, $\dot{m}_{Xe} = 14.75\text{ sccm}$ and nominal orifice size.

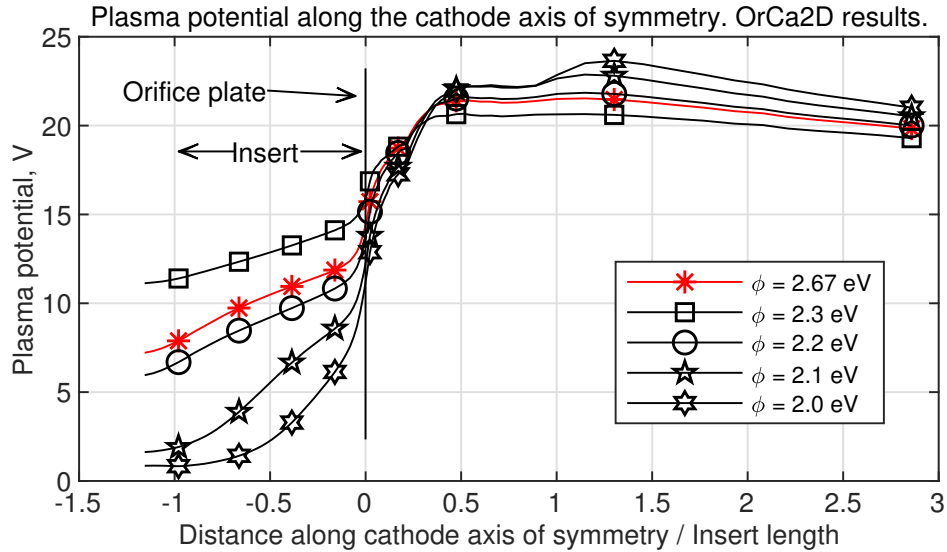


Figure 2.18: OrCa2D simulation results for the plasma potential along the cathode centerline for the nominal configuration at $J_D = 25$ A and $\dot{m}_{Xe} = 14.75$ scm.

temperature will drop after those initial moments due to the reduction in work function that the lanthanum dynamics establishes at that new operating point. We have studied all other small changes for ascending and descending discharge current settings and found that this explanation fits all the observations well with small discharge current steps (less than 5 A).

The La-B system consists of three compounds [17]: LaB_4 , LaB_6 , and LaB_9 . Single phase LaB_6 only exists for atomic ratios of B/La between 6.0 and 6.1 [3] (this last value is slightly dependent on temperature for the temperature range of interest for this work), and it has a purple color in natural or incandescent light. Two phases coexist from B/La ratios between 6.1 and 9. LaB_9 has been reported to appear blue [18], and therefore, in this range the color of the surface depends on the ratio of the two phases, with higher LaB_9 concentration, the color will be closer to dark blue. Two phases also coexist for B/La ratios between 4 and 6.1. In this La-rich phase, the grey color of the surface is proportional to the concentration of LaB_4 [17]. This result suggests that if the insert cools down quickly, we can freeze the surface chemistry to a certain degree and by visual inspection, roughly infer the surface chemistry. In Fig. 2.8 the emitting surface

shows two distinct colors, which suggests La enrichment for the majority of the insert emitting surface and B-rich for a small area close to the orifice plate. We could not find work function measurements for the lanthanum-rich and boron-rich phases in the literature. However, our own work function and chemical analyses suggest that La-rich chemistries have a lower work function than 2.66 eV. There is no definite conclusion about the impact on work function of B-rich chemistries because the carbon presence is very high in the same area where B/La concentration is higher than stoichiometric. Nevertheless, LaB₉ is considered not to have free electrons and therefore to be a semiconductor [3], so a high work function value for this B-rich region is expected. Precise understanding of the different possible phases at the insert surface requires crystallographic analysis of samples exposed to the cathode plasma. We discuss our approach to crystallographic analysis in Chapter 4.

2.5.5.2 Crystallographic texture hypothesis

A polycrystalline sample of LaB₆ contains a random distribution of crystals. Each type of crystal exhibits a different work function and surface energy as a consequence of the specific electron distribution established by the atomic bonds present at the grain surface. Given the high temperatures, long time periods and bombardment by Xe ions, the emitting surfaces of the cathode have enough time to evolve towards their lowest surface energy crystals. Lower surface energy crystals possess lower work function as shown by Uitejtwaal [11]. Crystallographic textures can be studied by X-ray diffraction; this is further described in Chapter 4.

2.5.5.3 Chemical enhancement hypothesis

Several adsorbates have been identified as work function reducers for LaB₆, e.g. Cs [19] and Ba [11]. Therefore, there is a possibility that a chemical that we are not aware of is reducing the work function of the emitter.

2.6 Conclusions

In this work we have obtained temperature measurements of the thermionic emitting surfaces of a working hollow cathode for a variety of steady state and transients operating conditions. These temperatures suggest that LaB_6 hollow cathodes exhibit lower work function than their vacuum cathode counterparts.

The reduction in work function observed in the hollow cathode gas discharge could be explained by the following hypothesis. **(a)** Lanthanum is evaporated from the insert constantly. In a cathode operated in vacuum, most of the evaporated lanthanum would escape, but in a gas discharge its ionization mean free path is small, on the order of the orifice diameter. The neutral La atoms would therefore be ionized and pushed back to the insert surface by the plasma electric field, making the insert emitting surface rich in lanthanum. The degree of enrichment could vary, depending on the global and local operating conditions of the cathode. **(b)** Over a sufficiently long time scale, the crystallography of the polycrystalline sample could evolve and increase the abundance of low work function crystals at the emitting surface. **(c)** A chemical outgassed from the thermionic emitter environment could be adsorbed and reduce the work function of the emitter.

The following evidence is in agreement with the lanthanum recycling hypothesis:

- The fact that the estimated work function for the large orifice cathode is higher than that for the smaller ones, as lanthanum neutrals will have a shorter residence time in the region where they can get ionized.
- The fact that the deeper the cool down, the higher the temperature peak after reignition. When the cathode is shut down, the plasma disappears. Without plasma, lanthanum cannot be ionized. The emitting surface is still hot and lanthanum that is weakly bonded to the surface can easily evaporate. The longer it takes for the reignition to happen, the closer to stoichiometric LaB_6 the surface will get and therefore, the higher the temperature at reignition will be. Another scenario to explain this behavior is related to oxidation of the lanthanum at the emitting surface with water and/or oxygen present in the vacuum vessel.

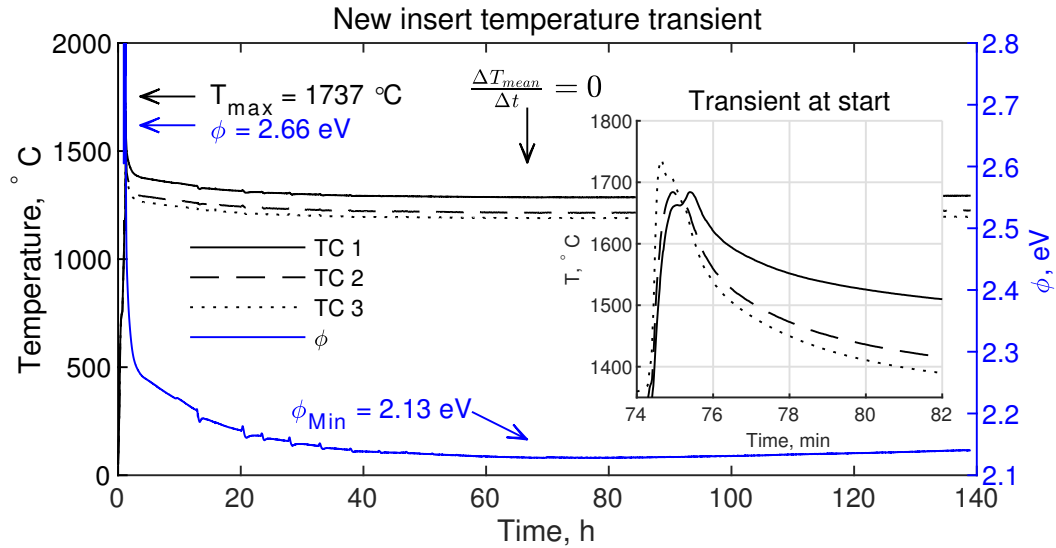


Figure 2.19: Thermal transient and inferred work function for a new insert at $J_D = 25$ A and $\dot{m}_{Xe} = 14.75$ sccm with the nominal orifice. In the inset it is shown the details of the temperature transient during the first few minutes of operation after the discharge power supply has been enabled.

- The long thermal transient for a new insert could also be explained with this model as the stoichiometry is LaB_6 when the insert is new and it will take some time for lanthanum to be deposited and diffuse into the insert. Figure 2.19 shows that the initial temperature after ignition of a new insert is consistent with a work function of 2.66 eV, but drops to 2.13 eV over a time scale of 40 to 50 hr.
- The XPS work function measurements for La-rich stoichiometries with the lowest contamination content.
- The overshoot and undershoot of the temperature transients as J_D is changed.

The following evidence is in agreement with the crystallographic evolution hypothesis:

- The long thermal transient for a new insert could be explained with this model as the relative crystallographic abundance at the surface of the emitter

could evolve over a long time scale because of the effect of the plasma on the emitting surface. Figure 2.19 shows that the initial temperature after ignition of a new insert is consistent with a work function of 2.66 eV, but drops to 2.13 eV over a time scale of 40 to 50 hr.

- The fact that once a new insert has reached steady state, if the cathode is shut down and ignited again, the temperature comes back to the steady state value associated to 2.13 eV. This observation suggests that the work function enhancement has a permanent component, which could be the result of the crystallographic evolution.

The following evidence is in agreement with the chemical enhancement hypothesis:

- The long thermal transient for a new insert could be explained with this model as outgassed chemicals could reduce the work function progressively in the time scale of tens of hours.
- The fact that the work function enhancement seems to have a persistent component after the first 50 hr could be the results of the permanent adsorption of these chemicals.

The precise chemical picture that explains the behavior of the work function given the environment that the hollow cathode produces in the thermionic emitter with xenon gas discharge is still elusive. A combination of their effects is not necessarily mutually exclusive given the ample range of temperature and plasma densities throughout the inner cathode region.

Further surface analyses are necessary to gain more evidence to conclude with certainty which and to what extent the aforementioned hypotheses are responsible for the transient and permanent temperature evolution observed in this work. Because of limited physical access to the emitter and the harsh plasma environment, measuring the chemical composition of the insert inner surface while the cathode is running is not feasible. Instead, we must rely on indirect measurements while the cathode is running and direct crystallographic and chemical measurements before

and after operation. These are ambitious but necessary goals to further explain the elusive mechanism that govern lanthanum hexaboride thermionic emission performance in gas discharges.

2.7 Appendix: Validation of the temperature measurements

2.7.1 Thermocouple accuracy and stability

When using thermocouples to measure temperatures, in order to minimize perturbations to the temperature of a solid at a point of interest it is desirable to use only the thermocouple wires, as their thermal mass and conductivity is the smallest possible for any thermocouple assembly. In our case we cannot use this approach because we observed that boron diffuses in the refractory metal matrix of the thermocouples wires shifting their calibration. The solution to this problem is to use sheaths to isolate chemically the thermocouples wires from possible chemical contaminants. We use tantalum sheaths as they have shown to be robust in this environment.

Boron diffusion from the insert to the tantalum sheath that protects the thermocouples was also a concern. When this happens, the tantalum eventually becomes embrittled and cracks can appear. If that happens, boron has a direct path to contaminate the tungsten rhenium thermocouple wires, which is of great concern as this will shift the calibration of the type C junction. Even if the tantalum sheath is not cracked, boron could potentially diffuse towards the inside of the thermocouples given enough time. However, thorough examination of the thermocouples using a microscope showed that even after 1000 hours of operation they have not developed cracks.

In order to rule out any potential shifts in the response of the thermocouples used in the cathode temperature measurements, we compared the accuracy and stability of these thermocouples used in our experiments with those of new thermocouples in an isothermal oven that we built in-house. These tests showed that the thermocouples used in our experiments performed similarly to new ones, with an accuracy within the expected range. Thus, the thermocouple calibration

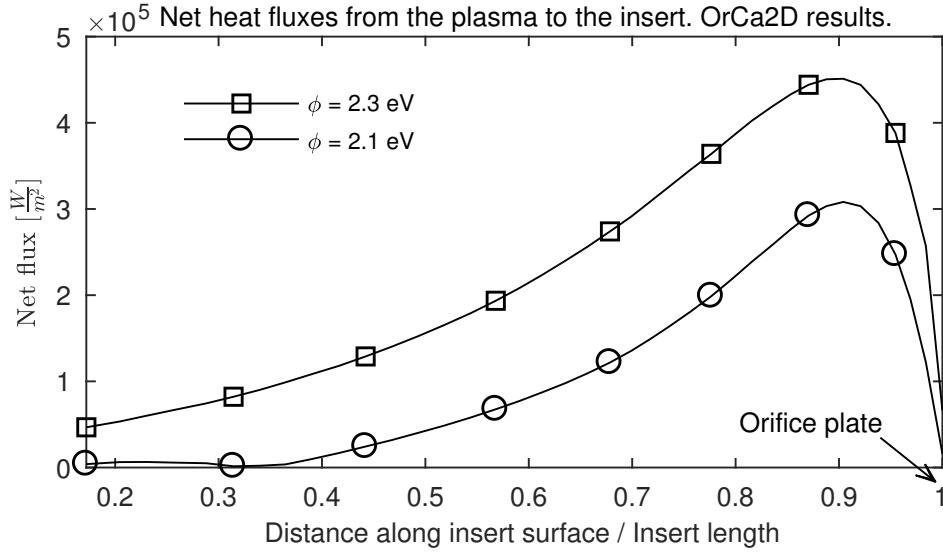


Figure 2.20: Thermal heat fluxes along the insert of the cathode at $J_D = 25 \text{ A}$ and $\dot{m}_{\text{Xe}} = 14.8 \text{ sccm}$ with the nominal orifice.

had not shifted during the experiments.

The agreement between new and used thermocouples removed any doubt related to thermocouple calibration shifts. Boron does not diffuse through the tantalum sheath, at least for these temperatures and the time frame of the observations.

2.7.2 Thermocouple installation impact on the thermal characteristics of the insert.

COMSOL Multiphysics[®] is a multidisciplinary finite element analysis solver. COMSOL thermal simulations were used to study whether the installation of thermocouples disturbs the insert temperature distribution. 3D thermal simulations were necessary to reproduce the actual geometry with high fidelity. A thermal simulation of the entire cathode would have been prohibitively expensive, thus, the simulation approach was based on simulating only the insert. The thermal flux distributions on the insert from the OrCa2D simulations for the cases 2.1 and 2.3 eV were used as the heat flux boundary condition on the insert exterior surface, see Fig. 2.20. The boundary condition for the inner surface was the measured

temperature distribution from the thermocouple data. The other two surfaces of the insert were thermally isolated. First, the insert temperature distribution was computed with the aforementioned boundary conditions for an insert without any thermocouple wells (the undisturbed case). The temperature was extracted at six points in the simulation domain where the thermocouple junctions would be and 1.5 mm away from the junctions, into the insert material. A second model was then constructed with the three thermocouple wells and run with the same boundary conditions. Comparison of the unperforated and perforated inserts showed a difference of less than 2 °C for both thermal flux distributions at the six points.

A third model of the insert with the three thermocouple wells and inserted thermocouples was then studied. Thermocouples were simulated as single component solids with thermal characteristics equal to the real multicomponent structures. The thermocouples protrude from the insert 15 cm, at which point a 100 °C temperature boundary condition was applied. This value was the coldest temperature measured at that point in the actual cathode assembly with a thermocouple during testing. Perfect thermal contact was simulated between the insert and the thermocouples. The thermocouples were allowed to conduct heat out of the insert and the value was recorded. Ambient temperature with which the thermocouples could exchange heat due to radiation was set to 1000, 900, 700, and 500 °C. Non-radiating thermocouples were also simulated. The results from this experiment at the six points agree within 0.6 °C with the temperatures in the intact insert for both thermal fluxes. The total amount of heat that the three thermocouples conduct out of the insert was less than 15% of the heat input to the insert from the plasma, less than 4.2 W per thermocouple.

If the thermocouples have less than perfect thermal contact with the insert, they will measure temperatures lower than the actual temperature of the insert interior. Most of our initial measurements were taken with a thermocouple placement strategy based on inserting the thermocouples and rigidly gluing them to the structure of the cathode. To test the effect of thermal contact, a spring loaded thermocouple assembly was built to ensure good thermal contact by applying a force

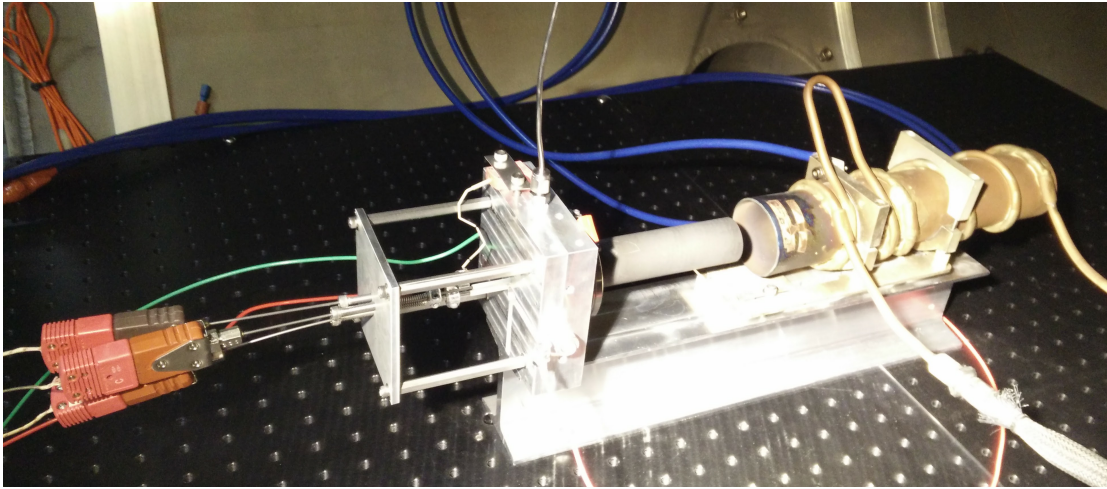


Figure 2.21: Spring loaded thermocouple assembly.

of approximately 23 N between the insert and each thermocouple independently, see Fig. 2.21. In order to maximize the contact area between the thermocouples and the insert, the thermocouples were finished in the shape of half a sphere and the bottom of the thermocouple wells in the insert were machined to match the shape of that sphere. Temperatures measured with this approach at $J_D = 25$ A and $\dot{m}_{Xe} = 14.75$ sccm agreed with the data obtained earlier, indicating good thermal contact with the initial thermocouple fixturing as well. The thermocouples tend to get stuck inside the wells, apparently because evaporated material from the insert fills the gap between thermocouples and the insert.

The cathode was later simulated in full detail assuming axial symmetry. We have learned from those simulations that the radial temperature drop across the insert thickness is, in the worse case scenario, 10 °C.

BIBLIOGRAPHY

- [1] Ioannis G Mikellides et al. “Numerical Simulations of the Partially Ionized Gas in a 100-A LaB6 Hollow Cathode”. In: *IEEE Transactions on Plasma Science* 43.1 (Jan. 2015), pp. 173–184. DOI: 10.1109/TPS.2014.2320876 (cit. on pp. 21, 23).
- [2] Walter H. Kohl. *Handbook of materials and techniques for vacuum devices*. AIP-Press, 1997, pp. XVI, 498. ISBN: 978-1563963872 (cit. on pp. 21, 23).
- [3] Edmund K Storms and B. A. Mueller. “A study of surface stoichiometry and thermionic emission using LaB6”. In: *Journal of Applied Physics* 50.5 (May 1979), pp. 3691–3698. DOI: 10.1063/1.326323 (cit. on pp. 37, 48, 49).
- [4] Matthias Richter Paul Nunez Christopher W. Roske. “Characterization of Electronic Transport through Amorphous TiO2 Produced by Atomic-Layer Deposition”. In: *in review* (2019) (cit. on p. 41).
- [5] W. R. Salaneck. “Photoelectron spectroscopy of polyconjugated polymer surfaces and interfaces”. In: *Reports on Progress in Physics* 54.9 (Sept. 1991), pp. 1215–1249. DOI: 10.1088/0034-4885/54/9/002 (cit. on p. 41).
- [6] C Oshima et al. “Thermionic work function of LaB 6 single crystals and their surfaces”. In: *Journal of Applied Physics* 48.9 (Sept. 1977), pp. 3925–3927. DOI: 10.1063/1.324266 (cit. on p. 43).
- [7] T. Takahashi, H. Tokailin, and T. Sagawa. “Angle-resolved ultraviolet photoelectron spectroscopy of the unoccupied band structure of graphite”. In: *Physical Review B* 32.12 (1985), pp. 8317–8324. DOI: 10.1103/PhysRevB.32.8317 (cit. on p. 43).
- [8] James E Polk et al. “Tungsten and barium transport in the internal plasma of hollow cathodes”. In: *Journal of Applied Physics* 105.0021-8979 (2009), pp. 113301–13. DOI: 10.1063/1.3111970 (cit. on p. 44).
- [9] James E Polk et al. “The effect of cathode geometry on barium transport in hollow cathode plasmas”. In: *Journal of Applied Physics* 115.18 (May 2014), p. 183301. DOI: 10.1063/1.4873168 (cit. on p. 44).
- [10] Hiroyuki Kawano. “Effective work functions for ionic and electronic emissions from mono- and polycrystalline surfaces”. In: *Progress in Surface Science* 83.1-2 (Feb. 2008), pp. 1–165. DOI: 10.1016/j.progsurf.2007.11.001 (cit. on p. 44).

- [11] M A Uijttewaal, G. A. de Wijs, and R. A. de Groot. “Ab Initio and Work Function and Surface Energy Anisotropy of LaB 6”. In: *The Journal of Physical Chemistry B* 110.37 (Sept. 2006), pp. 18459–18465. DOI: 10.1021/jp063347i (cit. on pp. 44, 49).
- [12] Jian Wang et al. “Work functions of metal hexaborides: Density functional study”. In: *Modern Physics Letters B* 32.2 (2018), pp. 1–8. DOI: 10.1142/S0217984918500070 (cit. on p. 44).
- [13] Alejandro Lopez Ortega, Ioannis G. Mikellides, and Benjamin Jorns. “First-principles modeling of the IAT-driven anomalous resistivity in hollow cathode discharges II: Numerical simulations and comparison with measurements”. In: *52nd AIAA/SAE/ASEE Joint Propulsion Conference*. Reston, Virginia: American Institute of Aeronautics and Astronautics, July 2016. DOI: 10.2514/6.2016-4627 (cit. on p. 45).
- [14] Yong Ki Kim and Philip M. Stone. “Ionization of boron, aluminum, gallium, and indium by electron impact”. In: *Physical Review A - Atomic, Molecular, and Optical Physics* 64.5 (2001), p. 11. DOI: 10.1103/PhysRevA.64.052707 (cit. on p. 46).
- [15] H. -W. Drawin. “Zur formelmabigen Darstellung der Ionisierungsquerschnitte gegenüber Elektronenstob”. In: *Zeitschrift fur Physik* 164.5 (Oct. 1961), pp. 513–521. DOI: 10.1007/BF01378424 (cit. on p. 46).
- [16] Benjamin A. Jorns, Ioannis G. Mikellides, and Dan M. Goebel. “Ion acoustic turbulence in a 100-A LaB6 hollow cathode”. In: *Physical Review E - Statistical, Nonlinear, and Soft Matter Physics* 90.6 (2014), pp. 1–10. DOI: 10.1103/PhysRevE.90.063106 (cit. on p. 46).
- [17] Edmund Storms and Barbara Mueller. “Phase relationship, vaporization, and thermodynamic properties of the lanthanum-boron system”. In: *The Journal of Physical Chemistry* 82.1 (Jan. 1978), pp. 51–59. DOI: 10.1021/j100490a014 (cit. on p. 48).
- [18] Robert W. Johnson and A. H. Daane. “THE LANTHANUM—BORON SYSTEM 1”. In: *The Journal of Physical Chemistry* 65.6 (June 1961), pp. 909–915. DOI: 10.1021/j100824a004 (cit. on p. 48).
- [19] S.A. Chambers, P.R. Davis, and L.W. Swanson. “Cesium and oxygen coadsorption on LaB6 single crystal surfaces”. In: *Surface Science* 118.1-2 (June 1982), pp. 93–102. DOI: 10.1016/0039-6028(82)90016-4 (cit. on p. 49).

HOLLOW CATHODE THERMAL MODELLING AND
SELF-CONSISTENT PLASMA SOLUTION; WORK FUNCTION
EVALUATION FOR A LaB_6 CATHODE AND TWO STEP
NEUTRALIZATION MODELLING.

3.1 Abstract

Self-heating hollow cathodes are central components in modern electric thrusters. The plasma discharge inside these devices heats the internal components, thus maintaining the temperatures required for electron emission. Precise knowledge of the physical phenomena governing hollow cathode operation, specifically, their thermionic emission characteristics, is key to predicting their lifetime. A new simulation platform has been built to couple plasma and thermal physics models of the self-heating hollow cathode to produce a self-consistent solution. The plasma solution is provided by JPL's 2D axisymmetric code OrCa2D and the corresponding cathode temperature distribution is calculated using COMSOL's Multiphysics[®] heat transfer module. The platform allows investigation of the sensitivity of different variables that govern the behavior of the three dominant processes involved in cathode operation – thermal, plasma and chemical. A self-consistent solution has been found for a LaB_6 hollow cathode operating at 25 A and 13 scm when classical assumptions are implemented in the model, i.e., resonant neutralization, homogeneous work function along the emitter, and 100% energy accommodation of the returned ion flux to the internal cathode surfaces. However, the emitter temperature from the converged solution does not agree with experimental temperature measurements. We studied the effect of four potential explanations for the disagreement: sensitivity of the self-consistent solution to the thermal model or measured keeper voltage of the cathode, variable work function distribution along the insert, energy accommodation coefficient, and neutralization model for the ion return current. We conclude that the most likely cause for the

disagreement is the lack of fidelity of the classical resonant neutralization model and the need to account for energy accommodation. Importantly, we demonstrate that an agreement between simulated and experimental results can be found when incorporating a two step neutralization mechanism and energy accommodation for the ions impacting the cathode surfaces. This mechanism could govern the neutralization in other cathode technologies where low work function emitters are employed. This approach constitutes the first successful attempt to simulate a LaB₆ hollow cathode with 2D axisymmetric models for the plasma and thermal model of the cathode (where the thermal model is experimentally validated independently of the plasma) that are self-consistently coupled. Previous attempts to couple plasma and thermal solutions have used low-fidelity 2D thermal models that were not independently validated [1, 2]. This coupled simulation methodology enables us to better estimate the work function of running LaB₆ hollow cathodes. We find that the work function for the aforementioned operating point is ~ 2.25 eV, which is significantly lower than previous estimates[3], and implies a better than expected cathode material performance.

3.2 Introduction

Reaching further, going faster and delivering heavier payloads are the ultimate goals of the design of any space vehicle. In order to improve the current technical capabilities and enable more ambitious deep space missions, NASA is investing in high power electric propulsion systems. Scalable arrays of Hall thrusters are at the heart of these propulsion systems.

Hollow cathodes are among the basic components necessary for Hall thruster operation, and therefore cathode lifetime is a major determinant of thruster lifetime. There are several cathode failure processes which are still not fully understood and a better understanding of the different physical mechanisms that govern cathode discharges is necessary. Thermionic emission of electrons is the most fundamental mechanism of the cathode discharge. Thermionic emission is strongly dependent on the work function of the emitting surface of the cathode. Cathodes composed of a porous tungsten emitter impregnated with barium-calcium-aluminate mixture

are the baseline for the Advanced Electric Propulsion System (AEPS) that is under development by the NASA Glenn Research Center (GRC) and the Jet Propulsion Laboratory (JPL) with Aerojet Rocketdyne as an industrial partner. This technology maintains a relatively low work function during the operation of the cathode, conferring a long lifetime. LaB₆ cathodes are a promising alternative with several advantages over tungsten cathodes, which include emitting surface self-cleaning from oxides, greater resilience to contamination, and low work function. A low work function is essential for electron emitters because it enables operation at a lower temperature for a given emission current, which reduces the evaporation of the emitting material and thus increases their useful lifetime.

Hollow cathodes are thermionic emitters classically modelled with the Richardson-Dushman law [4] (Eq. 3.1). This law relates temperature, emission current density of electrons and work function.

$$j_{\text{ther}}(\phi, T) = D T^2 \exp\left(\frac{-e(\phi - \phi_{\text{Schottky}})}{k_{\text{B}}T}\right), \quad (3.1)$$

where T is the temperature at the emitting surface, $D = 29 \text{ A/cm}^2 \text{ K}^2$, k_{B} is the Boltzmann constant, ϕ is the work function of the material, ϕ_{Schottky} is the reduction in the work function due to the Schottky effect Eq. 3.2 [5] and e is the electron charge.

$$\phi_{\text{Schottky}} = \sqrt{\frac{e|\vec{E}_{\text{wall}}|}{4\pi\epsilon_0}}, \quad (3.2)$$

where \vec{E}_{wall} is the external electric field value at the interface with the emitter wall and ϵ_0 is the vacuum permittivity.

Several phenomena must be taken into account when studying the current density capability of a hollow cathode, namely **(1)** the return current of electrons and ions to the emitting surface, **(2)** the Schottky effect, **(3)** space charge limitations, **(4)** temperature variation along the emitting surfaces and **(5)** work function variation due to evolution of the chemistry and/or crystallographic structure of the emitting surfaces.

In order to estimate the current density a cathode is capable of, a simple analysis can be done with the following assumptions:

1. No net return current (contribution from plasma electrons and ions)
2. $\phi_{\text{Schottky}} = 0$
3. Not space charge limited current
4. Uniform temperature along the emitter
5. Uniform work function along the emitter

Fig. 3.1 shows a study of thermionic emission current density with temperature and ϕ as a parameter for a range of temperatures between 1200 and 1600 °C for LaB₆. The emission current density for a 2.54 cm long insert with inner diameter 6.35 mm and net discharge current of 25 A is shown, as well as the range if a net return current of $\pm 10\%$ and $\pm 15\%$ are considered. The temperature of the insert for this configuration with a xenon flow rate of 13 sccm has been measured experimentally [6] and the range is shown as well.

This simplified example shows that the return current and temperature distribution are of great importance. In fact, all of the aforementioned physical details must be considered to develop a more accurate description of LaB₆ hollow cathode operation. We can observe though that the work function for LaB₆ hollow cathodes operated with an internal gas discharge must be lower than the previously reported value of 2.66 eV [3] for polycrystalline LaB₆ operating in vacuum. Our previous estimate of the work function for this operating point was ~ 2.19 eV, where assumptions 1, 2, 3 and 5 were used and the temperature profile along the insert ($T_{\text{insert}}(z)$) was extrapolated from three thermocouple measurements using a second degree polynomial fit.

In order to improve the determination of the work function in a LaB₆ hollow cathode that has reached steady state, it is of paramount importance to accurately determine the net return current (considering space charge limitations), $T_{\text{insert}}(z)$,

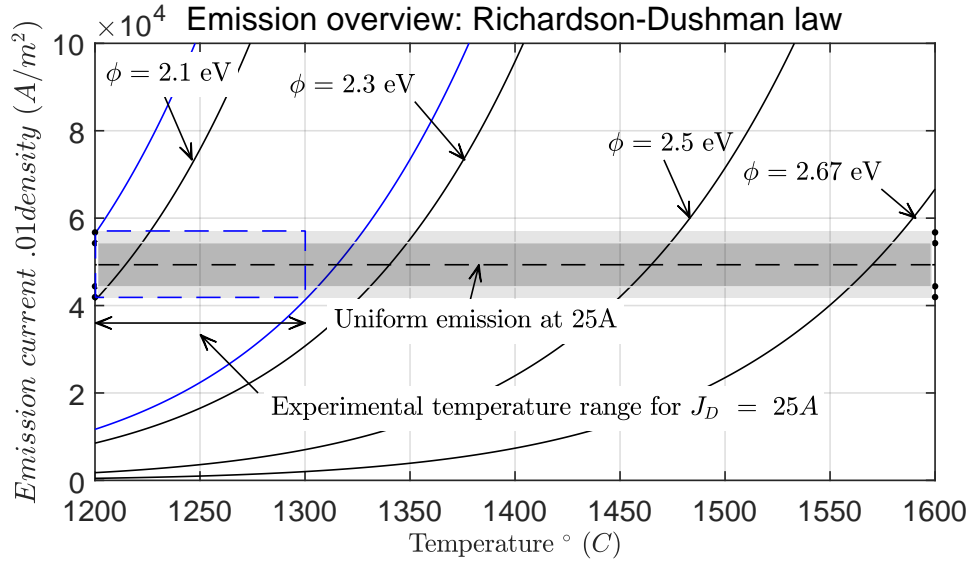


Figure 3.1: Thermionic emission sensitivity analysis for Richardson-Dushman law. Uniform emission at $J_D = 25$ A is shown with a $\pm 10\%$ net return current (dark shaded area) and a $\pm 15\%$ net return current (lighter shaded area). Experimentally measured temperature range of the insert at $J_D = 25$ A is also shown, as well as the range of work function possible for it.

and the impact of the Schottky effect on the work function. If all of those variables were perfectly known, the work function could be determined with higher accuracy than in our previous work. In the present work, we have employed the JPL in-house plasma solver OrCa2D to find the plasma structure inside the cathode, which provides a quantification of the net return current and Schottky effect.

The question of how to accurately determine the temperature distribution is still challenging to answer. Two experimental approaches have been employed to determine the temperature in our previous work; type C thermocouples and sapphire fiber optic-based ratio pyrometry. Even though we continue to improve those techniques with more accurate calibrations, the temperature distribution along the emitting surfaces has uncertainties that impact the proper determination of thermionic emission in a significant manner.

With regards to the thermocouple approach, it is only feasible to measure

the temperature at a few locations along the emitting length of the insert, and then the temperature can be interpolated between those points. However, it is difficult to make thermocouple measurements of the temperature at the ends of the insert, which impacts the estimation of the actual shape of $T_{\text{insert}}(z)$. Furthermore, type C thermocouples have a 1% inherent tolerance. The fiber-optic approach also poses challenges in determining $T_{\text{insert}}(z)$. Fiber-optics depend on their calibration and a view factor correction method to produce the most accurate temperature profile. When they are used with LaB_6 cathodes, the fiber-optic probes might get coated with La or B, which impairs their optical properties and shifts their calibration. In addition, accurate view factor correction of the unfiltered signal relies on knowledge of the temperature distribution of all the surfaces within view of the insert, data which are not available.

We have developed a third method to improve our understanding of the temperature distribution along the insert and the plasma structure inside hollow cathodes which relies on a self-consistent simulation of plasma heat loads and cathode thermal behavior. A high fidelity thermal model of the cathode built using the COMSOL Multiphysics[®] heat transfer module was experimentally validated and coupled with the in-house OrCa2D plasma solver. An iterative coupling of the two codes is possible due to the slower time scale of the thermal response of the cathode compared to the much faster plasma behavior. Using this coupled OrCa2D-COMSOL solver, we can simulate the temperature distribution that is self-consistently produced at steady state during cathode operation for any geometry, materials, and operating conditions that we establish. Combining the OrCa2D-COMSOL coupled solver with the aforementioned experimental methods brings a significant improvement to the cathode temperature determination problem. We can now account for the return current of ions and electrons, space charge limitations, temperature distribution, and work function variations along the emitter. In addition, we can include the effect of the plasma electric field in lowering the effective work function at the interface between plasma and emitter.

A self-consistent solution has been found for a LaB_6 hollow cathode operating at 25 A and 13 sccm when classical assumptions are implemented in the model,

i.e., resonant neutralization, homogeneous work function along the emitter, and 100% energy accommodation of the returned ion flux to the internal cathode surfaces. The emitter temperature from the converged solution does not agree with experimental temperature measurements, however. The self-consistent solution provided a temperature distribution about 150 °C higher than the experimentally measured temperatures [6].

We studied the effect of four potential explanations for the disagreement: sensitivity of the self-consistent solution to the thermal model or measured keeper voltage of the cathode, variable work function distribution along the insert, energy accommodation coefficient, and neutralization model for the ion return current.

Variable work function distribution

In our previous work we observed a color gradient in an insert used for hundreds of hours in a hollow cathode, which was removed from the cathode after it was shut down, cooled down to ambient temperature and exposed to the atmosphere [6]. This color gradient suggests a possible chemical evolution while the cathode is in operation. Given the dependency between chemical state at the surface of the insert and work function, we hypothesised that the chemical composition, and hence the work function, might not be constant along the insert.

To investigate the work function distribution along the insert, we studied four different profiles (including two linear and two quadratic) in the self-consistent solution. Results showed that the temperature distribution of the insert is quite insensitive to the work function profile. Therefore, we conclude that this hypothesis cannot explain the disagreement between the self-consistently computed insert temperature and the experimentally measured one.

Thermal model and keeper voltage sensitivity

We considered that the self-consistent solution might be sensitive to some parameter used to define the thermal model or the plasma solution. We studied the effect on the self-consistent solution of two parameters – the cathode thermal losses and the keeper voltage. The results from these experiments ruled out both parameters as factors that could explain the discrepancy between simulated and experimental values.

Inelastic ion-surface interaction

For the cathode used in this study and the operating condition chosen, the most significant contribution to the heat fluxes from the plasma to the cathode structure are the ones produced by the return current of ions. Those returning ions collide inelastically against the surface of the emitter, releasing their kinetic energy on it. This process does not necessarily release all the energy of the incoming ions to the surface, but can result in neutralized ions bouncing off the surface with some energy left. We studied the effect of the energy accommodation factor, which is the fraction of ion kinetic energy deposited on the surface, on the self-consistent solution and concluded that we need an energy accommodation factor of about 50 % for all the surfaces in the cathode in order to find a self-consistent solution that agrees with the experimentally measured values. The energy accommodation factor for the $\text{Xe}^+ (<50 \text{ eV})$ - LaB_6 and $\text{Xe}^+ (<50 \text{ eV})$ - W has not been reported in the literature as far as we are aware. We explain that the energy accommodation factor is primarily influenced by the mass ratio of the impinging ions and the atoms in the surface. Using experimentally measured values for the energy accommodation factors for gas-surface system with similar mass ratios as the Xe - LaB_6 and Xe - W systems, we concluded that the energy accommodation factor for either case cannot be less than 80 %. We report that while an energy accommodation factor less than 100 % helps get closer to the experimentally measured temperatures, it is not necessarily the only contributor to the disagreement between experiments and simulation results.

Neutralization model

Finally, we studied the effect of a two step neutralization model for the ion return flux to the emitter. The model includes resonant neutralization to the first excited state of xenon, followed by Auger de-excitation to the ground state. During the de-excitation of the Xe atoms, electrons in the solid gain energy and a portion of them per neutralized Xe ion will have enough energy to be emitted from the solid into the plasma sheath. These electrons will then be accelerated by the sheath into the plasma. There is no data available in the literature for the electron yield for the $\text{Xe}^+(\lt 50 \text{ eV})\text{-LaB}_6$ system. We modelled the probability of an electron leaving the solid into the sheath with γ_{Auger} and computed the necessary value to match the experimentally measured insert temperature. Results show that assuming 100% energy accommodation for the return current of ions, $\gamma_{\text{Auger}} = 0.85$ is necessary to find an agreement with the experimentally measured temperatures of the insert. In this case the work function yielded by the model is 2.27 eV. Similarly, we found that when the energy accommodation is 80%, γ_{Auger} needs to be 0.5, and in this case the work function is 2.25 eV.

3.3 Methods

3.3.1 Overview of the coupled self-consistent simulation approach

The overall strategy used to couple both codes can be seen in Fig. 3.2. MATLAB[®] 2018a was used as the main framework from which OrCa2D and COMSOL simulation packages are controlled, and where the coordination between models is established. The general process of finding a plasma solution which is consistent with the thermal characteristics of the hollow cathode requires several global simulation/iteration steps.

A global iteration step starts when OrCa2D is provided with an initial guess for the temperature distribution along the insert and the plasma solution is then obtained for the particular operating point. At that point, OrCa2D produces the heat fluxes to the walls of the cathode from electrons and ions. Those fluxes are then input into the COMSOL heat transfer simulation package where the

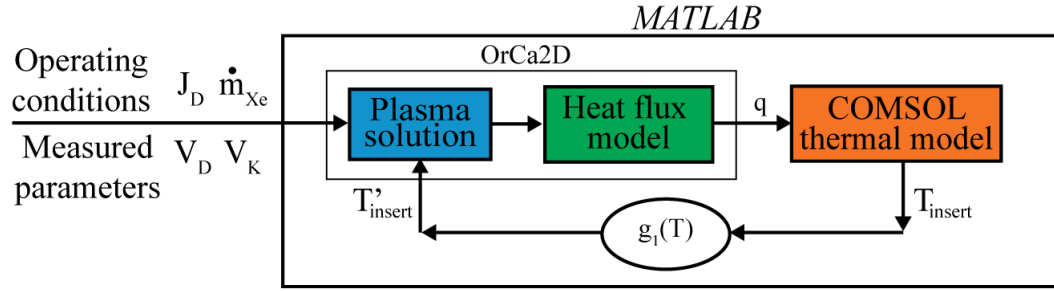


Figure 3.2: Overview of the strategy used to compute the coupled solution that includes plasma and thermal models.

updated temperature of the insert is obtained. Then, MATLAB[®] compares the temperature provided to OrCa2D at the beginning of the global iteration step with the temperature profile that COMSOL has generated using the plasma heat fluxes. If they are not the same, the accommodating function $g_1(T(z))$ shown in Fig. 3.2, Eq. 3.3 creates a new temperature profile to input into OrCa2D, which is closer to the one that COMSOL computed in the previous global iteration step.

$$T'_{i+1}(z) = \begin{cases} T_i(z) & \text{if } |T_i(z) - T'_i(z)| < dT_{\text{cap}} \quad \forall z \\ T'_i(z) + (T_i(z) - T'_i(z)) / F & \text{if } |T_i(z) - T'_i(z)| \geq dT_{\text{cap}} \quad \forall z \end{cases} \quad (3.3)$$

where $T = T_{\text{insert}}$, $dT_{\text{cap}} = \text{parameter}$,
and $F = \max(|T_i(z) - T'_i(z)|) / dT_{\text{cap}}$

In order to input $T'_{\text{insert}}(z)$ into OrCa2D, a fourth order polynomial fit is used. Then, a new global iteration can be executed. The code finishes when the temperature input into OrCa2D and the one computed by the COMSOL heat transfer module differ by less than a small tolerance. The root mean square error (RMSE) of both profiles is computed and convergence is defined when this value is less than 10 °C. At that point, we conclude that the plasma solution is consistent with the thermal model of the cathode. With this self-consistent solution we are able to capture the details of the shape of $T_{\text{insert}}(z)$, along with a high fidelity estimate of the net return current and Schottky effect [5].

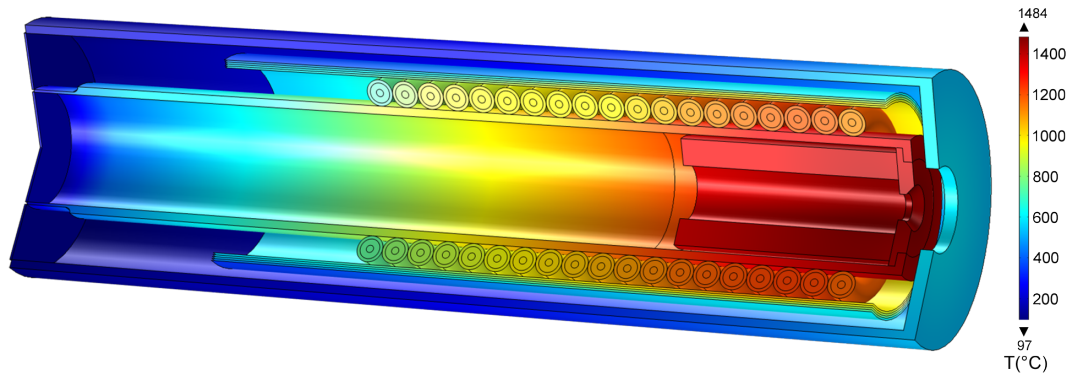


Figure 3.3: Temperature distribution created with COMSOL (example).

3.3.2 Hollow cathode thermal model

The thermal model used in this study was created using COMSOL Multiphysics[®] V5.3a. The geometry was built using SOLIDWORKS[®] 3D CAD 2016 and imported into COMSOL. Two “Physics” modules were used to model heat transfer by conduction and radiation between components, “Heat Transfer with Surface-to-Surface Radiation” and “Heat Transfer in Thin Shells”. The meshing approach was based on a parameterization using a combination of maximum sized elements in the edges of the domains and “extremely fine refinement” for the interior of the domain. The thermal model was written in batch mode in Java, enabling MATLAB[®] to dynamically create and execute thermal models with any configuration (geometry, material properties, boundary conditions, mesh configuration and refinement and modeling details: parameters used for thermal contact, convergence criteria, etc). An example of the solution of such a strategy is shown in Fig. 3.3

3.3.2.1 Geometry and materials

The geometry of the cathode thermal model is a 2D axisymmetric approximation of the actual cathode geometry. The different parts and materials used are shown in Fig. 3.5 and Table 3.1. The mounting plate (Part 7) is a fictitious boundary at which a fixed temperature equal to that measured at a corresponding point on the cathode tube is specified. In reality the cathode is attached to an aluminum block

0.5" further upstream.

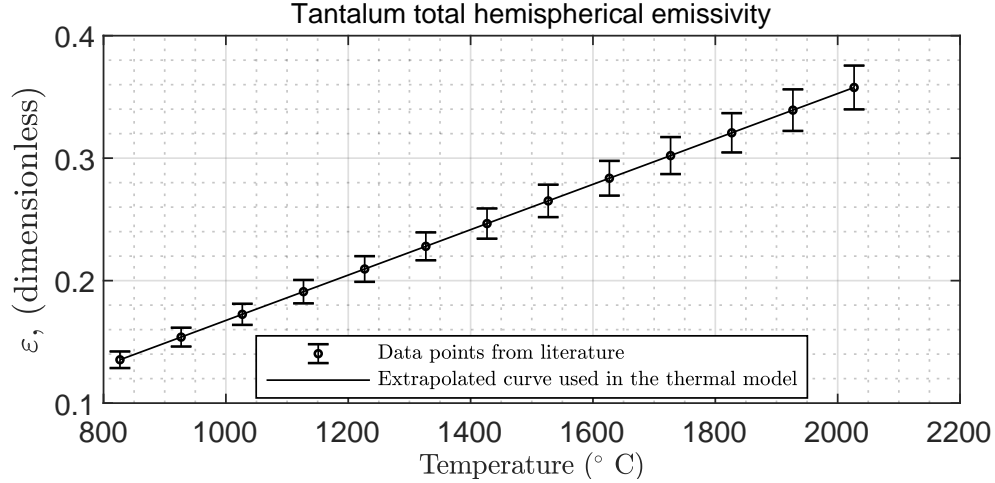


Figure 3.4: Ta total hemispherical emissivity from [7].

The heater coil is manufactured with an inner diameter slightly smaller than the cathode tube outer diameter so it presses against the tube when installed around it. Because the heater and cathode tube are both made of pure Ta and are pressed together, during operation at high temperature they eventually fuse to each other. This interaction between the two parts was modelled with a point contact between the individual heater coils and the cathode tube. Thermal conductivity and total hemispherical emissivity values for the different materials used in the cathode construction were obtained from the literature and the references are shown in Table 3.1. Tantalum total hemispherical emissivity is shown in Fig. 3.4.

3.3.2.2 Thermal modelling

In the present work the thermal model of the cathode assumes axisymmetry (2D model), as shown in Fig. 3.6. The only component that is not axisymmetric in reality is the heater, which is made from a long cable, thus, there is heat conduction along the heater length. In the model the heater is made of 19 tori arranged along the axis of symmetry of the cathode, starting from the one that is most downstream. The heater consists of three components, the inner wire, insulator

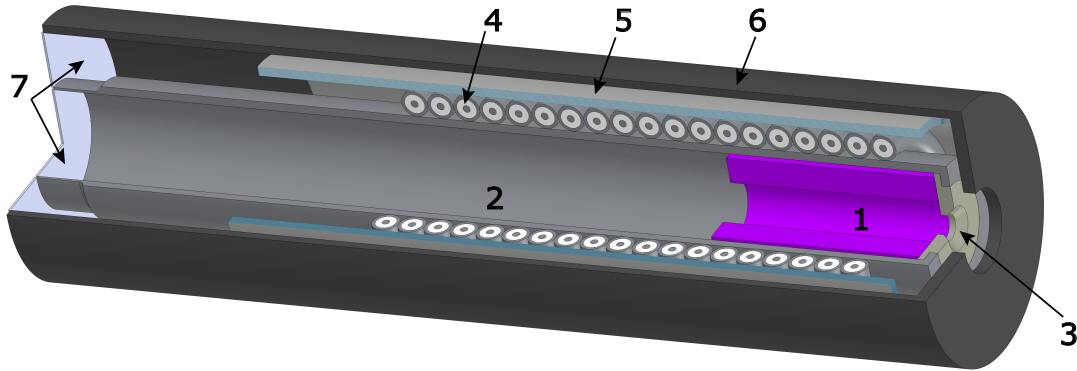


Figure 3.5: Cathode geometry.

Table 3.1: Summary: cathode parts and materials

Part number	Name	Material	Material properties
1	Insert	LaB ₆	[8, 9]
2	Cathode tube	Ta	[7, 10]
3	Orifice plate	W	[10, 11, 12, 13]
4	Heater	Ta and Al ₂ O ₃	[7, 10, 14]
5	Radiation shielding	Ta	[7, 10]
6	Keeper	C	[15, 16]
7	Mounting plate	Al 6061	[17, 18]

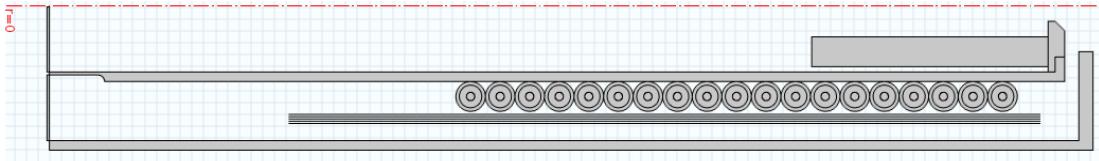


Figure 3.6: Axisymmetric model of the hollow cathode.

and outer sheath. It was assumed that those three components are in perfect thermal contact, as they are manufactured with a swaging process.

The insert is assumed to be non-porous and in perfect thermal contact with the orifice plate. The orifice plate was modelled as having perfect thermal contact with the cathode tube. The radiation shielding was modelled with 5 layers instead of 10 as it is in reality. This reduction in the number of shields is a way to

approximate the thermal contact between layers, which we found was necessary to match measured temperatures. Each radiation shield was modelled using “Heat Transfer in Thin Shells” where the governing equations associated with the thermally thin approximation are implemented (no temperature gradient across the layers). The radiation shielding used was 0.001" thick. Additionally, the radiation shields were observed to have darkened during cathode operation. We believe this darkening is associated to the adsorption of a chemical during the high temperature operation of the cathode. In order to account for this darkening effect on the radiation properties of the shields, we added 0.2 to the literature value for the emissivity curve of Ta (ϵ_{Ta}) on these layers, this configuration is named the *baseline* thermal model. The sensitivity to this parameter was studied with a second model which assumed the emissivity was higher by 0.4 (i.e., an additional 0.2 increase above values used in the *baseline* case), see Results section 3.4. The graphite keeper emissivity was assumed to be unity.

All the components were modelled from the radiation standpoint as diffuse gray surfaces (no wavelength dependence of emissivity). The hemicube approximation was used to compute the form factors, taking into account shadowing effects. A value of 256 (COMSOL default) was used for the radiation resolution, a parameter which controls the accuracy of the method [19, 20, 21]. We are using axisymmetric geometry, therefore, the 2D geometry needs to be virtually revolved to create a 3D one where values for the mutual irradiance and view factors can be computed. 128 azimuthal sectors (COMSOL default) were used for this process. The thermal solution sensitivity was studied against grid refinement (Fig. 3.7), radiation resolution, and azimuthal sectors. The outcome of that analysis showed that the temperature distribution does not change significantly with increasing radiation resolution and the number of azimuthal sectors, see Fig. 3.8 and 3.9. The values used for the *baseline* thermal model are shown in the figures.

3.3.2.3 Thermal fluxes – the interface with the plasma solver

Heat from the plasma is input into the model as heat fluxes along the surfaces shared by both codes. These surfaces are highlighted in red in Fig. 3.10. The

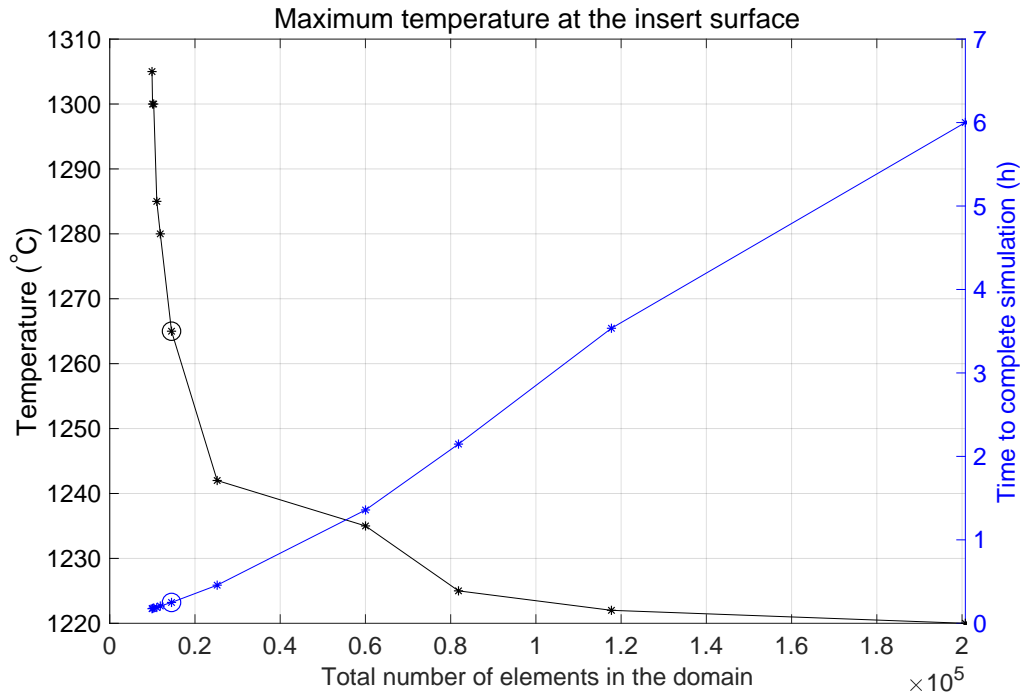


Figure 3.7: Dependence of the maximum temperature of the insert surface with the total number of elements in the Comsol thermal model.

approach followed for this interaction is based on extracting the heat fluxes from the plasma at every grid point of the plasma boundary and interpolating their value at every grid point of the thermal model boundary. The total heat input into any surface was used to check the success of the approach.

3.3.3 Thermal model validation

The COMSOL thermal model was validated with measured temperatures at five cathode heater power levels ($P = 124.53, 157.19, 192.62, 229.9, 267.78$ W, see Fig. 3.12). Seven thermocouples were used to measure the temperature in the positions shown in Fig. 3.11. Two of those thermocouples (TC6 and TC10) provided boundary conditions for the thermal model, the other five were used to compare experimental with simulated thermal results.

The heater was powered with a DC power supply. The current was measured

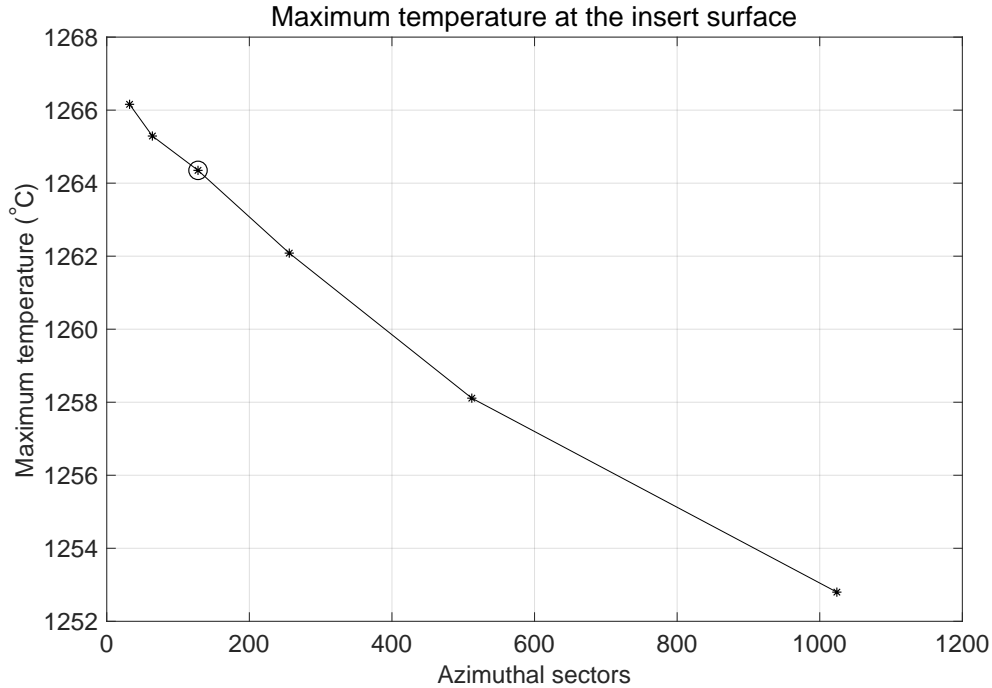


Figure 3.8: Dependence of the maximum temperature of the insert surface with the number of azimuthal sectors used in the COMSOL thermal model.

with a shunt placed along the heater circuit which provides 10 mA accuracy. The voltage of the heater was measured at the vacuum feedthrough. There is approximately 2 m of cable connecting the feedthrough to the heater. The resistance of that cable was measured and used to correct for the voltage drop along the cables when the heater is powered. The voltage measurement has an accuracy of 50 mV. A Keithley 2400-C sourcemeter was used to calibrate the data acquisition system. In the thermal model, the distribution of power over the heater was modeled by calculating the Joule heating produced in the inner conductor of each coil using the temperature-dependent electrical resistivity [22] for a given current. The current was varied until the sum of the power dissipated in the coils matched the experimental value. Thus, the current necessary to match the measured total power is self-consistently obtained during the thermal model simulation and a more realistic distribution of power is simulated. The error between simulated and measured current was between 4.3% and 7.9%.

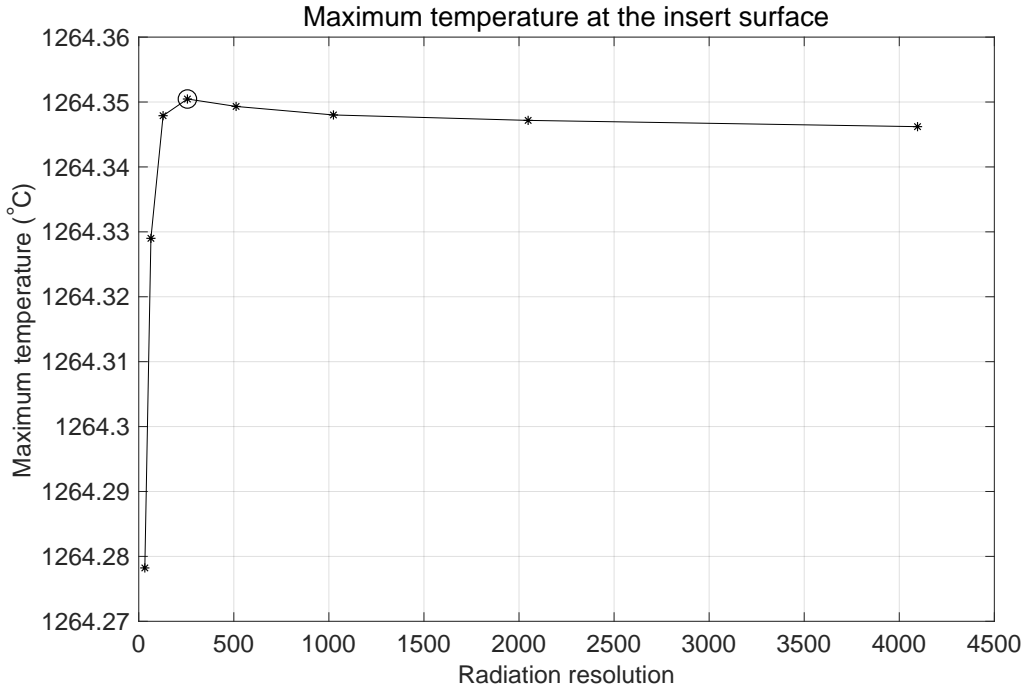
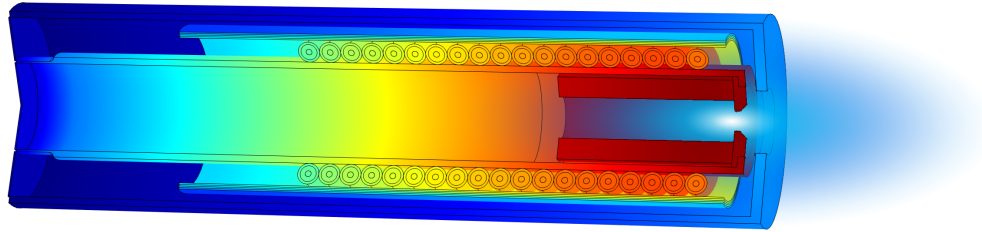


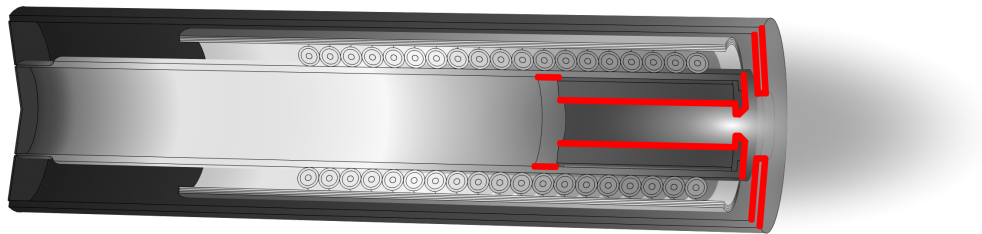
Figure 3.9: Dependence of the maximum temperature of the insert surface with the radiation resolution used in the Comsol thermal model.

There is a section of the heater (see Fig. 3.11) that is not included in the thermal model but consumes part of the heater input power. The power associated with that part of the heater was estimated using a linear variation of the temperature along the heater lead and electrical resistivity from [22]. This calculation yielded 5% as the maximum percentage of the power associated with the part of the heater not modelled. In order to take into account the effect of this portion of the power input, five more thermal simulations were performed with power reduced by 5% from the measured power. With those extra five temperature distributions we can bound the effect of not including that portion of the heater in the model.

The results of the described thermal model validation process can be observed in Fig. 3.12. There are 10 plots in total. The five plots on the top show absolute temperature for TC1, TC2, TC3, TC11, TC12 for the five power levels. The



(a) Thermal model results and a schematic representation of the internal plasma.



(b) Surfaces where the plasma heat fluxes are input into the thermal model geometry (highlighted in red).

Figure 3.10: Representation of the cathode thermal model, plasma and surfaces at the interface.

experimental results are shown in blue (temperature measured with thermocouples in the cathode). The COMSOL thermal model results are shown in red. The results of the COMSOL thermal model when 95% of the heater power is input instead of the experimentally used power levels are shown in green. The five plots on the bottom show the differences between simulated and experimental results. Bar plots show the rated thermocouple accuracies.

Assuming the thermocouples measured the correct temperature value, the COMSOL thermal model results for TC1, TC2 and TC3 produce a maximum of ~ 60 °C absolute error. This error is reduced to a maximum of ~ 31 °C for TC11 and TC12.

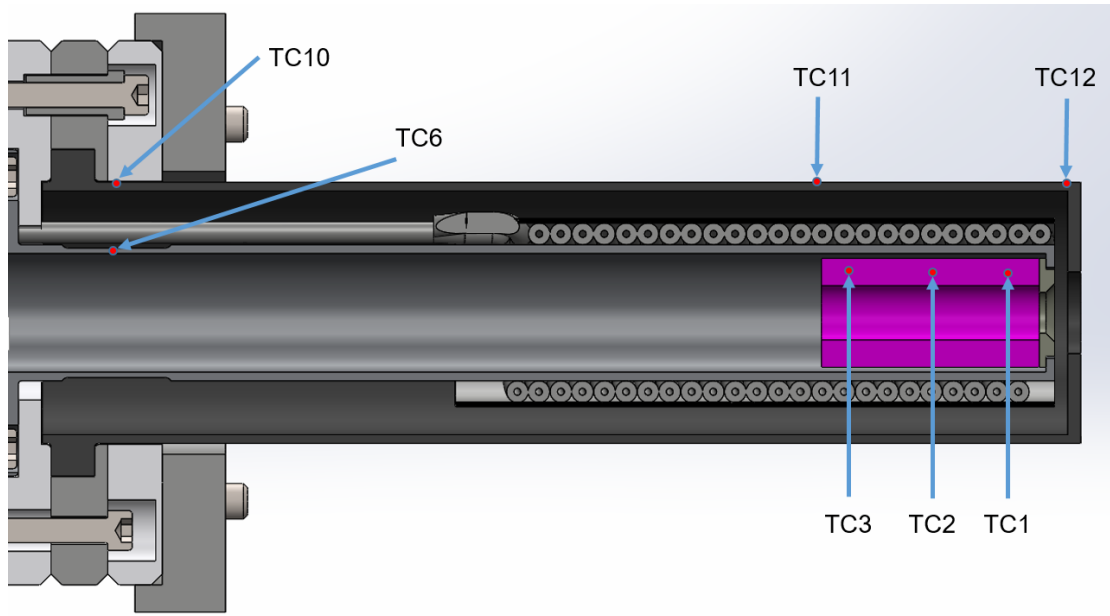


Figure 3.11: Location where the thermocouples were installed.

3.3.4 Hollow cathode plasma model (text by Dr. Yiingos Mikellides, coauthor in the paper.)

All plasma simulations presented herein have been performed with the 2D axisymmetric solver of the partially ionized gas in hollow cathode discharges called OrCa2D.

The physics models, conservation equations and numerical methods in OrCa2D have been described in detail in previous articles [23, 5, 24, 25] and will only be described briefly here. The code solves the conservation laws for three species in the partially-ionized gas: electrons, xenon ions and xenon neutrals. It is assumed that only singly-charged ions are present and that quasi-neutrality prevails except inside sheaths which are handled with appropriate boundary conditions. The Navier-Stokes equations are solved for the neutral gas only inside the cathode up to a “transition boundary” at which the method to obtain the solution changes to a collisionless approach that assumes neutrals follow straight-line trajectories [26]. The Euler equations for mass and momentum of ions are solved in the entire computational domain. A separate energy equation is solved for the ions, allowing

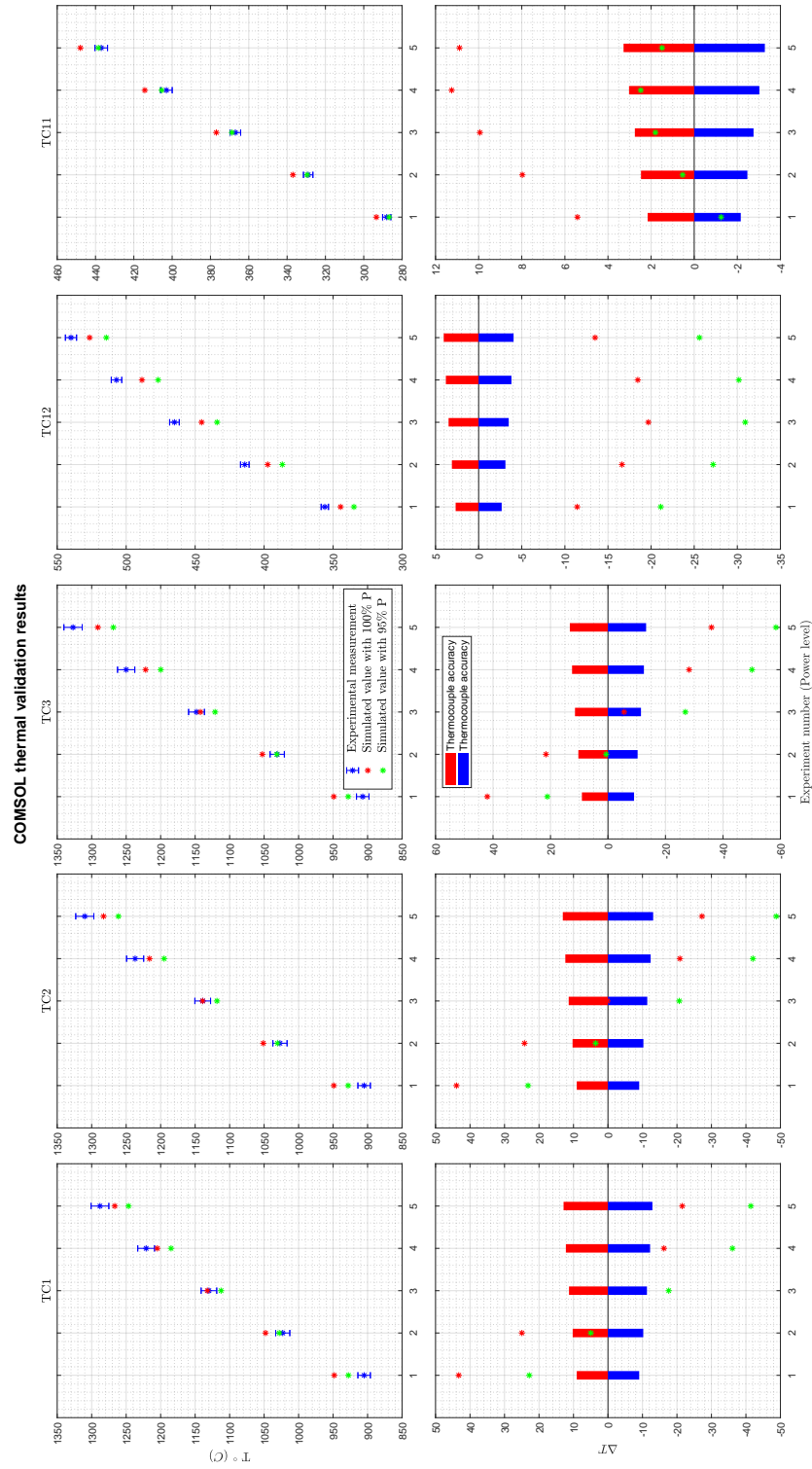


Figure 3.12: COMSOL thermal model validation results.

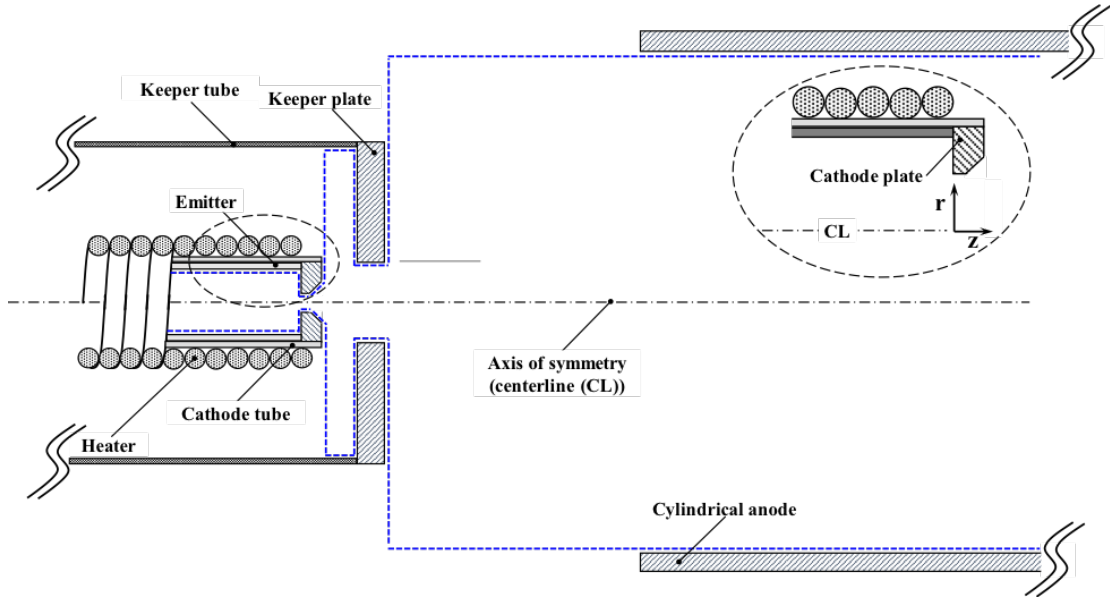


Figure 3.13: Schematic of the computational domain (blue dashed outline) used in the OrCa2D simulations, in a region near the cathode electrodes and plume (not to-scale).

for distinct temperatures for the two heavy species. Ionization, charge exchange and electron-ion collisions are accounted for in the equations and modeled either as source or drag terms. The solution for the electrons is obtained from a combination of Ohm's law, energy, and current conservation equations. An idealized model for the anomalous enhancement in the resistivity, which is now known to occur in the cathode plume [27, 28] due to the excitation of ion acoustic turbulence (IAT) there, is included in Ohm's law. The model is based on the formulations of Sagdeev and Galeev (S&G) [29] and is described in more detail in a paper by Mikellides, et al. [30].

The emitted electron current density from the insert is specified according to the Richardson-Dushman equation for thermionic emission [31]. The emitter temperature is implemented as a boundary condition in OrCa2D using a 4th-order (or lower) polynomial that provides the temperature as a function of axial position along the emitter. The field-enhanced emission due to the Schottky effect is included, and its implementation in OrCa2D is described in [32]. The work

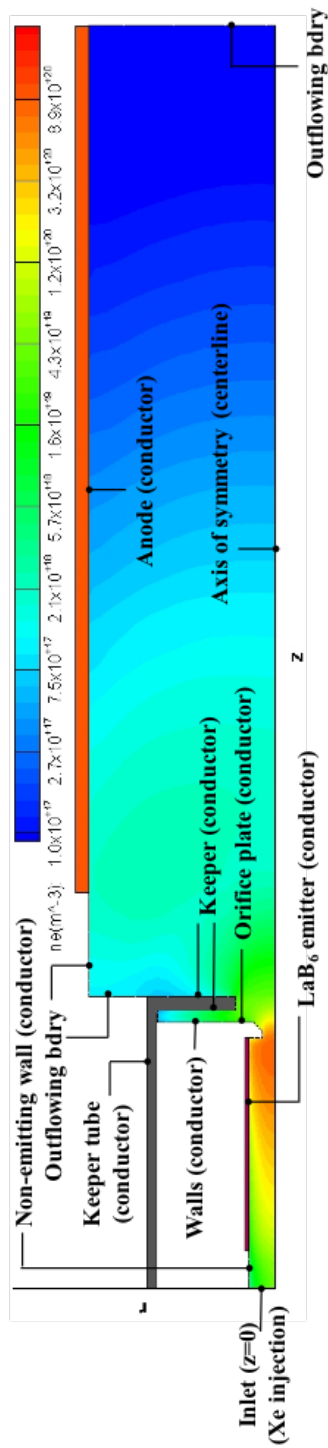


Figure 3.14: OrCa2D numerical simulation (half) domain showing naming conventions for all relevant boundaries of the LaB₆ cathode. (Also shown is the simulation result for the electron number density, n_e (the details of which are described later in this article).

function must be provided and its value depends on the specific case studied. It is important to emphasize that net emission is determined not only by the emission current density but also by the current density of electrons and ions that are adsorbed by the emitter wall. This is also accounted for in OrCa2D as described in [23, 5]. For boundaries that are electrically conducting, electron and ion collection is accounted for in both limits of ion-attracting and an ion-repelling sheaths. This boundary condition was described in detail in [33]. At the anode, current is collected as specified by the discharge current. It is also assumed that ions become neutralized after they strike it and return back to the computational region as neutrals with a thermal speed that is based on the specified temperature of the anode.

In the experiments that provided the conditions and measurements for the cathode investigated here, a cylindrical anode was used [6]. The OrCa2D computational domain in the vicinity of the cathode plate and near plume is outlined in Fig. 3.13. The full domain from a representative simulation of the cathode is shown in Fig. 3.14. The two figures also provide naming conventions for the various cathode components and boundary conditions that are relevant to this study. The inlet boundary is defined to be at $z = 0$ in the domain. The keeper was set to collect no net current (i.e. it was floating), which was accounted for in the simulations through appropriate boundary conditions. A zero-current condition also was specified at the out-flowing boundaries (Fig. 3.14). A magnetic field was not applied in the experiments or the simulations.

The highest Xe^+ number density expected in the cathode is on the order of $n_{i_max} = 10^{21} \text{ m}^{-3}$. Using that estimate for the plasma density, the photon mean free path based on the Planck opacity or the Rosseland opacity is much larger than 10 cm and 2.5 m respectively [34, 35]. Thus, the plasma is considered transparent and it does not interact with the thermal radiation mechanisms described above.

At every global iteration step, a new temperature profile is input to the plasma solver. OrCa2D was configured to find the plasma solution that provides the keeper voltage that matches the experimentally measured value of V_K . Then, the new heat fluxes associated with the converged plasma solution are input into

the thermal model in order to generate an updated temperature profile for the insert ($T_{\text{insert}}(z)$). This is one of the many approaches that can be used to update the plasma solution at every iteration. This approach provided the most stable convergence in the global sense because the plasma solution is always close to the one that matches the experimental value of V_K , and only the heat fluxes are being influenced by the small changes in the plasma distribution and the updated value of the work function.

During the simulation, the evolution of the plasma solution is monitored by several numerical probes positioned throughout the computational domain. A convergence criterion has been implemented in OrCa2D that is based on the time-averaged computed variables. The algorithm computes the percent change in the main plasma variables within a specified time increment, from all numerical probes. The simulation is terminated when the maximum percent change is less than 10^{-6} . The MATLAB[®] framework was built to be able to manipulate this convergence criterion as needed. The current configuration requires the plasma solver to produce more accurate results as the global simulation gets closer to the self-consistent solution. This strategy optimizes global convergence computational time without affecting the fidelity of the final solution.

Initial plasma solution for the coupled plasma-thermal simulations

To start the coupled plasma-thermal simulations an initial solution of the plasma must be provided. This is obtained with OrCa2D as follows. The mass flow rate and discharge current are required as inputs to the simulation. They are therefore specified directly in the code based on the conditions under which the experiment was conducted, namely 13 sccm and 25 A. To achieve the specified discharge current, an iteration is performed on a single coefficient that determines the level of resistivity enhancement due to the IAT in the cathode plume, as described in more detail in Mikellides, et al. [36]. The discharge voltage is set in the simulations at 25 V to match the experiments. The temperature along the emitter $T_{\text{insert}}(T)$ is specified using a 2nd-degree polynomial fit to measurements discussed in Chap. 2 using three type C thermocouples, see Fig. 2.9. The simulation iterates on the

value of the work function to obtain the measured keeper voltage of 4.2 V.

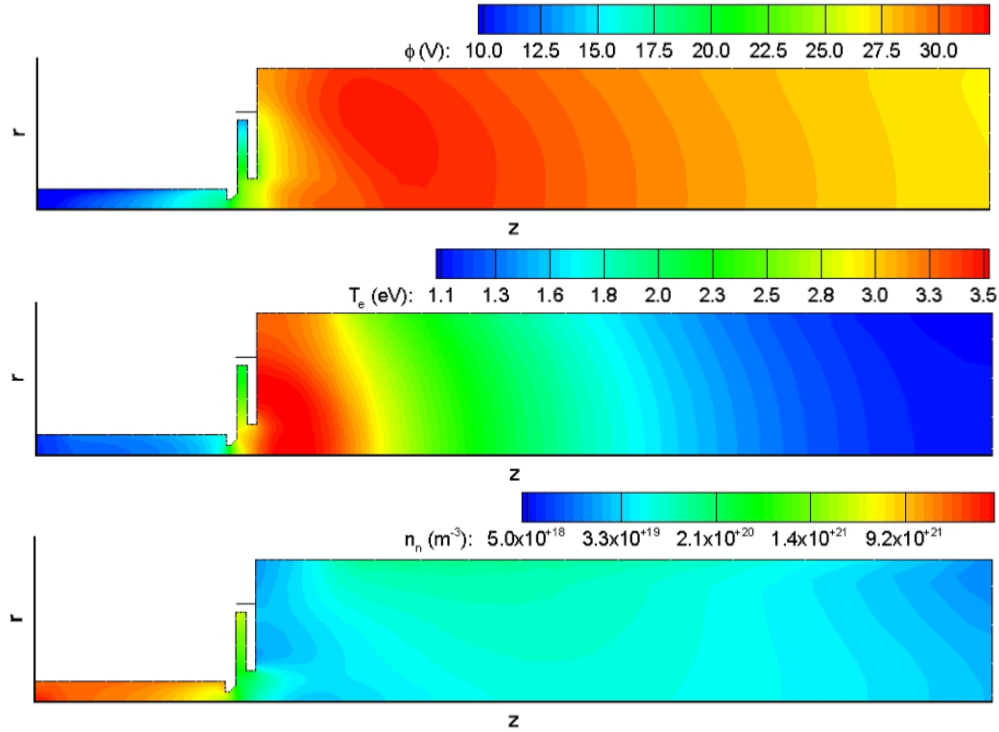


Figure 3.15: Steady-state solution for the plasma potential (ϕ), electron temperature (T_e) and neutral gas density (n_n) from the OrCa2D simulations with the initial emitter temperature profile shown in Fig. 3.21. The solution was used to calculate the initial heat fluxes for the coupled plasma-thermal simulations.

3.3.5 Plasma model validation (text by Dr. Yiingos Mikellides, coauthor in the paper.)

Unlike general-purpose computational tools, such as commercial computational fluid dynamics (CFD) and scientific magneto hydrodynamics (MHD) codes, OrCa2D was developed to simulate a very specific problem, namely the hollow cathode discharge. A main reason for developing a new code to do this was that the physics that drive the discharge are uniquely diverse in these devices and span a wide range of spatial and temporal scales. Hence, it became evident very early that attempts to model the problem using general-purpose tools, or some modified version of them,

would be futile and that a tailored mathematical and numerical approach had to be developed from scratch. A consequence of this is that the ability to validate the strongly-coupled governing physics models, or even subsets of these models, using existing analytical solutions were very limited. Thus, OrCa2D's validation has been pursued largely by direct comparisons with laboratory measurements, which themselves carry uncertainties of varying degrees. Because neither the simulations nor the experiments performed to validate them are straightforward, the comparisons between the numerical results and the laboratory measurements have varied. A typical example is provided in Figs. 3.16, 3.17 and 3.18, which shows comparisons between OrCa2D and experimental results for two very different hollow cathodes [32]. In the small cathode (bottom), called NSTAR DHC, the agreement between electron number densities was well within the uncertainty of the measurement whereas in the larger cathode the simulation under-predicted the measurement in the interior by about a factor of 1.7 (see Fig. 3.17). Despite this discrepancy, the agreement with the plasma potential and electron temperature in this same cathode was found to be less than 10 % and 25 %, respectively (see Fig. 3.18).

Development of the code began in 2004 and since then it has been used to simulate numerous hollow cathodes, operating under a wide range of conditions [23, 5, 37, 24, 33, 25, 38]. In most cases, each investigation focused on a given geometry at a fixed or a range of operating conditions to elucidate specific physics such as electrode erosion [23, 24, 33], emission and related sheath physics [37, 5], power deposition and thermal response of the cathode[2, 39, 37], effects of neutral gas viscosity [25], BaO material transport[40, 41], operation at high discharge currents [32], and electron transport due to ion-acoustic turbulence [42]. In many cases, especially early in the development of OrCa2D, comparisons between simulations and laboratory measurements helped advance the physics models, thereby improving the fidelity of the code. Occasionally, even with the more accurate models, larger discrepancies would be obtained in one cathode compared to another (such as those shown in Fig. 3.16). Since the code solves the same governing equations for every cathode, part of these discrepancy variations were due to uncertainties that are difficult to quantify, for example in the inputs to

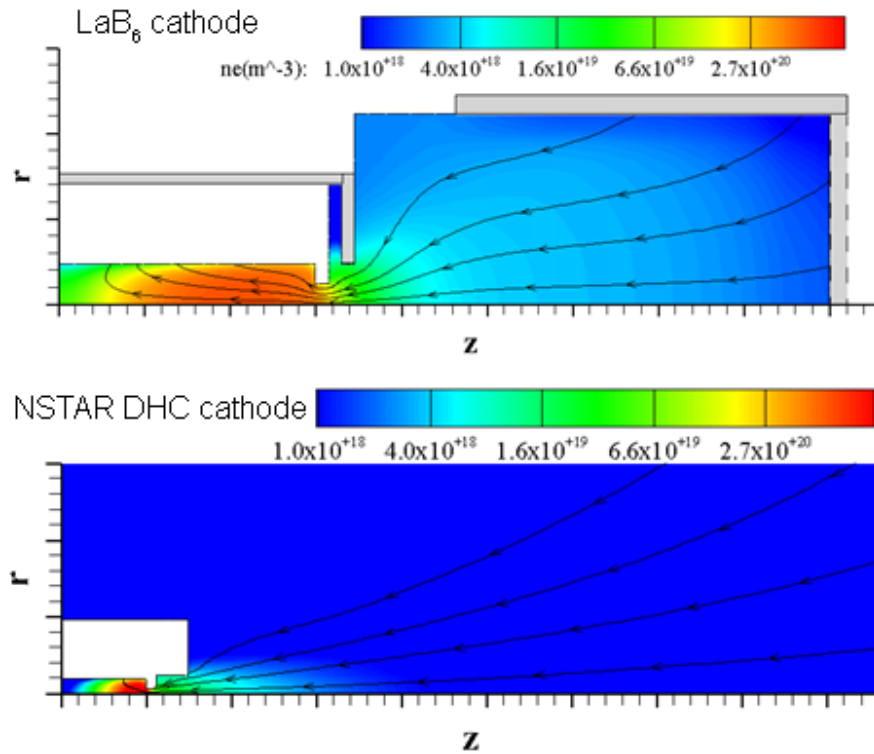


Figure 3.16: Comparison of a LaB₆ hollow cathode operating at 100 A and 12 sccm with a BaO cathode (called NSTAR DHC) operating at 13.3 A and 3.7 sccm. OrCa2D simulation results for the electron number density showing the significantly different geometries of the two cathodes. Also shown are representative electron current density streamlines. [2]

the simulations and/or in the laboratory measurements, and/or due to subtle differences between simulation and experimental setup. For example, in Fig. 3.16, the emitter temperature (a required boundary condition for OrCa2D), was not known as well in the 100-A cathode as it was in the 13.3-A cathode, which the authors identified as a possible source of the discrepancy in the density.

Based on the wide range of cathode geometries and operating conditions that OrCa2D has simulated, and the many comparisons with laboratory measurements, the developers of the code estimate that in the absence of errors associated with discrepancies in the experimental setup and/or uncertainties in the material properties (such as emission characteristics), the uncertainty of the solution in the

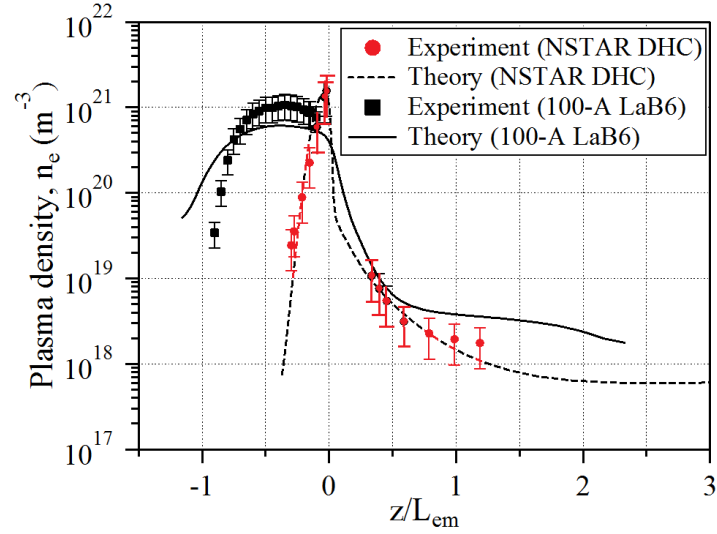


Figure 3.17: Comparison of the electron number densities along the centerline of the two cathodes between theory and experiment. [2]

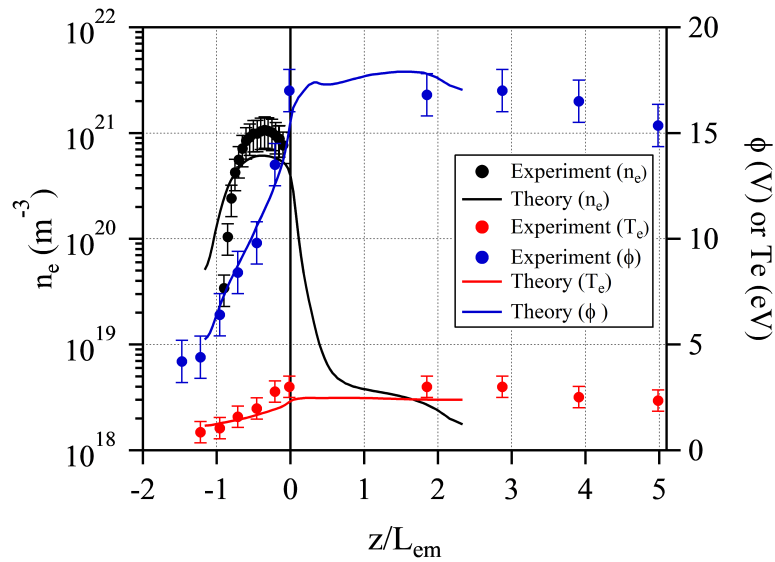


Figure 3.18: Comparison of the plasma potential and electron temperature along the centerline of the 100-A LaB6 cathode. The density comparison is repeated for reference. [2]

cathode interior is less than 25% for the plasma potential and electron temperature and less than 50% for the plasma density.

3.3.6 Heat flux model

The inner region plasma consists of three fluids – neutrals, electrons and ions. Depending on the operating point of the cathode, different fluxes of those species reach the internal cathode surfaces exposed to the plasma. These fluxes heat the cathode, thus maintaining operating temperatures. The heat fluxes are computed following Eqs. 3.4, 3.5, and 3.6

$$\dot{q}_{\text{ther}} = -j_{\text{ther}} \phi \quad (3.4)$$

$$\dot{q}_e = -j_{e\text{-return}} (2T_e + \phi) \quad (3.5)$$

$$\dot{q}_i = j_{i\text{-return}} (\alpha_{\text{EAC}}^0 f(\beta) (\phi_{\text{sheath}} + T_e/2) + \alpha_{\text{ISC}} E_{\text{NC}}) \quad (3.6)$$

where \dot{q}_{ther} , is a cooling heat flux term due to electrons going over the work function barrier of the insert. \dot{q}_e and \dot{q}_i are heating terms associated with the return current of electrons and ions. j_{ther} is the thermionically emitted electron current density defined in Eq. 3.1. $j_{e\text{-return}}$ is the return current density of electrons. $j_{i\text{-return}}$ is the return current density of ions. ϕ is the work function of the insert. T_e is the electron temperature at the sheath edge. ϕ_{sheath} is the potential of the sheath. α_{ISC} is the ion survival probability. α_{EAC}^0 is the energy accommodation coefficient for normal-to-the-surface angle of incidence β . $f(\beta)$ is the function that models the dependence of the energy accommodation coefficient with ion-surface incidence angle. E_{NC} is the energy associated with the neutralization event, with a maximum possible value equal to the ionization potential of the first excited state of the gas minus the work function of the surface.

In the cathode used in this study, the main thermal load consists of ions returning to the cathode, accelerated in the sheath and pre-sheath. The main cooling load comes from the thermionic emission of electrons into the plasma. The emitter and the orifice plate receive approximately the same net heat load. The

next relevant heat load is received by the keeper. The electron heating effect is insignificant given the low electron return current collected.

The total amount of energy that ions returning to the cathode bring with them consists of the energy picked up as the ions are accelerated through the potential of the sheath $j_{i\text{-return}} \phi_{\text{sheath}}$, their thermal energy $j_{i\text{-return}} T_e/2$ (due to the plasma potential drop in the pre-sheath), and the ionization potential (IP) of the specific gas used, in our case, xenon [43]. The exact amount of heat transferred to a surface when an ion collides with it depends on the following factors: ion survival probability, energy accommodation factor, and neutralization mechanism.

The ion survival probability α_{ISC} quantifies the probability that an ion will be neutralized when it interacts with a surface. In our case, the low energy of the noble gas ions returning to the surfaces of the cathode (< 50 eV) indicate that we can assume 0% probability of ion survival rate ($\alpha_{\text{ISC}} = 1$) [44].

The return current of electrons is estimated following classical sheath theory [43]. Returning electrons heat the material by the work function as they descend through the potential barrier of the surface. They also transfer their kinetic energy, computed as the flux weighted average kinetic energy [2].

3.3.6.1 Energy accommodation coefficient

The energy accommodation coefficient α_{EAC} depends on the inelastic behavior of the interaction between ions and the atomic structure of the surface, therefore, it is a function of the energy and incident angle of the ions with respect to the normal of the surface (β). α_{EAC} only affects the potential and thermal energy of the ions, where α_{EAC}^0 is the energy accommodation factor for normal ion incidence and $f(\beta)$ is the function that accounts for deviations with respect to the normal. In this work, we only use the canonical form of $f(\beta) = \cos(\beta)$ as the ions become merely perpendicular to the surface due to the strong action of the sheath, and therefore, the results are basically insensitive to the functional form of $f(\beta)$.

The energy accommodation coefficient (EAC) strongly depends on the mass ratio (μ) between gas ions and surface atoms. The EAC is different for ion-surface

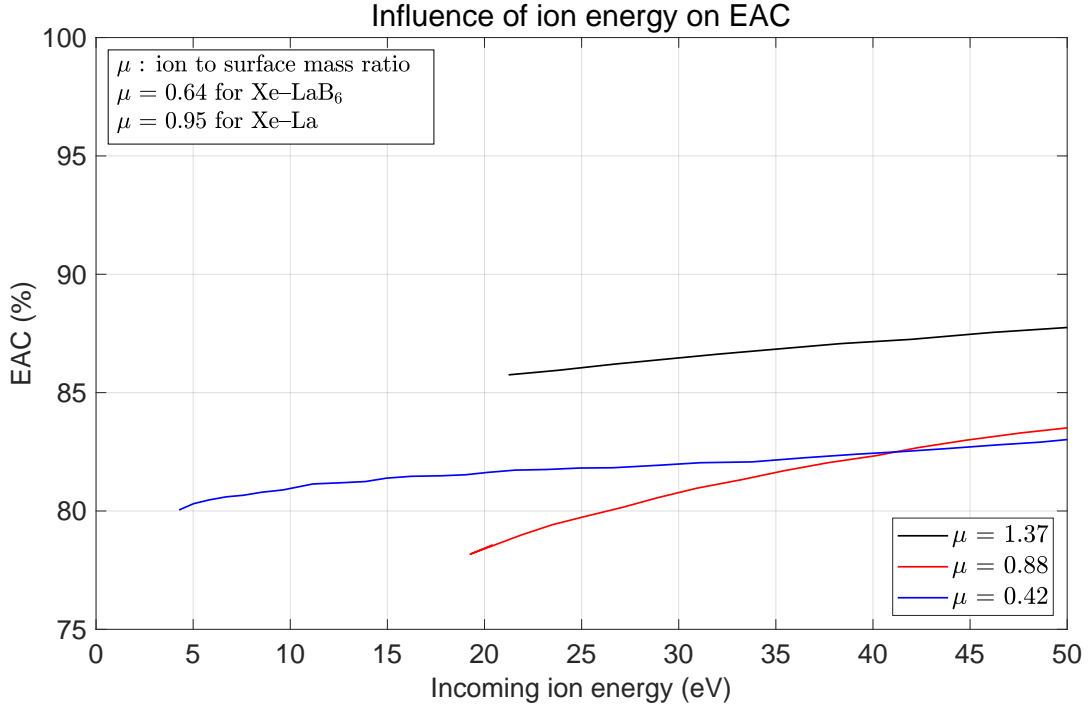


Figure 3.19: EAC as a function of ion-surface mass ratio and ion energy. Data from [45].

interaction and neutral-surface interaction. To our knowledge, there are no data available in the literature for the system $\text{Xe}^+ - \text{LaB}_6$ in the energy range of interest for this work. In order to bound the effect of the EAC in our case, we extrapolated the results of the only data available for the interaction between low energy ions and polycrystalline surfaces [45], see Fig. 3.19. In our case, Xe ions interact with LaB_6 crystals. Depending on the crystal, the interaction will occur with lanthanum atoms (when the crystal is purely terminated in La, like the crystal (001)) or a molecular form of LaB_6 , depending on how many boron atoms participate on the interaction. In the case $\text{Xe}^+ - \text{LaB}_6$, $\mu_{\text{Xe}^+ - \text{LaB}_6} = 0.64$ and in the case $\text{Xe}^+ - \text{La}$, $\mu_{\text{Xe}^+ - \text{La}} = 0.95$. According to Shuvalov's experimental data, the $\text{EAC}_{\text{Xe}^+ - \text{LaB}_6}$ for ion energies lower than 50 eV must be lower than 90% and higher than 75%.

3.3.6.2 Neutralization model

The energy associated with the neutralization event is accounted for in E_{NC} . There are two possible families of neutralization mechanisms based on how many steps it takes for the neutralization event to be completed: single or two step. The selection of mechanism depends on the surface internal electron density distribution where the ions collide, and on the energy level of ionized and first excited neutral states of the incoming ion.

One step neutralization model

Among the single step neutralization mechanisms only two are applicable to the case where low energy ions impact solid surfaces: resonant tunneling neutralization and Auger neutralization. The leading theory describes resonant neutralization as the dominant mechanism by which low energy ions neutralize upon interactions with conductive surfaces [46]. Auger neutralization can still exist in this case, with a much smaller probability. Only when the density of states (DOS) in the solid is not aligned with the energy levels in the ion, Auger neutralization takes a dominant role. This is the case when He^+ interact with metals. In our case, if the neutralization event between Xe^+ and LaB_6 occurs following a single step, it will most probably do it by resonant neutralization. In this case, incident xenon ions are neutralized as they come closer to the surface by tunneling an electron from the appropriate energy band of the solid into an energy hole of the ion, thus creating a ground state xenon neutral. In this case the energy given to the surface is the ionization potential of xenon minus the work function of the surface $E_{\text{NC}} = IP - WF$, where $IP = E(\text{Xe}^+) - E(\text{Xe}^0)$.

Two step neutralization model

The alternative neutralization model consists of resonant neutralization to the first excited state of xenon (Xe^*) followed by Auger de-excitation to the ground state of xenon (Xe) [47]. This mechanism is only possible if the work function of the material is low enough, thus allowing electrons from the appropriate energy level in the material to fill the respective energy hole in the ion, creating an excited neutral.

In the case of xenon, the difference between the ionized and the first excited state is $E(\text{Xe}^+) - E(\text{Xe}^*) = 3.81$ eV [48]. This means that only the emitter surface can be modelled with this two step neutralization model, as the other surfaces are pure metals and their work function is greater than 3.81 eV. The probability of creating excited neutrals is higher than creating ground state atoms because electrons have to tunnel through a lower potential barrier.

In the first step, the amount of heat exchanged between the ion and the surface is due to the transfer of one electron per ion neutralized, $E(\text{Xe}^+) - E(\text{Xe}^*) - WF$. During the second step, the excess of energy contained in the excited xenon neutral relaxes to the ground state xenon neutral by transferring that energy to the solid. The electrons in the solid will then be excited with this energy. Depending on the distribution of the energy in the solid, a different population of electrons will be excited and a portion of them will be emitted by means of Auger de-excitation. We model that yield with a parameter, γ_{Auger} . In summary, the total amount of energy deposited in the solid due to neutralization per ion strike is $E_{\text{NC}} = IP - WF - \gamma_{\text{Auger}}(E(\text{Xe}^*) - E(\text{Xe}^0))$.

As a side effect, electrons are emitted from the solid at a rate $j_e^{\text{A}} = \gamma_{\text{Auger}} j_{\text{i-return}}$. These electrons get accelerated away from the emitter by the emitter sheath. This component was accounted for in OrCa2D when computing the net charge exchange at the emitter surface. To date, there does not exist a theory or simulation capable of estimating the value of γ_{Auger} given specific ions and solids. However, it is possible to experimentally quantify it. To our knowledge, this has never been measured for the combination $\text{Xe}^+ - \text{LaB}_6$. Values below $\gamma_{\text{Auger}} = 3$ have been measured for several noble gases at different charge states interacting with tungsten [49].

3.3.7 Iterative solution (text by Dr. Yiangos Mikellides, coauthor in the paper.)

As noted earlier, the plasma solution in Fig. 3.15 is used to calculate the initial heat fluxes for the coupled plasma-thermal simulations. During the coupled simulations the approach to obtain the steady-state OrCa2D solution at each

intermediate global iteration remains essentially the same. The exception is that at each iteration a new polynomial fit to the emitter temperature is defined at the OrCa2D emitter boundary, based on the solution provided by the thermal model. With the newly defined temperature, OrCa2D then proceeds to obtain the new steady-state solution by performing the two aforementioned iterations in parallel, namely on the anomalous transport coefficient to attain the specified discharge current (25 A) and on the work function to attain the measured keeper voltage (4.2 V).

Initializing the coupled plasma-thermal model with the aforementioned plasma solution produces the evolution of temperature $T_{\text{insert}}(z)_i$ and $T'_{\text{insert}}(z)_i$ at every global iteration step i , as shown in Fig. 3.20.

3.4 Results

We employed the novel scheme described above to study the self-consistent solution of a LaB₆ cathode running at $J_D = 25$ A and $\dot{m}_{\text{Xe}} = 13$ sccm with the experimentally measured values of $V_K = 4.2$ V and $V_D = 25$ V for the keeper and discharge voltage. In the simulations presented here, the plasma convergence criterion was set to 0.002%.

3.4.1 Baseline thermal model, $\alpha_{\text{EAC}}^0 = 1$, one step neutralization

The self-consistent solution ($T_{\text{insert}}(z)_i = T'_{\text{insert}}(z)_i$) is shown in blue in Fig. 3.21 for the *baseline* thermal model. The modelling approach for the heat fluxes assumes $\alpha_{\text{EAC}}^0 = 1$ and $f(\beta) = 1$. The neutralization mechanism is the single step resonant neutralization to Xe⁰ and the work function profile along the insert is constant. In this case the work function converged to 2.55 eV and the net return current was 19.76% of the discharge current.

Notably, the converged insert temperature profile does not match the thermocouple measurements, with the solution predicting higher temperature (~ 150 °C) than that measured with thermocouples. The thermocouple measurement approach was thoroughly analyzed in our previous work [6], and we concluded that the

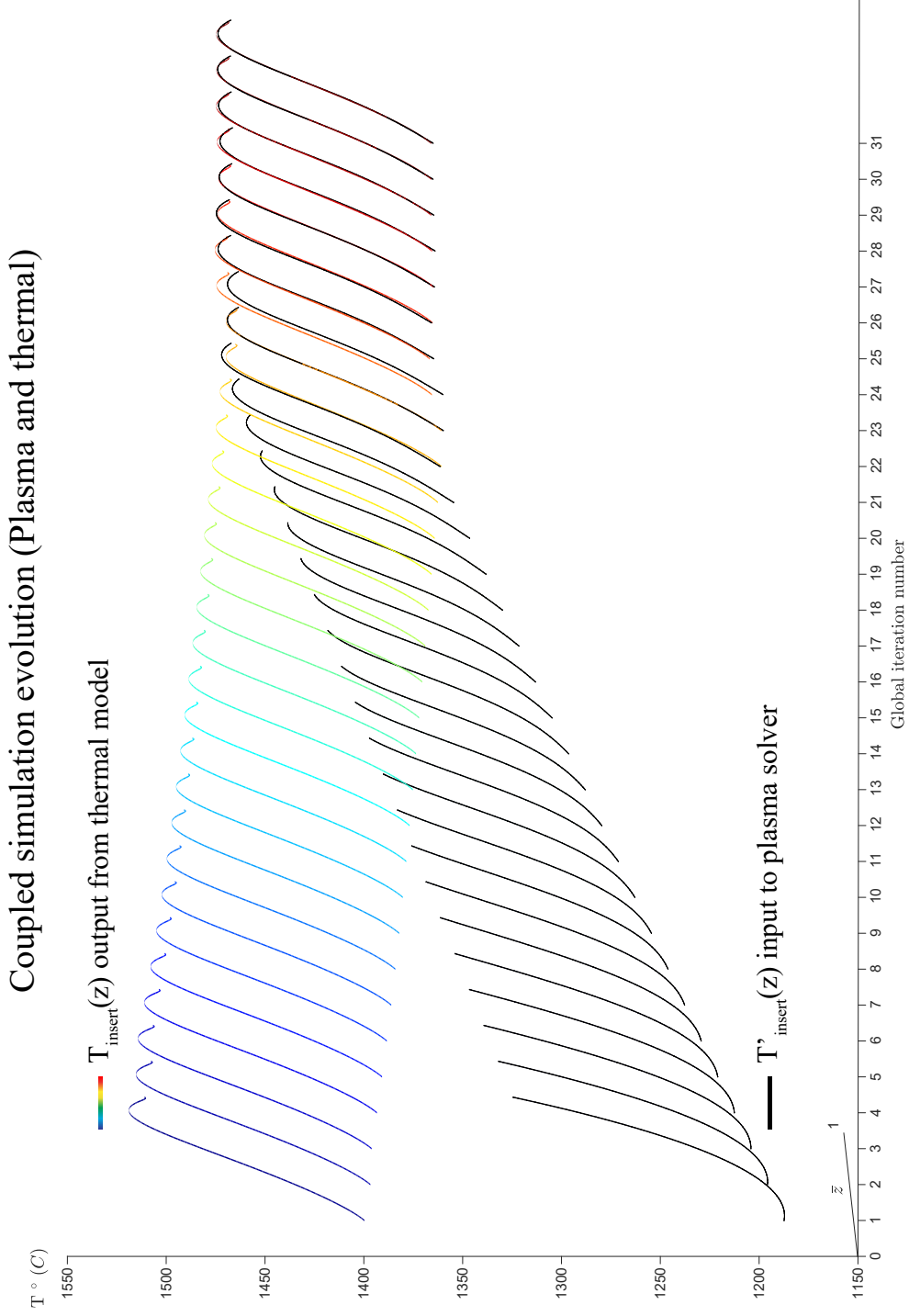


Figure 3.20: Evolution of the temperature input to OrCa2D (black curves) and output from COMSOL thermal model based on heat fluxes from the last iteration of OrCa2D (colored curves).

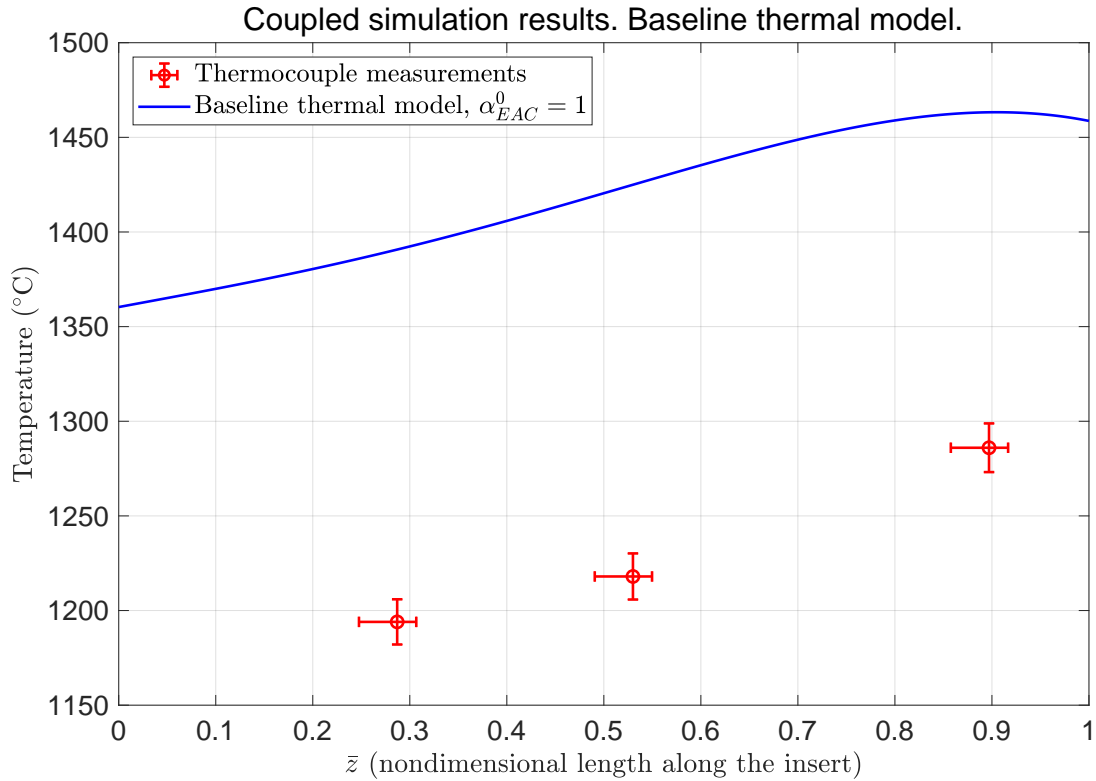


Figure 3.21: Converged temperature results for the *baseline* thermal model. Experimental values shown for comparison.

discrepancy observed in the coupled converged solution cannot be explained by an inaccuracy of the temperature measurements. Therefore, we conclude that this discrepancy must be the result of modelling inaccuracies in either the plasma, heat flux or thermal models.

3.4.2 Sensitivity to errors in plasma model results

We did not perform a sensitivity analysis for the plasma model as such analysis is outside the scope of this work. However, the heat fluxes are primarily dictated by the return and thermionic currents which are coupled with the plasma solution. It is of interest for future work to thoroughly study the dependence of the heat fluxes on the assumptions and sensitivities of the different variables involved in the definition of the plasma solution.

3.4.3 Sensitivity to thermal model assumptions

To understand the sensitivity of the thermal model to the different parameters that define it, we studied the impact of parameter variations from the *baseline* thermal model. The most sensitive parameter in the cathode thermal behavior is the value for the total hemispherical emissivity of tantalum (ϵ_{Ta}). ϵ_{Ta} is used to model the radiation properties of the cathode tube, the heater and the radiation shield. ϵ_{Ta} in the literature is obtained for pure polished material. We observed darkening of different Ta cathode components, indicating impurities, that may increase the actual value of the emissivity. The darkening was particularly prominent on the radiation shielding, therefore, we used a value of $\epsilon_{\text{Ta}} + 0.2$ for this component in order to obtain the agreement shown in Fig. 3.12. This value was also used in the *baseline* simulation shown in Fig. 3.21.

We created a new thermal model to understand how the *baseline* thermal model validation is impacted by the increase of the emissivity that defines the radiation properties for some of its components. This new thermal model underestimates the global thermal losses of the cathode, and therefore, for any given power input, the temperature distribution of the inner region (insert region) is colder than the experimental values, see Fig. 3.22. The only difference between this thermal model and the *baseline* is that we have added 0.4 to the ϵ_{Ta} from literature in the material properties utilized to model the radiation shield, as opposed to 0.2 used in the *baseline*.

In Fig. 3.22 we have simplified the validation results by removing the absolute values of the experiments and simulations that we showed in Fig. 3.12. As TC1, TC2 and TC3 give very similar results due to their physical proximity, we only show results for TC2. We have also removed the two simulation series 100% P and 95% P , and only show the mean temperature simulated by both. Results for this thermal model show that TC2 is cooler than the experimental results by a minimum of ~ 30 °C and a maximum of ~ 110 °C. In addition, the new thermal model estimates ~ 70 °C cooler temperatures for all power levels than those for the *baseline*.

In order to estimate the sensitivity of the coupled system to inaccuracies in the

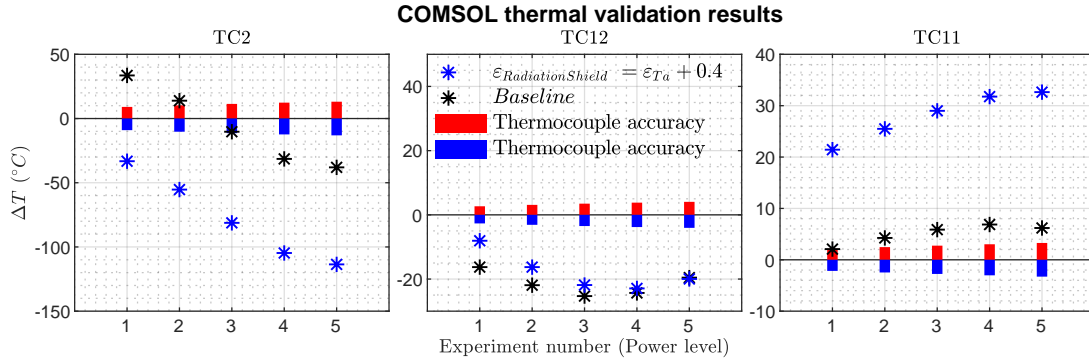


Figure 3.22: COMSOL thermal model validation results. Comparison between thermal model *baseline* and modified version with 0.4 addition to the emissivity of the radiation shield.

thermal model, we varied two parameters and ran the global simulation until the converged solutions of the system were found. These included ϵ_{Ta} (20% increase with respect to the literature values) for every Ta component, and ϵ_{Ta} used in the definition of the radiation shield (0.2 increase above the value used in the *baseline*). Results are shown in Fig. 3.23.

When we increase the value of the emissivity for modelling the radiation shield by 0.4 above the literature values, we are effectively overestimating the losses in the cathode as shown in Fig. 3.22 by the cooler response of the insert. However, that does not affect the response of the coupled solution significantly ($\sim 6^\circ\text{C}$), see Fig. 3.23. This occurs because in the coupled system, the overestimation of the thermal losses creates a temperature solution that results in lower thermionic emission. In this case the plasma solution cannot converge given that the total discharge current of 25 A cannot be satisfied. Therefore, the new plasma solution (self-consistent with this perturbed thermal model) is different than the one for the *baseline* thermal model.

A more significant overestimation of the losses was performed by using 120% of the literature values for the Ta emissivity for every Ta component in the cathode. The response of the converged solution using this modified thermal model was still not significantly cooler ($\sim 24^\circ\text{C}$). Therefore, the discrepancy between the converged global simulation results and the experimental values cannot be explained by any

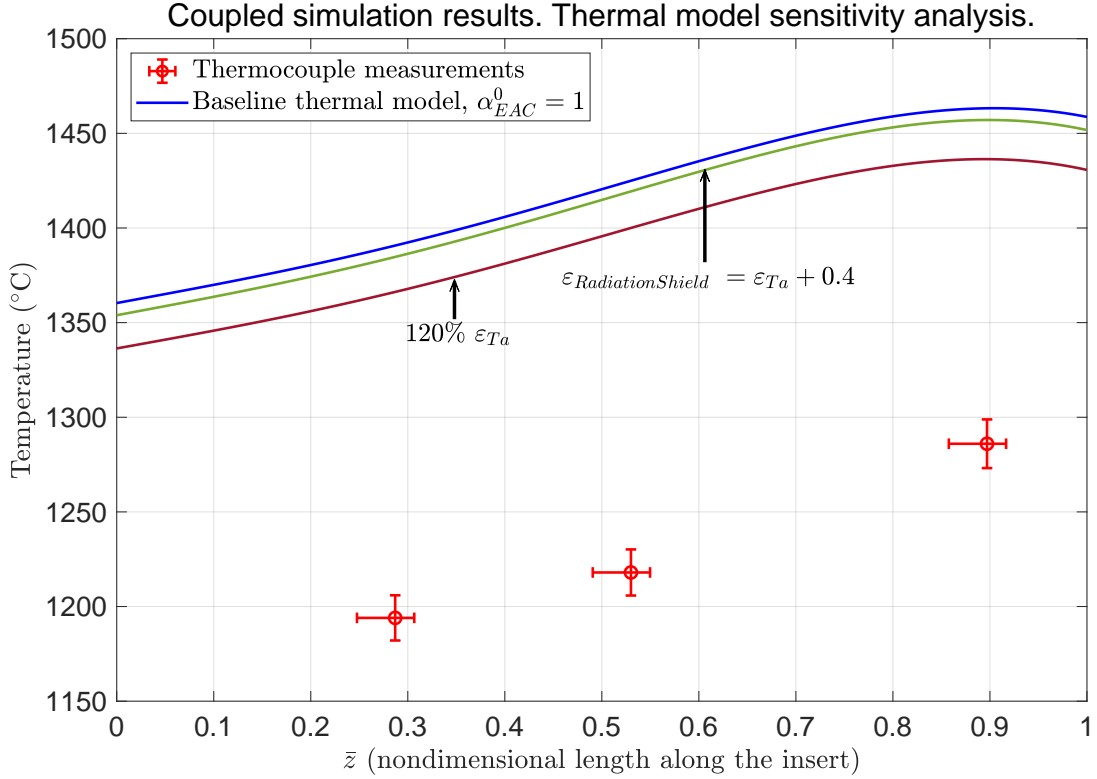


Figure 3.23: Converged temperature results for the *baseline* thermal model. Thermal model sensitivity analysis. Experimental values shown for comparison.

reasonable modification of the cathode thermal characteristics that result in an increase of the thermal model heat losses.

3.4.4 Sensitivity to plasma model parameters

The discrepancy between the predicted and observed temperature values could also be related to inaccuracies in the plasma solver results due to sensitivities in the input parameters defining the cathode operating point. The plasma solution depends on four experimentally measured variables and the modelling techniques. The four empirical variables – \dot{m}_{Xe} , J_D , V_D , and V_K – were measured with accuracies that do not affect the final solution significantly. However, the solution of the coupled system strongly depends on the value of V_K . V_K is ultimately used to find the work function at every global iteration step. We studied the sensitivity to V_K

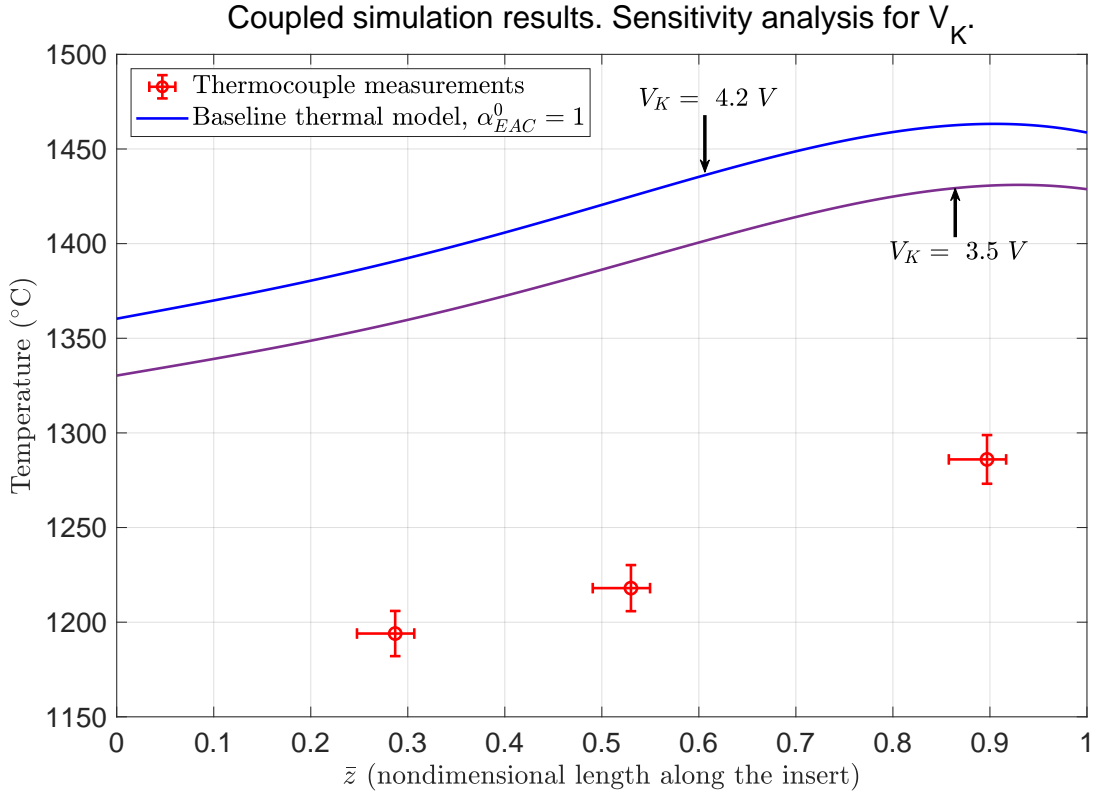


Figure 3.24: Converged temperature results for the *baseline* thermal model. Sensitivity analysis for V_K . Experimental values shown for comparison.

by reducing it to 3.5 V (0.7 V less than the actual measurement). Results are shown in Fig. 3.24.

The self-consistent insert temperature solution was reduced by ~ 30 °C in this case. This result suggests that inaccuracies in V_K modelling are not a likely explanation of the observed difference between experimental and modelling results.

3.4.5 Sensitivity to energy accommodation coefficient

The results also showed that the solution is indeed insensitive to $f(\beta)$ and if $\alpha_{EAC}^0 = 0.75$ at every surface of the cathode, the converged solution does not agree with the experimental values as shown in Fig. 3.25. The temperature distribution at convergence is in this case (~ 74 °C) cooler than the one obtained for the *baseline*

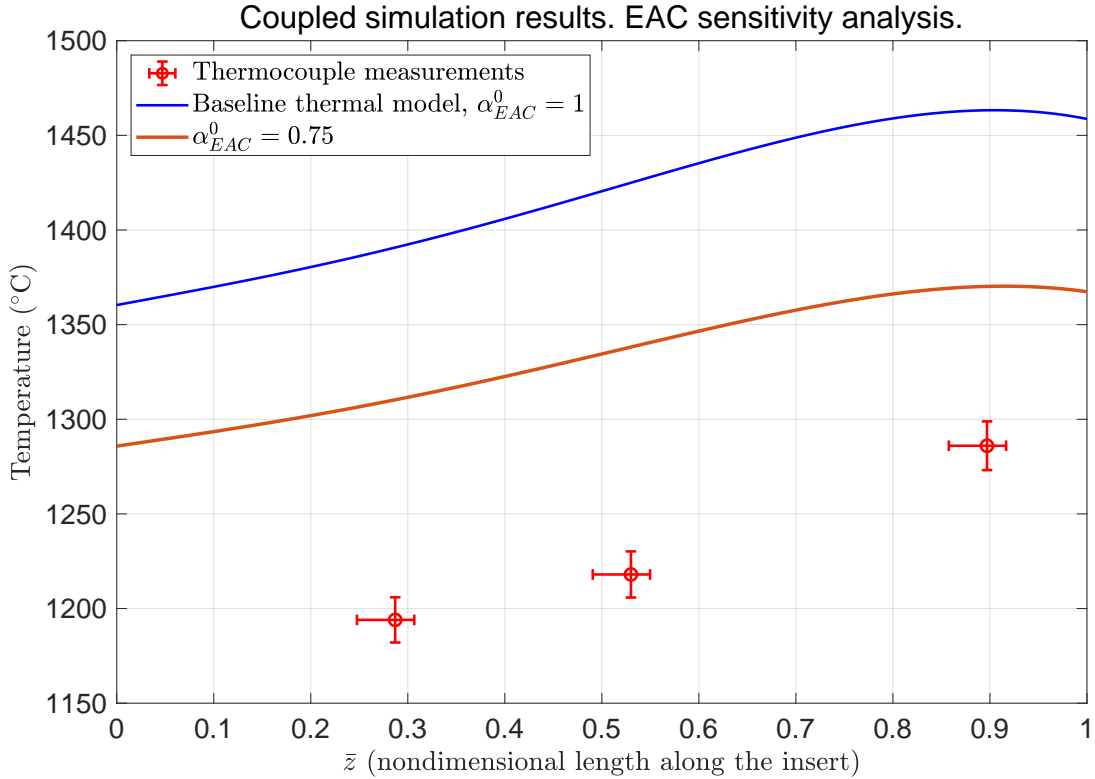


Figure 3.25: Converged temperature results for the *baseline* thermal model. Sensitivity analysis for EAC. Experimental values shown for comparison.

thermal model.

3.4.6 Sensitivity to work function distribution

In this work we also studied the dependence of the self-consistent solution on work function distributions along the emitter ($\phi(z)$). This study was motivated by the observation of discoloration along the emitter, suggesting chemistry evolution due to plasma interaction which could result in such axial variations in the work function. The impact on the magnitude of the work function or its spatial dependence is difficult to capture experimentally, as we cannot measure the work function or the chemical state of the surface while the cathode is running. However, to get an initial estimate of the sensitivity of the self-consistent solution to work function distributions, we decided to study the effect of linear and parabolic work

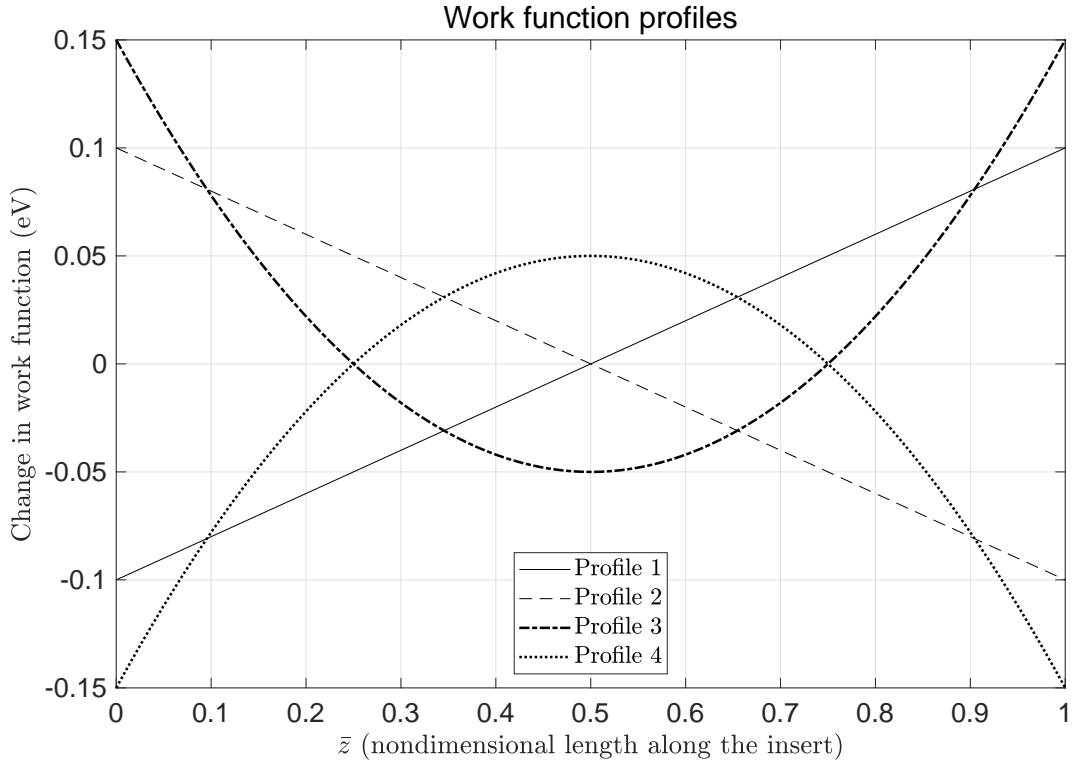


Figure 3.26: Work function profiles studied in this work.

function profiles whose mean magnitude is adjusted according to the self-consistent model needs. The amplitude of those profiles is 0.2 eV, value chosen arbitrarily to get an initial estimation of the sensitivity of the solution to a plausible real scenario, see Fig. 3.26. We use $\alpha_{\text{EAC}}^0 = 0.75$ for all the work function profiles studied.

The self-consistent solutions show that the temperature distribution is not greatly affected by the work function profiles utilized in this study. The net effect on the insert temperature for Profile 1 in Fig. 3.26 is a shifted temperature distribution ~ 30 °C cooler than the solution with constant work function profile. Similarly for Profile 3, it is ~ 25 °C cooler. For profiles 2 and 4, the shift is towards higher temperatures, by ~ 20 °C.

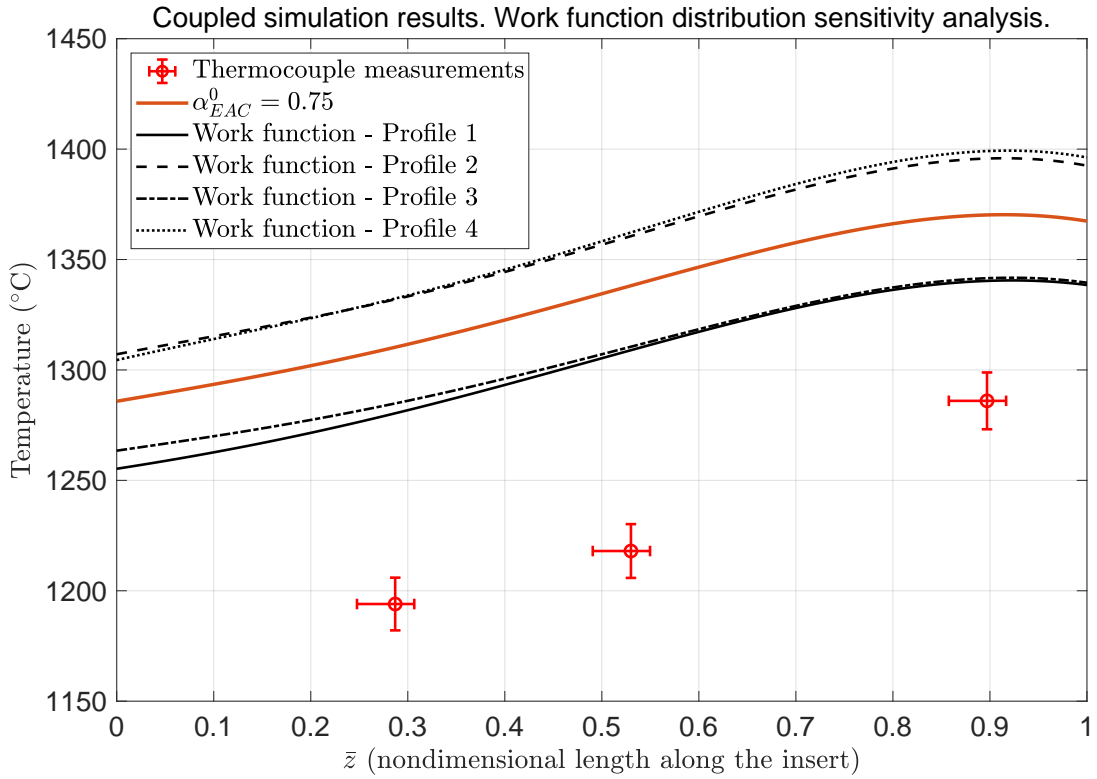


Figure 3.27: Converged temperature results for the *baseline* thermal model. Sensitivity analysis for work function distributions. Experimental values shown for comparison.

3.4.7 Sensitivity to neutralization model

A much better agreement was found when the two step neutralization model was employed. In this case, $\gamma_{\text{Auger}} = 0.85$ ($\alpha_{\text{EAC}}^0 = 1$) was sufficient to find a reasonable agreement with the experimental results, with work function convergence at 2.27 eV. Similar agreement was found when $\gamma_{\text{Auger}} = 0.5$ and $\alpha_{\text{EAC}}^0 = 0.8$, in which case the work function is 2.25 eV.

3.5 Discussion

The converged solution is defined by the COMSOL thermal *baseline* model and the OrCa2D plasma solution necessary to match V_D and V_K at the operating point

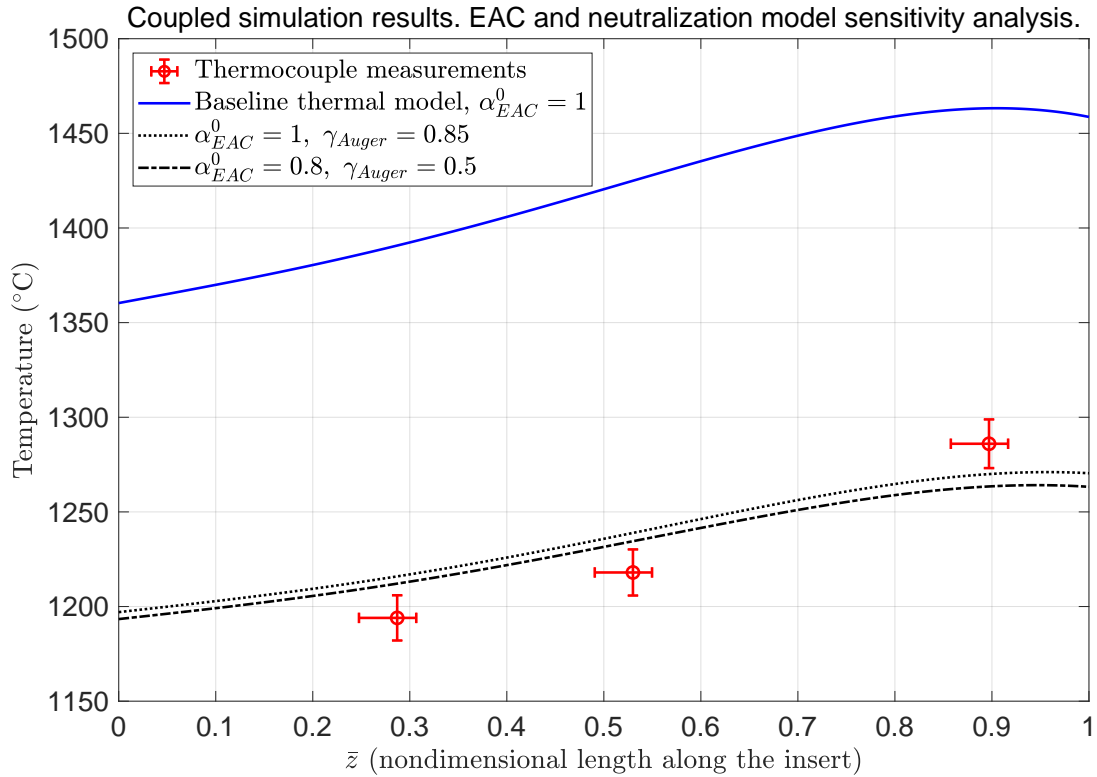


Figure 3.28: Converged temperature results for the *baseline* thermal model. Sensitivity analysis for EAC and neutralization model. Experimental values shown for comparison.

utilized in this test case. Coupling both models imposes an additional constraint in the solution, therefore, one less degree of freedom is available. Thus, ϕ and $T_{\text{insert}}(z)$ are the inherent results of this coupled system.

We have shown in Fig. 3.20 that the simulation approach is successful and convergence occurs.

In order to find agreement with experimental measurements we need to employ one or the other of two major assumptions. One assumption is that α_{EAC}^0 is smaller than 0.75 if resonant neutralization dominates the charge exchange process of ions that interact with solids for every surface at the cathode-plasma interface. However, we propose that this scenario is unlikely: accommodation coefficients are dominated by the mass ratio between the ions and the atoms of the surface.

According to the most extensive data set that we could find in the literature [45] extended to the Xe^+ - LaB_6 case, α_{EAC}^0 is not expected to be lower than 0.8.

An alternative assumption that leads to an agreement between simulation results and experimental measurements is that the ion-surface interaction is governed by the two step neutralization process described above, with either $\gamma_{\text{Auger}} = 0.85$ and $\alpha_{\text{EAC}}^0 = 1$ or $\gamma_{\text{Auger}} = 0.5$ and $\alpha_{\text{EAC}}^0 = 0.8$. In each case, the work function predicted by the simulation platform is 2.27 and 2.25 eV respectively. These values corroborate our previous finding that LaB_6 inserts exposed to plasma in hollow cathodes display reduced work function [6] with respect to the previously reported value of 2.67 eV [3] measured in the vacuum diode configuration for polycrystalline LaB_6 . The refined prediction of the work function produced with the model includes all the effects introduced in 3.2. The most significant of them, for the test case analysed here, is the $\sim 20\%$ ion return current that the interior cathode plasma direct towards the insert walls. The contribution of the Schottky effect can be observed in Fig. 3.29.

Two step neutralization is a well-established process in systems comprising low energy ions neutralizing with low work function surfaces. To our knowledge the mechanism of Xe ion neutralization with LaB_6 solids has not been specifically addressed by empirical studies. Experimental work to confirm our model that Xe ions neutralize with LaB_6 solids following a two step neutralization mechanism in similar conditions should be performed.

We studied the behavior of the self-consistent cathode simulation approach with respect to work function axial distribution $\phi(z)$. The work function profiles tested did not influence the solution to the extent necessary to find agreement with the experimental results. The work function distribution might be non-uniform in the cathode, but we learned that the self-consistent solution is not heavily influenced by the studied $\phi(z)$ profiles.

The *baseline* thermal model could be improved upon by experimentally testing individual components or small sub-groups of components of the cathode and comparing the results with corresponding thermal simulations. In that manner we can likely reduce the variability observed in Fig. 3.12 over the different power

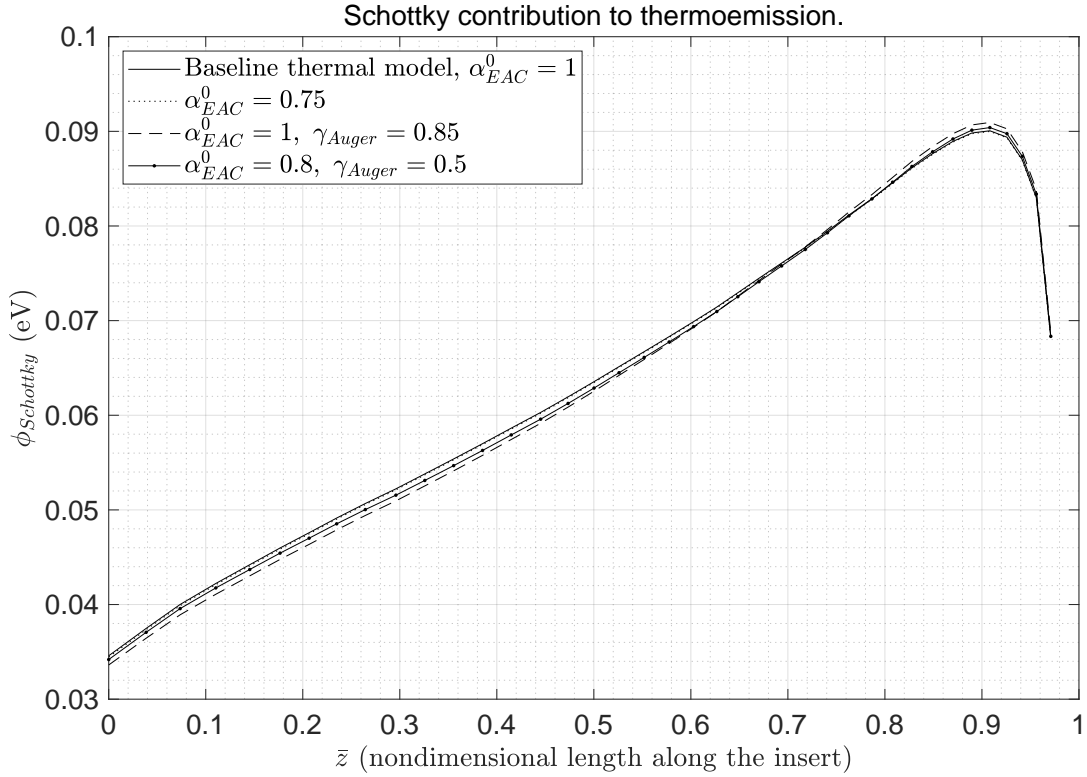


Figure 3.29: Contribution of the Schottky effect for the final self consistent solutions.

settings. Those studies would focus on trying to measure a more realistic emissivity for Ta in the actual components using a calibrated thermal camera. In addition, an improved modelling technique could be used to simulate the radiation shield and the contact between cathode tube and heater coils. However, given the results of the sensitivity analysis for the overestimation of the global heat losses of the cathode, it is not possible that refining the thermal characteristics of the cathode will explain the difference between temperature measurements and the self-consistent solution shown in Fig. 3.21.

Uncertainties in the plasma model should be identified and their impact in the self-consistent solution should be quantified. This is a very challenging goal given the number of variables involved and the inherently non-linear behavior of the plasma model. It is not clear at this point whether or not such study can be

accomplished within a reasonable amount of time given the computational cost of each simulation and the number of variables to be studied.

In conclusion, in order to predict the temperature distribution of the cathode in any configuration and operating condition we still need to identify which of the mechanisms studied here are in fact occurring in the cathode and to what extent they affect the cathode. Experimental work is necessary to obtain that knowledge.

BIBLIOGRAPHY

- [1] Gaétan Sary, Laurent Garrigues, and Jean-Pierre Boeuf. “Hollow cathode modeling: II. Physical analysis and parametric study”. In: *Plasma Sources Science and Technology* 26.5 (Mar. 2017), p. 055008. DOI: 10.1088/1361-6595/aa6210 (cit. on p. 61).
- [2] Ira Katz et al. “Thermal model of the hollow cathode using numerically simulated plasma fluxes”. In: 23.3 (2007). DOI: 10.2514/1.21103 (cit. on pp. 61, 85, 86, 87, 89).
- [3] J. M. Lafferty. “Boride Cathodes”. In: *Journal of Applied Physics* 22.3 (Mar. 1951), pp. 299–309. DOI: 10.1063/1.1699946 (cit. on pp. 61, 63, 104).
- [4] Walter H. Kohl. *Handbook of materials and techniques for vacuum devices*. AIP-Press, 1997, pp. XVI, 498. ISBN: 978-1563963872 (cit. on p. 62).
- [5] Ioannis G Mikellides et al. “Hollow cathode theory and experiment. II . A two-dimensional theoretical model of the emitter region”. In: *JOURNAL OF APPLIED PHYSICS* (2005), pp. 1–14. DOI: 10.1063/1.2135409 (cit. on pp. 62, 69, 78, 82, 85).
- [6] Pablo Guerrero et al. “Work function reduction in lanthanum hexaboride hollow cathodes operated in gas discharges”. In: *35th International Electric Propulsion Conference*. Atlanta, GA, USA, 2017, pp. 2017–399. URL: https://iepc2017.org/sites/default/files/speaker-papers/iepc-2017_399.pdfhttp://erps.spacegrant.org/IEPC_2017/IEPC_2017_399.pdf (cit. on pp. 63, 66, 82, 93, 104).
- [7] N. D. Milošević et al. “Thermal Properties of Tantalum Between 300 and 2300K”. In: *International Journal of Thermophysics* 20.4 (1999), pp. 1129–1136. DOI: 10.1023/A:1022659005050 (cit. on pp. 71, 72).
- [8] Takaho Tanaka. “The thermal and electrical conductivities of LaB 6 at high temperatures”. In: *Journal of Physics C: Solid State Physics* 7.9 (May 1974), pp. L177–L180. DOI: 10.1088/0022-3719/7/9/001 (cit. on p. 72).
- [9] Edmund K Storms. “The emissivity of LaB6 at 650 nm”. In: *Journal of applied physics* 4450 (1979). DOI: 10.1063/1.326438 (cit. on p. 72).
- [10] C. Y. Ho, R. W. Powell, and P. E. Liley. *Thermal Conductivity of the Elements: A comprehensive review*. 1974. DOI: 10.1063/1.3253100 (cit. on p. 72).

- [11] General Electric Company and Nela Park. “Radiating Characteristics of Tungsten and Tungsten Lamps”. In: *Journal of the Optical Society of America* 35.2 (1945), pp. 108–113. DOI: 10.1364/JOSA.35.000108 (cit. on p. 72).
- [12] A. G. Worthing and W.E. Forsythe. “Total emissivity powers and resistivities of tungsten at incandescence”. In: *Physical Review* 18 (1921), pp. 144–147 (cit. on p. 72).
- [13] W. E. Forsythe and E. M. Watson. “Resistance and Radiation of Tungsten as a Function of Temperature”. In: *Journal of the Optical Society of America* 24.4 (Apr. 1934), p. 114. DOI: 10.1364/JOSA.24.000114 (cit. on p. 72).
- [14] W. D. KINGERY et al. “Thermal Conductivity: X, Data for Several Pure Oxide Materials Corrected to Zero Porosity”. In: *Journal of the American Ceramic Society* 37.2 (Feb. 1954), pp. 107–110. DOI: 10.1111/j.1551-2916.1954.tb20109.x (cit. on p. 72).
- [15] S Weisenburger. “Heat transport measurements in polycrystalline graphites up to 2600C (Report on an international cooperative measuring programme)”. In: *High Temperatures - High Pressures* 5 (1973), pp. 475–480 (cit. on p. 72).
- [16] Bufa Zhang, John Redgrove, and Jamie Clark. “New apparatus for measurement of the spectral, angular, and total emissivity of solids”. In: *High Temperatures - High Pressures* 35-36.3 (2003), pp. 289–302. DOI: 10.1068/htjr124 (cit. on p. 72).
- [17] N/A. *Military Handbook - MIL-HDBK-5H: Metallic Materials and Elements for Aerospace Vehicle Structures*. U.S. Department of Defense, 1998, pp. 3–261. ISBN: 978-1-59124-543-8 (cit. on p. 72).
- [18] Chang-da Wen and Issam Mudawar. “Experimental Investigation of Emissivity of Aluminum Alloys and Temperature Determination Using Multispectral Radiation Thermometry (MRT) Algorithms”. In: *Journal of Materials Engineering and Performance* 11.5 (Oct. 2002), pp. 551–562. DOI: 10.1361/105994902770343818 (cit. on p. 72).
- [19] Michael F. Cohen and Donald P. Greenberg. “The hemi-cube”. In: *ACM SIGGRAPH Computer Graphics* 19.3 (July 1985), pp. 31–40. DOI: 10.1145/325165.325171 (cit. on p. 73).
- [20] Urs Meyer. “Hemi-Cube Ray-Tracing: A Method for Generating Soft Shadows”. In: *Eurographics 90* (1990), pp. 365–376 (cit. on p. 73).
- [21] A. F. Emery et al. “Validation of Radiation Computations using View factors and COMSOLs Hemicube Approaches”. In: *COMSOL Conference 2009 Boston* (2009) (cit. on p. 73).

- [22] P. D. Desai et al. “Electrical Resistivity of Selected Elements”. In: *Journal of Physical and Chemical Reference Data* 13.4 (Oct. 1984), pp. 1069–1096. DOI: 10.1063/1.555723 (cit. on pp. 75, 76).
- [23] Ioannis G Mikellides and Ira Katz. “Wear Mechanisms in Electron Sources for Ion Propulsion , 1 : Neutralizer Hollow Cathode”. In: *Journal of Propulsion and Power* 24.4 (2008). DOI: 10.2514/1.33461 (cit. on pp. 78, 82, 85).
- [24] Ioannis G Mikellides et al. “Wear Mechanisms in Electron Sources for Ion Propulsion , II: Discharge Hollow Cathode”. In: *Journal of Propulsion and Power* 24.4 (2008). DOI: 10.2514/1.33462 (cit. on pp. 78, 85).
- [25] Ioannis G Mikellides. “Effects of viscosity in a partially ionized channel flow with thermionic emission”. In: *Physics of Plasmas* (2009), pp. 1–10. DOI: 10.1063/1.3056397 (cit. on pp. 78, 85).
- [26] Ira Katz and Ioannis G. Mikellides. “Neutral gas free molecular flow algorithm including ionization and walls for use in plasma simulations”. In: *Journal of Computational Physics* 230.4 (2011), pp. 1454–1464. DOI: 10.1016/j.jcp.2010.11.013 (cit. on p. 78).
- [27] Ioannis G Mikellides et al. “Evidence of nonclassical plasma transport in hollow cathodes for electric propulsion”. In: *Journal of Applied Physics* (2007), pp. 1–11. DOI: 10.1063/1.2710763 (cit. on p. 80).
- [28] Benjamin A. Jorns, Ioannis G. Mikellides, and Dan M. Goebel. “Ion acoustic turbulence in a 100-A LaB6 hollow cathode”. In: *Physical Review E - Statistical, Nonlinear, and Soft Matter Physics* 90.6 (2014), pp. 1–10. DOI: 10.1103/PhysRevE.90.063106 (cit. on p. 80).
- [29] R. Z. Sagdeev A. A. Galeev. *Nonlinear plasma theory*. New York: W.A. Benjamin, Inc, 1969 (cit. on p. 80).
- [30] Ioannis G Mikellides et al. “Numerical Simulations of a Hall Thruster Hollow Cathode Plasma”. In: *30th International Electric Propulsion Conference*. 2007, pp. 1–12 (cit. on p. 80).
- [31] Saul Dushman. “Electron emission from metals”. In: *Phys. Rev.* 21 (1923), pp. 623–636. DOI: 10.1103/PhysRev.21.623 (cit. on p. 80).
- [32] Ioannis G Mikellides et al. “Numerical Simulations of the Partially Ionized Gas in a 100-A LaB6 Hollow Cathode”. In: *IEEE Transactions on Plasma Science* 43.1 (Jan. 2015), pp. 173–184. DOI: 10.1109/TPS.2014.2320876 (cit. on pp. 80, 85).

- [33] Ioannis G Mikellides et al. “The discharge plasma in ion engine neutralizers : Numerical simulations and comparisons with laboratory data”. In: *Journal of Applied Physics* (2010), pp. 1–12. DOI: 10.1063/1.3514560 (cit. on pp. 82, 85).
- [34] Jesús García Rubiano et al. “Study of the radiative properties of plasma mixtures of interest for ICF chamber design using the ATMED code”. In: *39th EPS Conference on Plasma Physics 2012, EPS 2012 and the 16th International Congress on Plasma Physics*. Vol. 3. 2012, P4.157. ISBN: 9781622769810 (cit. on p. 82).
- [35] R. Rodriguez et al. “Determination and analysis of plasma parameters for simulations of radiative blast waves launched in clusters of xenon and krypton”. In: *Plasma Physics and Controlled Fusion* 54.4 (2012). DOI: 10.1088/0741-3335/54/4/045012 (cit. on p. 82).
- [36] Ioannis G. Mikellides et al. “Investigations of Spot-to-plume Mode Transition in a Hollow Cathode Discharge Using 2-D Axisymmetric Plasma Simulations”. In: *54th AIAA/SAE/ASEE Joint Propulsion Conference, AIAA Propulsion and Energy Forum: American Institute of Aeronautics and Astronautics*. 2018, pp. 1–23 (cit. on p. 83).
- [37] Ioannis G Mikellides et al. “Plasma processes inside dispenser hollow cathodes”. In: *Physics of Plasmas* 13.May (2006), p. 063504. DOI: 10.1063/1.2208292 (cit. on p. 85).
- [38] Dan M Goebel et al. “Hollow cathode theory and experiment. I . Plasma characterization using fast miniature scanning probes”. In: *Journal of Applied Physics* 98.11 (2005), p. 113302. DOI: 10.1063/1.2135417 (cit. on p. 85).
- [39] Ira Katz et al. “Insert Heating and Ignition in Inert-Gas Hollow Cathodes”. In: *IEEE Transactions on Plasma Science* 36.5 (Oct. 2008), pp. 2199–2206. DOI: 10.1109/TPS.2008.2004363 (cit. on p. 85).
- [40] James E Polk et al. “Tungsten and barium transport in the internal plasma of hollow cathodes”. In: *Journal of Applied Physics* 105.0021-8979 (2009), pp. 113301–13. DOI: 10.1063/1.3111970 (cit. on p. 85).
- [41] Angela M Capece et al. “Oxygen transport in the internal xenon plasma of a dispenser hollow cathode”. In: 153302 (2014). DOI: 10.1063/1.4871755 (cit. on p. 85).
- [42] Ioannis G. Mikellides et al. “Evidence of nonclassical plasma transport in hollow cathodes for electric propulsion”. In: *Journal of Applied Physics* 101.6 (Mar. 2007), p. 063301. DOI: 10.1063/1.2710763 (cit. on p. 85).

- [43] Dan M. Goebel and Ira Katz. *Fundamentals of Electric Propulsion: Ion and Hall Thrusters V0*. 2008, pp. 1–507. DOI: 10.1002/9780470436448 (cit. on p. 89).
- [44] Homer D. Hagstrum. “Reflection of Noble Gas Ions at Solid Surfaces”. In: *Physical Review* 123.3 (Aug. 1961), pp. 758–765. DOI: 10.1103/PhysRev.123.758 (cit. on p. 89).
- [45] V. A. Shuvalov. “Energy accommodation for gas ions on a polycrystalline material”. In: *Journal of Applied Mechanics and Technical Physics* 24.6 (1983), pp. 778–785. DOI: 10.1007/BF00905614 (cit. on pp. 90, 104).
- [46] R. Carmina Monreal. “Auger neutralization and ionization processes for charge exchange between slow noble gas atoms and solid surfaces”. In: *Progress in Surface Science* 89.1 (2014), pp. 80–125. DOI: 10.1016/j.progsurf.2014.01.001 (cit. on p. 91).
- [47] H. D. Hagstrum, P. Petrie, and E. E. Chaban. “Interaction of the He⁺ and Ne⁺ ions with Ni(100)-K and Cu(100)-K surfaces having variable potassium coverage”. In: *Physical Review B* 38.15 (Nov. 1988), pp. 10264–10279. DOI: 10.1103/PhysRevB.38.10264 (cit. on p. 91).
- [48] Jørgen E. Hansen and Willy Persson. “Revised analysis of singly ionized xenon, Xe II”. In: *Physica Scripta* 36.4 (Oct. 1987), pp. 602–643. DOI: 10.1088/0031-8949/36/4/005 (cit. on p. 92).
- [49] Homer D. Hagstrum. “Auger Ejection of Electrons from Tungsten by Noble Gas Ions”. In: *Physical Review* 96.2 (Oct. 1954), pp. 325–335. DOI: 10.1103/PhysRev.96.325 (cit. on p. 92).

Chapter 4

LAB₆ HOLLOW CATHODE WORK FUNCTION ENHANCEMENT: INSIGHT INTO THE CHEMICAL PROCESSES.

4.1 Abstract

LaB₆ hollow cathodes have demonstrated robust performance as electron emitters for electric propulsion applications. In Chap. 2 we showed that cathodes based on this material exhibit a transient thermal behavior during the first 50 hr of operation that we attributed to a reduction in the work function of the cathode emitter. In Chap. 3 we built a self-consistent thermal-plasma model that confirmed the reduction in the work function, estimating it at ~ 2.25 eV. This value is much lower than the polycrystalline work function value for LaB₆ of 2.67 eV. In the present work we establish the possible chemical reasons for such improvements and study them with chemical analysis. The hypotheses for the reduction include crystallographic evolution of the polycrystalline sample, phase change of the emitting surface, forced lanthanum termination of naturally occurring boron-terminated crystals and chemical poisoning of the surface. In order to investigate these hypotheses, we designed and built a modified insert which contains a small portion of flat emitting surface exposed to the collisional plasma in the cathode interior. This small piece was built to be removable and therefore, we could extract it from the cathode and place it inside an ultraviolet photoelectron spectrometer (UPS) for work function measurements, electron backscatter and an X-ray diffractometer for crystallographic measurements, secondary electron microscope for morphology identification, and a profilometer for topology characterization. The results from these analyses allowed us to characterize the morphological and chemical modification resulting from the action of the plasma on the emitting surfaces of a LaB₆ cathode running at 25 A and 13 sccm. They also aided in isolating the mechanism behind the lowering of the work function. Work function measurements with UPS confirmed that the work

function is reduced permanently after plasma exposure. However, there may also be secondary factors that further reduce the work function temporarily during operation, such as forced La termination. No phase change was observed at the surface of the sample after cool down. Finally, we observed a crystallographic texture formed by the action of the ions impacting on the walls of the cathode emitter, which can explain the work function reduction. The work function reduction due to the action of the cathode plasma is a recently found phenomenon [1] which greatly benefits the lifetime of LaB₆ hollow cathodes. As a result of identifying the mechanism behind the reduction, we can now pre-process the inserts that will be used in space cathodes to yield the best possible lifetime. Similarly, we can design the geometry of the cathode to make sure the beneficial crystallography is exposed throughout the lifetime of the cathode.

4.2 Introduction

Electric propulsion (EP) plays a crucial role in space exploration, from satellite station keeping to deep space exploration. Ion thrusters and Hall effect thrusters have proven to be very useful tools, allowing us to reach further into the unknown. Furthermore, higher power technologies like the magnetoplasmadynamic (MPD) thrusters promise to increase the application range of EP devices [2]. Hollow cathodes are essential components for the performance of any of these thrusters, to such a great degree, that if the cathode fails prematurely, the whole thruster is rendered unusable.

Unfortunately, cathodes are complex devices which require a multiphysics approach to fully understand them. At the heart of the behavior of hollow cathodes is the cathode plasma which provides a conductive medium that connects the electron emission source to the thruster plasma or ion beam. The electron emitter provides the electrons necessary to sustain the cathode plasma and for the thruster operation. The materials used as electron emitters must share several characteristics; low work function, low evaporation rate and robustness to propellant impurities, among others. Several materials have been selected and tested throughout the years to be used as emitters. Two technologies are widely

used today in electric thrusters, namely: BaO-W and LaB₆ [3].

LaB₆ hollow cathodes have proven to be a very robust technology after many years of use in operating spacecraft. However, the specifics of their operational behavior are still evading our understanding. In our previous work [1], we found that the cathode behaves as if it had a work function lower than the classically accepted value for LaB₆ vacuum cathodes, 2.67 eV [4]. In order to estimate precisely the work function of LaB₆ in the hollow cathode configuration, we built a coupled 2D axisymmetric plasma and thermal model [5]. Based on the final result for the coupled system we estimate a work function of 2.25 eV for the cathode with a 25 A discharge and 13 sccm mass flow rate of xenon. This is 0.42 eV lower than the vacuum cathode value.

The specific mechanism responsible for the reduction in work function is of great importance, not only from a purely scientific point of view, but also from an engineering one. Once the mechanism for the reduction is identified, we can potentially use it to engineer LaB₆ hollow cathodes for even lower operating temperatures throughout the lifespan of the cathode. With this new design, we could maximize the lifetime of polycrystalline LaB₆ cathodes.

The work function of a crystalline solid is a surface property of its crystals. It is an energy barrier established by the local environment of the crystal atomic structure at the surface. Therefore, it can be affected by numerous mechanisms. It is challenging to isolate a singular mechanism that can impact the work function in a given direction, because work function is determined by fine details of the atomic structure at the material surface. We have used published results from density functional theory [6, 7] (DFT) to elaborate the hypothetical mechanisms behind the work function reduction in LaB₆ presented in this work. We have identified four possible mechanisms that could improve the work function of polycrystalline LaB₆:

1. **Formation of a crystallographic texture** promoted by the preferential removal of high surface energy crystals by ion bombardment of the emitting surface of the cathode. A polycrystalline LaB₆ sample contains a random

distribution of crystals. Each crystal orientation exhibits different work function and different surface energy. We hypothesise that the action of plasma ions upon the grains of the polycrystalline sample could preferentially etch grain surfaces whose surface energies are high. The energy of those ions must be below the sputtering threshold of LaB_6 (~ 50 eV), otherwise the etch would not discriminate on the basis of surface energy. As this process evolves, the initial random distribution of crystals at the surface of the polycrystalline sample would evolve into a surface composed of grain surfaces that are highly stable (low surface energy). The relation between low surface energy crystals and low work function has been studied in the work of Uijtewaal [6].

2. **Formation of LaB_4** due to the re-crystallization of LaB_6 in a La-rich environment. In Chap. 2 we showed that the mean free path for evaporated La atoms is on the order of the cathode interior dimensions, and therefore, we expect it to be ionized. Given the cathode plasma distribution, ionized La must be driven back to the emitting surfaces of the cathode where it will interact with the polycrystalline surface of LaB_6 responsible for the thermionic discharge of the cathode. Given the high temperatures of the surface and the constant bombardment with La ions, we hypothesize that re-crystallization of LaB_6 into the more metallic phase LaB_4 might occur. The work function for LaB_4 is not known, but considering its highly metallic character we expect its work function to be comparable to LaB_6 , or possibly better. If that is correct, the formation of LaB_4 could be the reason behind the reduction of the work function.
3. **Formation of a cationic termination** in otherwise naturally occurring boron-terminated crystals. When La ions reach the surface of the insert, they could stick to the surface like adatoms without affecting the crystalline structure of LaB_6 . DFT results have shown that cationic terminations of crystals (La terminations in compounds La-B) are responsible for the low work function of LaB_6 crystals. A polycrystalline sample of LaB_6 is composed of a mix of La and B terminated crystals, with the work function of the first group much lower than that of the second. We hypothesize that the return

flux of La ions could force the B-terminated crystals into their La-terminated counterpart, yielding a reduced work function behavior of the solid.

4. **Formation of a surface complex** upon the interaction of LaB_6 with some undetermined chemical species outgassed from a component in the vicinity of the emitter. There could be a chemical species evaporated from the high temperature components that exist close to the insert that could reduce the work function of LaB_6 by the formation of a favorable dipole on its surface. Cesium is the only well known work function enhancer for LaB_6 [8]. We do not have any source of Cs anywhere near the insert, therefore, we have excluded that possibility. In general, other work function enhancers are possible (metals with lower electronegativity than the one for boron). Thus, we are not excluding this possibility entirely.

The polycrystalline LaB_6 inserts used in our studies are manufactured from LaB_6 powder synthesized using carbothermal reduction [9] and subsequently milled into 2 μm mean grain size. The powder was manufactured by Treibacher Industrie AG. The powder was then sintered into a billet by means of hot isostatic pressing in a Ta crucible by Exothermics Inc. Subsequently, the billet is machined into the final shape of the emitter using electro-discharge-machining (EDM). Throughout the synthesis of the powder, consolidation into the billet, and machining into the final emitter shape, there is no mechanism that preferentially exposes any one type of LaB_6 crystal at the surface. Thus, the exposed crystallographic orientation at the surface of the emitter does not show any specific crystallographic texture; it is completely random. That is the state of the emitting surface when the work function of polycrystalline LaB_6 samples is measured by means of a Richardson plot in a vacuum diode test cell.

In this work, we have studied the effect of the hollow cathode plasma interacting with the emitting surface of a polycrystalline LaB_6 insert. To that end we have built a slightly modified version of the classical cylindrical shaped insert, with the objective of exposing a flat surface of LaB_6 to the plasma. We then operated the cathode uninterruptedly for 50 hr at 25 A and 13 sccm. We have characterised

the effect of the plasma on the surface by means of crystallographic, chemical and morphological analyses. Upon comparison of the data obtained with the control measurements taken in the unexposed sample, we were able to determine that formation of a crystallographic texture likely contributes to the work function reduction.

4.3 Methods

The objective of this work is to elucidate, from a chemical point of view, what causes the work function reduction in the LaB₆ hollow cathode configuration. We have focused our attention on the case where the cathode is operating at 25 A and 13 sccm. From our previous experience at this operating condition, we know that the cathode exhibits a transient behavior during the first 50 hr of operation and at that point, the thermal response of the cathode is very stable. Thus, we replicated that experiment but this time we used a modified insert that could help us understand the chemical evolution that occurs during the transients.

We prepared an experiment that consisted of exposing a polycrystalline LaB₆ sample for the first time since manufacturing to Xe plasma in the cathode over a period of 50 hr. The shut down sequence was designed to minimize any further evolution of the thermionic surface due to the cool down transient of the cathode. We designed a special vacuum chamber to cool down the cathode as quickly as possible after the experiment to reduce further chemical evolution of the thermionic surface due to high temperature (diffusion of chemicals at the surface or recrystallization). The chamber is described in section 4.3.1. We obtained very steep cool down rates (starting at 246 °C/min) and total cool down of the insert in 5 hr. Additionally, we kept the Xe flow running until the insert temperature reached room temperature to prevent any chemicals from the vacuum chamber from reaching the sensitive thermionic emitter surface while it cools down from operating temperature (> 1200 °C).

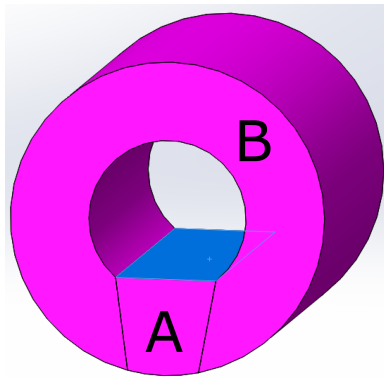


Figure 4.1: Modified insert geometry used in this study. Total inner area available for thermoemission is reduced by 1.72% with respect to an unmodified cylindrical insert.

4.3.1 Test article and facility – insert, cathode and chamber

The cathode setup used in this experiment was described in Chap. 2 and 3. The only difference with that configuration is the use of a modified insert geometry in this study. The modified insert is shown in Fig. 4.1. The insert consists of two pieces, part A and part B. Part A is held in place by its own weight in part B. Part A can be easily placed inside part B as in Fig. 4.1 and it can also be easily removed and transported for chemical analysis. This new geometry has an available area for thermionic electron emission 1.72% smaller than the original insert.

The chamber in which this experiment ran has a volume of $22 \times 10^{-3} \text{ m}^3$ and two 10" cryopumps arranged in opposite directions to each other (Fig. 4.2), the cathode sits between them (Fig. 4.3).

4.3.2 Operating conditions

The cathode operating point chosen for the 50 hr test had been studied previously and results were shown in Chap. 2 and 3. The discharge was set at 25 A and the mass flow rate at 13 sccm.

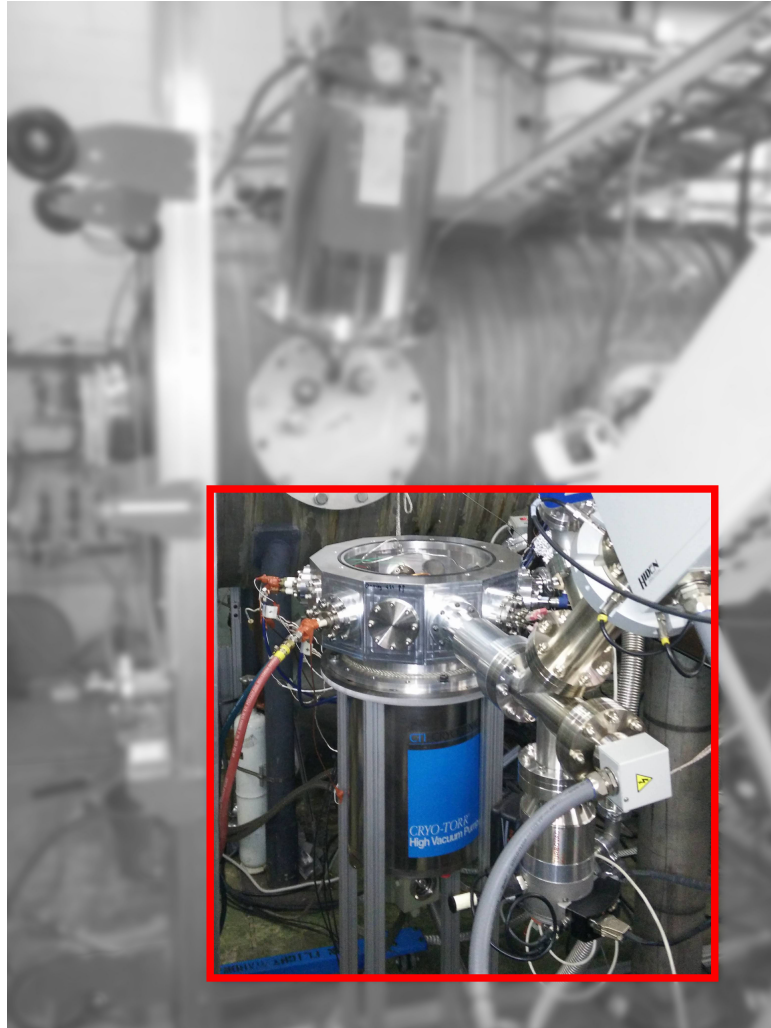


Figure 4.2: Vacuum chamber used in the experiment.

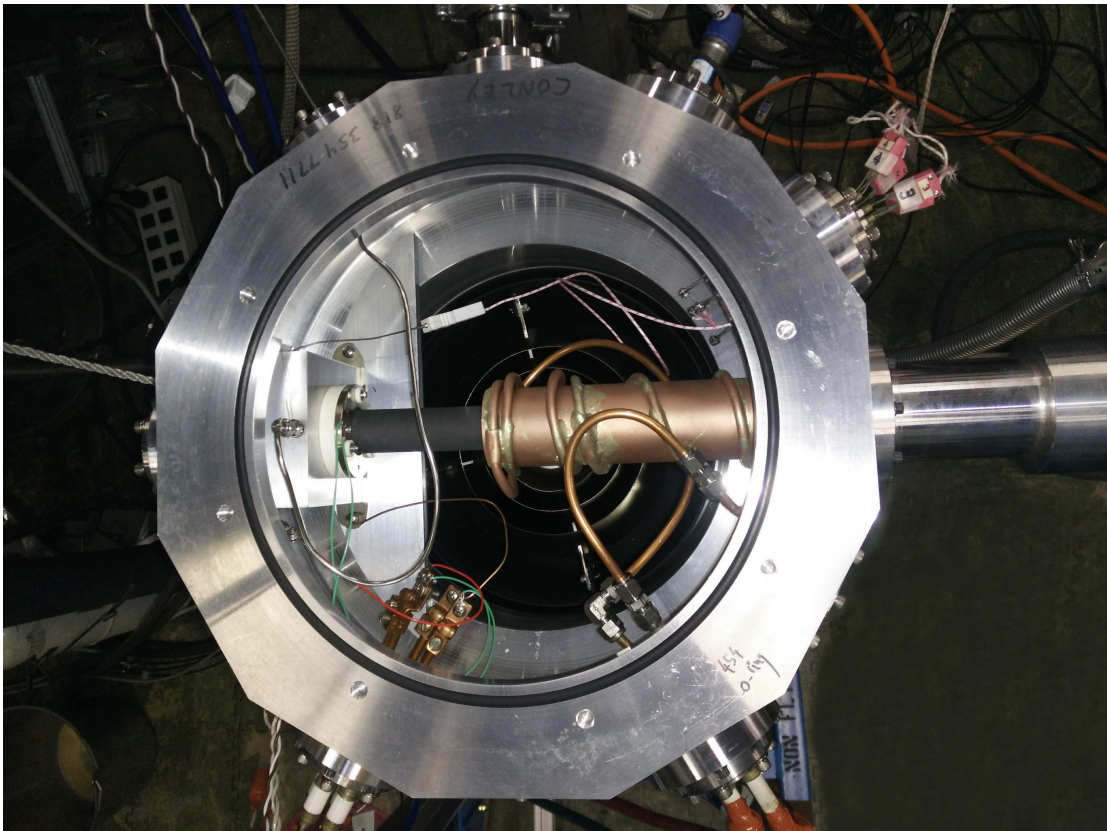


Figure 4.3: Cathode assembly inside vacuum chamber.

4.3.3 Surface morphology characterization – scanning electron microscopy (SEM) and profilometry

In order to visualize the effect of the plasma on the sample of LaB_6 , a series of high resolution images were obtained using a scanning electron microscope, ZEISS 1550VP FESEM. This device is located at the Caltech GPS Division Analytical Facility. The objective was to characterize the surface before and after plasma exposure. In SEM, accelerated electrons are forced to collide against a surface. When the electrons interact with the sample, they are decelerated by inelastic collisions, producing a variety of signals. One of these signals is the secondary electron emission, which is used to produce SEM images. Backscattered electrons are also emitted and they are mostly used for illustrating contrasts in composition in multiphase samples.

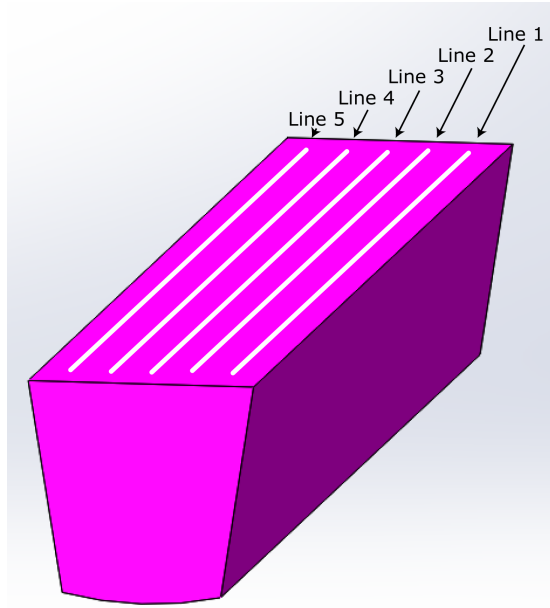


Figure 4.4: Test sample (part A). Depicted are the paths along which the profilometer was used to acquire the topology of the sample.

To quantify the effect that the plasma had on the morphology of the surface exposed to the plasma of part A (highlighted surface in Fig. 4.1), we used a DektakXT stylus profilometer. This device is located at the Caltech Molecular Materials Research Center. Stylus profilometers measure the surface profile of a sample by physically moving the tip of a probe along the sample surface. The method consists of applying a constant force to the stylus and maintaining it through a feedback loop. The change in the height of the arm holder is then measured and the profile can be reconstructed from the data. The radius of the stylus is $2\ \mu\text{m}$, profile configuration was “*Hills and Valleys*” and the stylus force was 3 mg. We selected the best possible resolution depending on the surface roughness present in the sample, which was either $6.5\ \mu\text{m}$ or $65.5\ \mu\text{m}$ peak to peak. Profiles along five straight lines were obtained before and after the plasma exposure. Those lines are shown in Fig. 4.4. Note that the profile could not be extended to the edges of the sample due to limitations in the apparatus.

4.3.4 Direct work function measurement – ultraviolet photoelectron spectroscopy

The work function was measured directly in the test sample after plasma exposure along Line 3 (see Fig. 4.4) in 15 different locations by ultraviolet photoelectron spectroscopy (UPS) using a Kratos Ultra spectrometer located at the Caltech Molecular Materials Research Center.

In UPS, ultraviolet light from a helium discharge source is shined on the location of interest. As a result, electrons of the sample get excited and photoemitted from the surface. By measuring the kinetic energy of the electrons emitted and subtracting the incident photon energy, one can measure the binding energy of the photoemitted electrons. UPS can therefore be used to measure the work function of a sample. The work function is the energy difference between the Fermi level and the vacuum level of a sample. The Fermi level is the highest energy level of an electron in a sample at absolute zero temperature. The work function can be spectroscopically acquired by measuring the difference between the Fermi level and the cutoff of the tail at the low kinetic energy end of the photoemitted electrons of the sample, and subtracting this value from the incident photon energy (see Fig. 4.5).

After the 50 hr test finished, the sample was exposed to the atmosphere in order to be transported from the vacuum chamber where the cathode was run (Jet Propulsion Laboratory), to the UPS instrument located at Caltech. The work function was also measured at five randomly chosen locations in a control sample. The control sample belongs to the same billet from which the insert was extracted. The surface of the control sample where the work function was measured was produced by cracking a control piece of LaB₆ with a pair of pliers right before introducing it into the UPS. The exposure of that sample to the atmosphere was less than 10 min. To account for possible area effect on the work function measurement, we used five different focusing lenses in the UPS instrument. According to the manufacturer of the apparatus, the different settings correspond to the following approximate areas: $1 \times 1 \text{ mm}^2$, $110 \times 110 \text{ }\mu\text{m}^2$, $55 \times 55 \text{ }\mu\text{m}^2$, $27 \times 27 \text{ }\mu\text{m}^2$ and $15 \times 15 \text{ }\mu\text{m}^2$. We checked the calibration of this technique by measuring the work

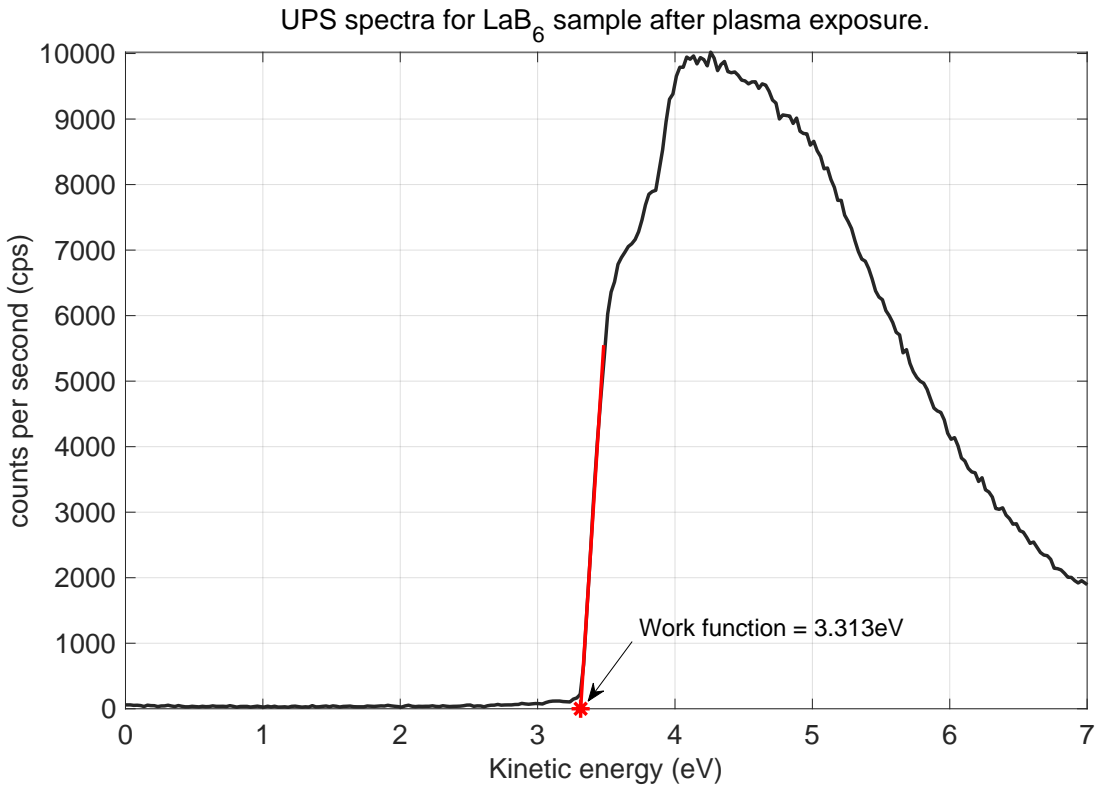


Figure 4.5: UPS spectra for the LaB₆ test article after plasma exposure at location $\bar{z} \sim 0.884$ (see Fig. 4.14) obtained with aperture $110 \times 110 \mu\text{m}^2$.

function of a sputtered polycrystalline gold sample at one location, using each of the aforementioned apertures, and obtained a value which deviates from the nominal value of 5.1 eV by less than 0.014 eV, a mean 5.086 eV with a standard deviation 0.037 eV.

4.3.5 Phase identification – X-ray powder diffraction and electron backscatter diffraction

X-ray powder diffraction (XRD) and electron backscatter diffraction (EBSD) are techniques useful for the characterization of the different phases present in a sample. Both of these techniques require flat samples to obtain meaningful results, which drove us to the design shown in Fig. 4.1.

EBSD is a surface analysis technique that allows quantitative microstructural analysis in SEM up to a nanometer scale. In this method, a beam of electrons is focused at the point of interest on a tilted sample, typically at 70° from the normal to the surface. Upon inelastic interaction between the impinging electrons and the atomic structure of the sample surface, scattered electrons form a divergent source of electrons close to the surface of the sample. Some of those electrons interact with the structure at angles that satisfy the Bragg equation: $n\lambda = 2d \sin(\theta)$ where n is an integer, λ is the wavelength of the electrons, d is the spacing of the diffracting plane, and θ the angle of incidence of the electrons on the diffracting plane. The diffracted pattern is recorded on a phosphor screen where the so-called Kikuchi bands are recorded. Each Kikuchi band can be indexed by the Miller indices of the diffracting crystal plane which formed it, thus enabling crystallographic identification. By comparing the measured Kikuchi patterns with known patterns from a database, phase identification can be obtained. Penetration depth in the order of 10 nm is characteristic for this technique, albeit dependent on the material. We applied this technique at locations of interest in the test sample after it was used in the 50 hr run test. The area analyzed in each case was 1 mm^2 . The speed of acquisition was 40.53 Hz and the accelerating voltage was 20 kV. The EBSD system used was manufactured by KHL Technology and is located at the Caltech GPS Division Analytical Facility.

XRD is another surface analysis method that provides information about the crystalline nature of materials at penetration depth of around $10 \mu\text{m}$. Similarly to EBSD, XRD employs constructive interactions between X-rays and atomic structures, producing patterns that can be recorded and used against database information to deconvolve the different phases present in the sample. The directions of possible diffractions depend on the size and shape of the unit cell of the material. The relative intensities of the diffracted X-rays depend on the kind and arrangement of atoms in the crystal structure. In order to produce a unique pattern from a crystalline material, the atomic structure needs to be exposed to the incident X-ray beam in every possible direction. This is obtained in practice by producing a powdered sample from the crystalline material of interest. The powdered sample is typically called a polycrystalline aggregate or powdered material. When a powder

with randomly oriented crystallites is placed in an X-ray beam, the beam will expose all possible interatomic planes. If the experimental angle is systematically changed, all possible diffraction peaks from the powder will be detected by the scintillation detector. By comparing the measured peak and intensity patterns with known patterns from a database, phases can be identified. We utilized a PANalytical X'pert³ XRD with Bragg-Brentano geometry operated by Professor K. Faber's group at Caltech. The data was acquired at 0.31 °/min.

4.3.6 Crystallographic texturing – X-ray powder diffraction

X-ray diffraction as a technique is similar to measuring the diffraction from a single crystal that is rotated in every possible direction with respect to a fixed incident X-ray source. From that point of view, the XRD pattern represents the result of a perfectly random distribution of crystal orientations in the powder sample or similarly in the polycrystalline solid sample (our test article). This situation is described by saying that there is no crystallographic texture in the polycrystalline solid sample. As a consequence of this, if a texture is present in the sample, the relative intensities of the XRD peaks will change.

4.4 Results

4.4.1 Cathode operating conditions

The cathode was operated for 50 hr in the aforementioned vacuum chamber and its performance was measured with the data acquisition system introduced in Chap. 2. Fig. 4.6 shows the temperature of the insert measured with a Type C thermocouple for the 50 hr test. Fig. 4.7 shows the shut down procedure and cool down curve. Fig. 4.8 shows the main discharge voltage, current and keeper voltage during the test. Fig. 4.9 shows the vacuum chamber pressure and Xe mass flow rate fed into the cathode.

In Fig. 4.6 we can observe a temperature transient somewhat similar to the one introduced in Chap. 2, Fig. 2.3. The behavior of the transient is similar in terms of showing a fast cool down during the first 5 hr of the cathode operation

and slower cool down during the following 45 hr. Of note, while the transients were highly reproducible, at this time we observed a temperature at steady state about 200 °C higher. Once we disassembled the cathode, we found that most of the thermionic active area of the insert part B was coated in black, see Fig. 4.10. The source of this contamination is most likely the graphite pusher placed upstream of the insert. Prior to this 50 hr test, the cathode assembly (including the pusher but excluding the insert) was thoroughly outgassed. The outgassing lasted for ~24 hr at 1300 °C. It is unclear whether the outgassing procedure was insufficient (higher temperature or longer processing time required) or this contaminant is sputtered off the pusher walls by energetic ions. Insert temperature increments due to carbon contamination have already been observed, see Chap. 2, Fig. 2.8 and 2.7. We believe that this contamination is the reason for the abnormal temperature at steady state in this test. Fortunately, the carbon contamination did not affect the test article (part A) significantly. Nonetheless, these observations highlight an important unsolved problem with LaB₆ cathodes, namely material compatibility. Graphite is considered as the best suited material to be in contact with LaB₆ at high temperature given the knowledge available in the literature and from practitioners in the field. This is also true given our own experience. However, in light of the contamination issues introduced here, more work needs to be done to perfect its utilization.

4.4.2 Morphology identification – scanning electron microscopy (SEM)

In Fig. 4.11 the microscopic evolution of the morphology of the surface of the material can be observed. The image on the left corresponds to a surface that was produced by electrical discharge machining (EDM) from the billet as the test sample. On the right we can observe the test sample after exposure to the cathode plasma for 50 hr. The most remarkable detail in the pictures is the faceted appearance of the surface that corresponds to the area of the test sample exposed to the high density plasma (downstream side or right hand side in Fig. 4.11). On the left hand side of the test sample (exposed to a much lower plasma density), the surface morphology seems to be increasing in roughness but facets are not visible.

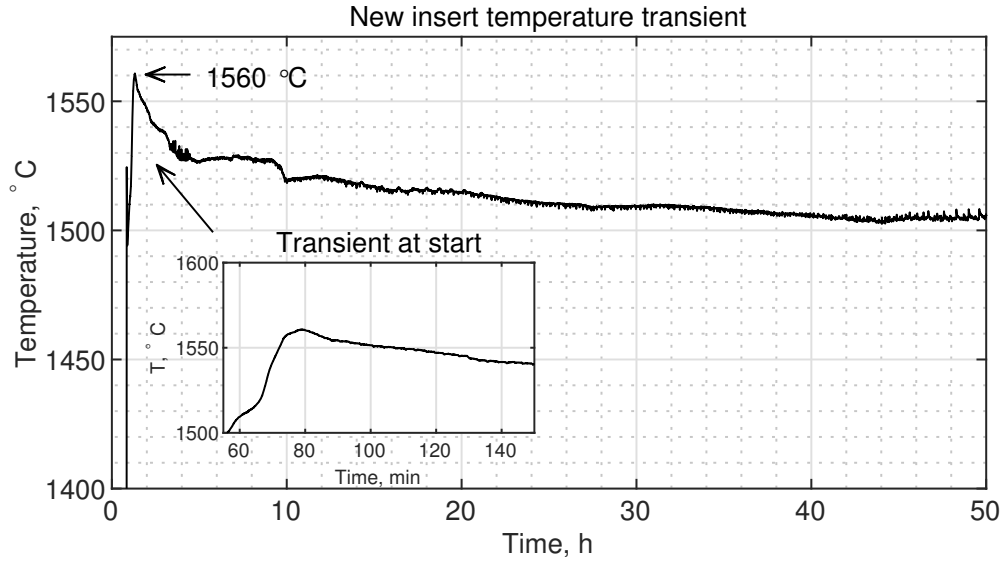


Figure 4.6: Thermal transient for a new insert at $J_D = 25$ A and $\dot{m}_{Xe} = 13$ sccm with the nominal orifice.

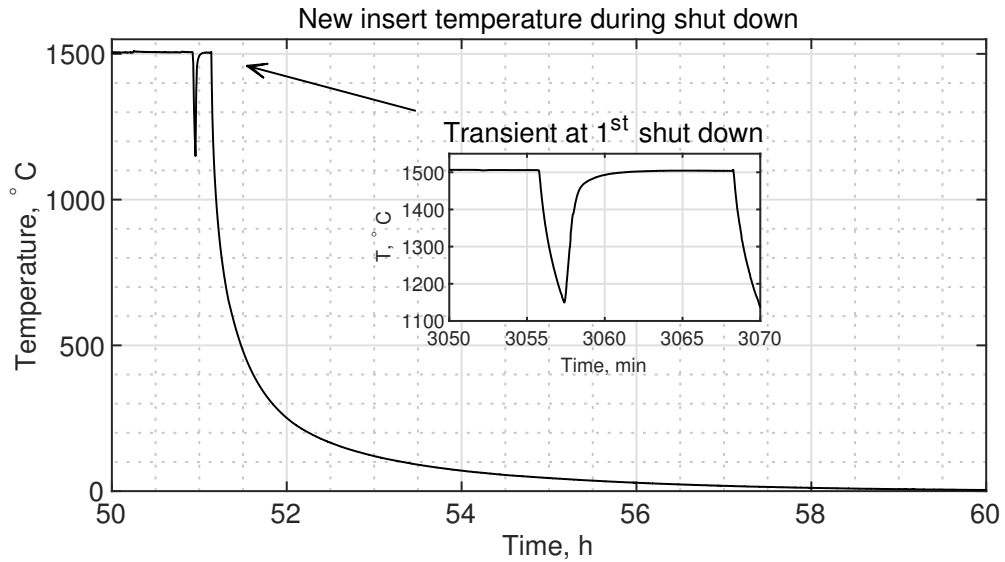


Figure 4.7: Thermal transient during shut down.

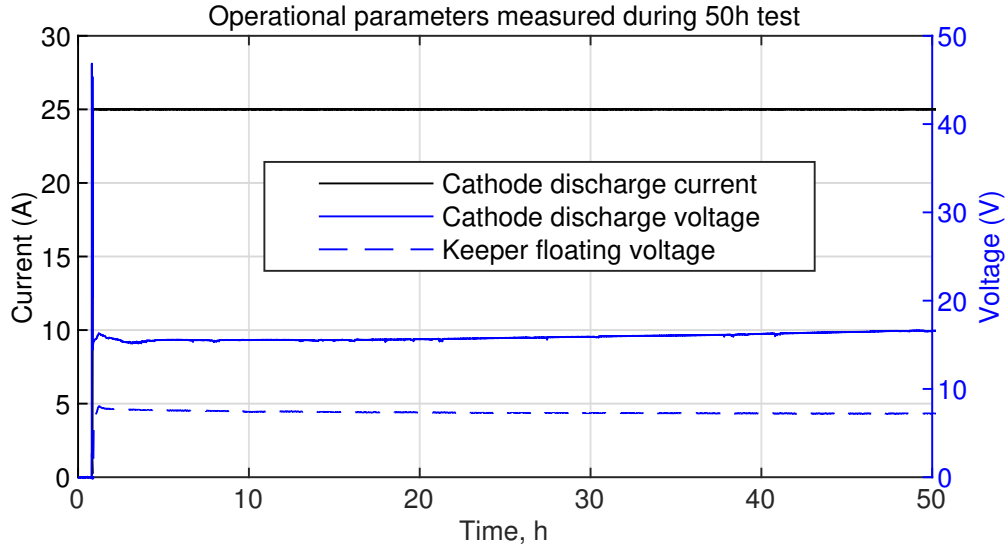


Figure 4.8: Cathode operational parameters measured during 50 hr test: discharge voltage and current, and keeper voltage.

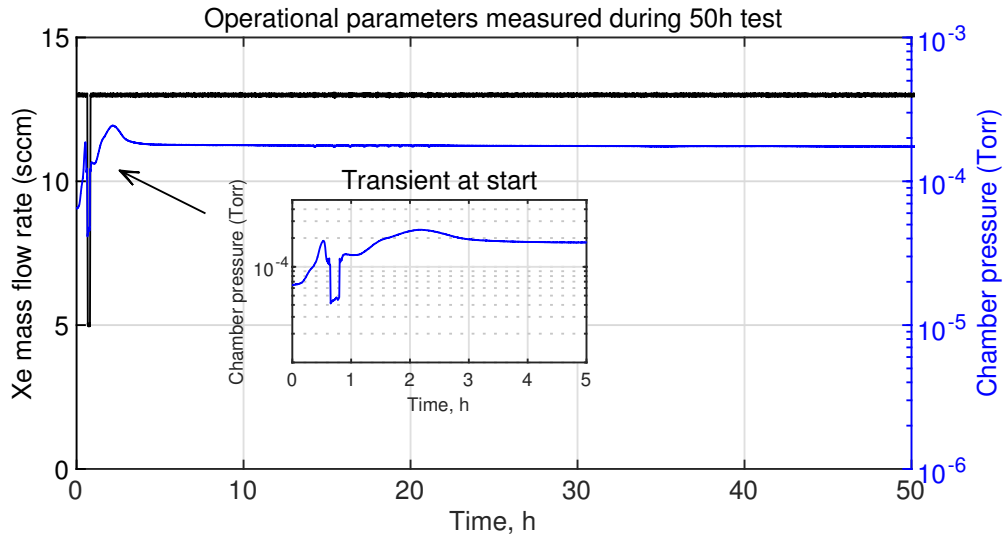


Figure 4.9: Cathode operational parameters measured during 50 hr test: chamber pressure and Xe mass flow rate.



Figure 4.10: Test sample (part B) after the 50 hr test. Sample shows carbon contamination in most of its internal area.

4.4.3 Topology characterization – profilometry

The profiles measured along the five lines depicted in Fig. 4.4 before plasma exposure are shown in Fig. 4.12 and for the sample after plasma exposure in Fig. 4.13.

As can be observed, the sample roughness after EDM is on the order of $2\ \mu\text{m}$ peak-to-peak and deviation from flatness is on the order of $1\ \mu\text{m}$. The spikes in Fig. 4.12 are small imperfections in the surface.

In Fig. 4.13 the profiles after plasma exposure show a roughness on the order of $2\ \mu\text{m}$ peak-to-peak in the upstream region of the sample ($\bar{z} \sim 0.1$) that increases up to $8\ \mu\text{m}$ peak-to-peak in the downstream region. Furthermore, we can observe

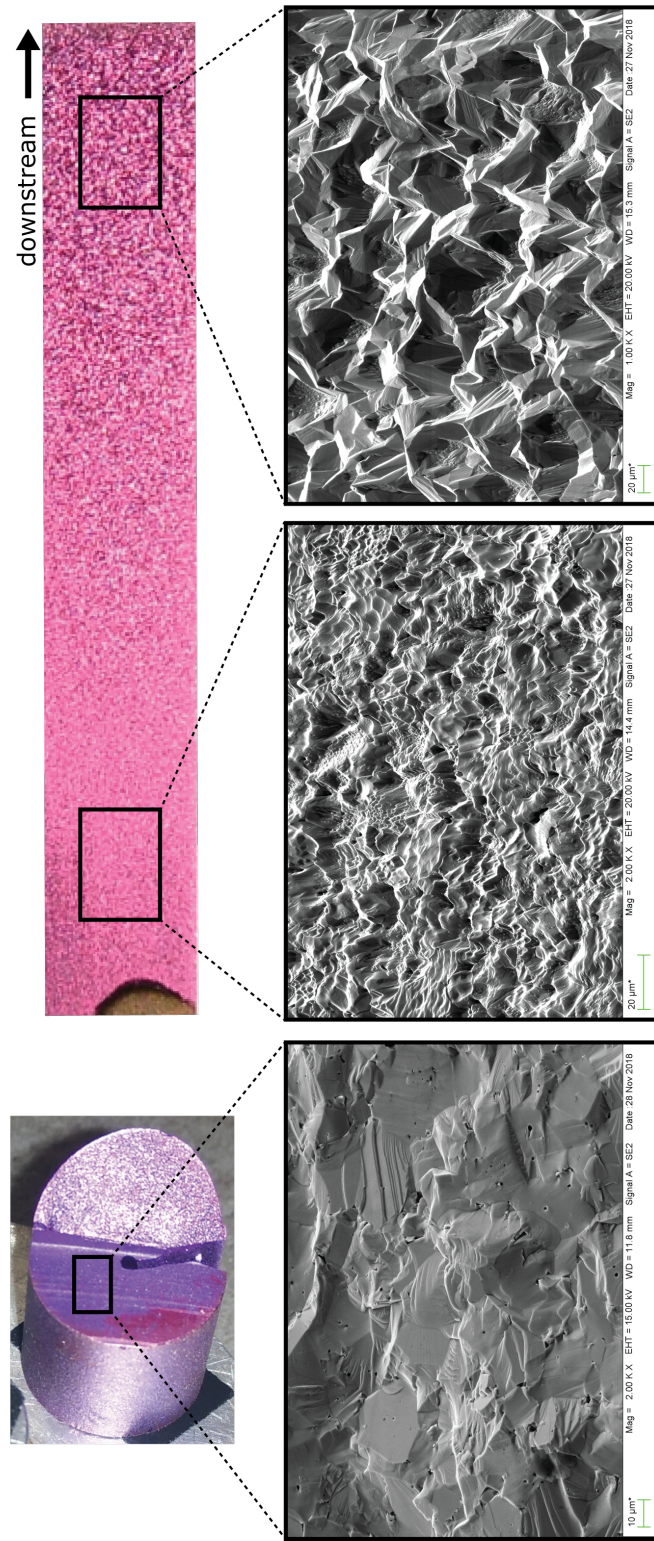


Figure 4.11: On the left, SEM image collected from a sample after manufacturing. On the right, SEM pictures from the test sample after exposure to plasma. Note the slight difference in the scale of the images. The orientation of the test sample indicates the downstream end of the cathode (towards the orifice plate).

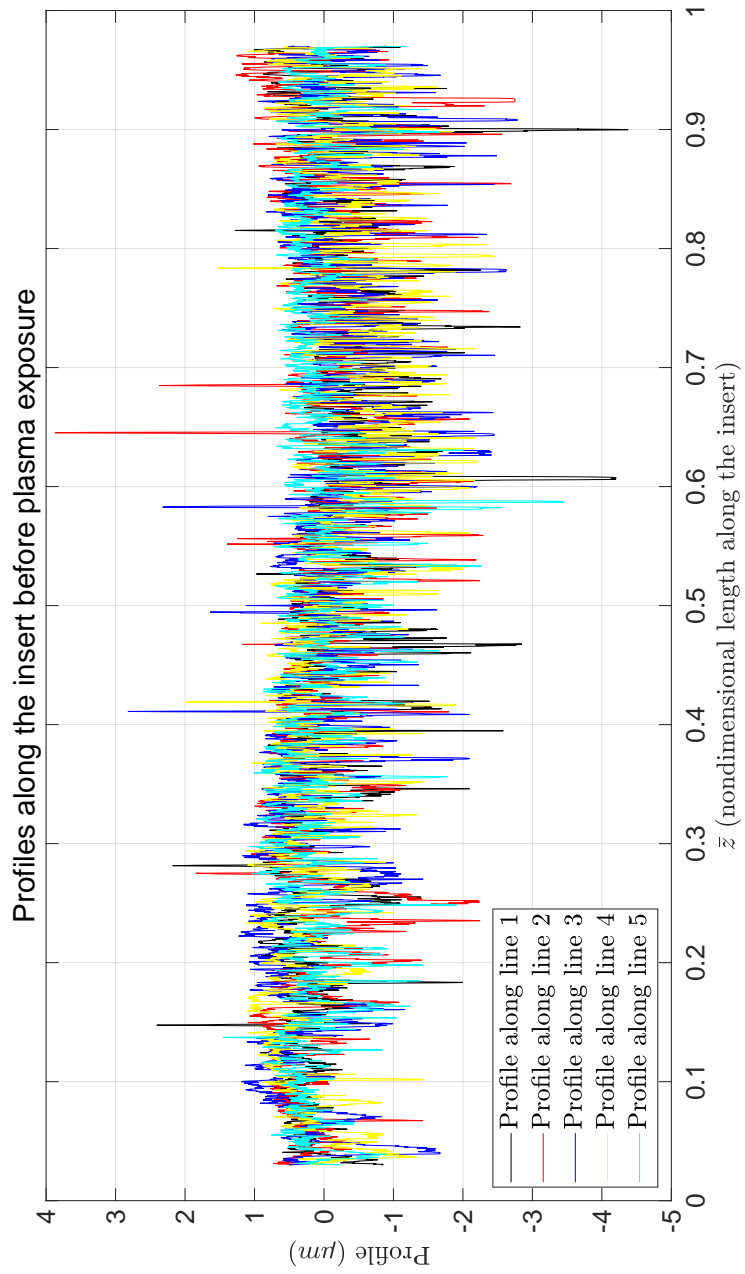


Figure 4.12: Surface profiles acquired before plasma exposure

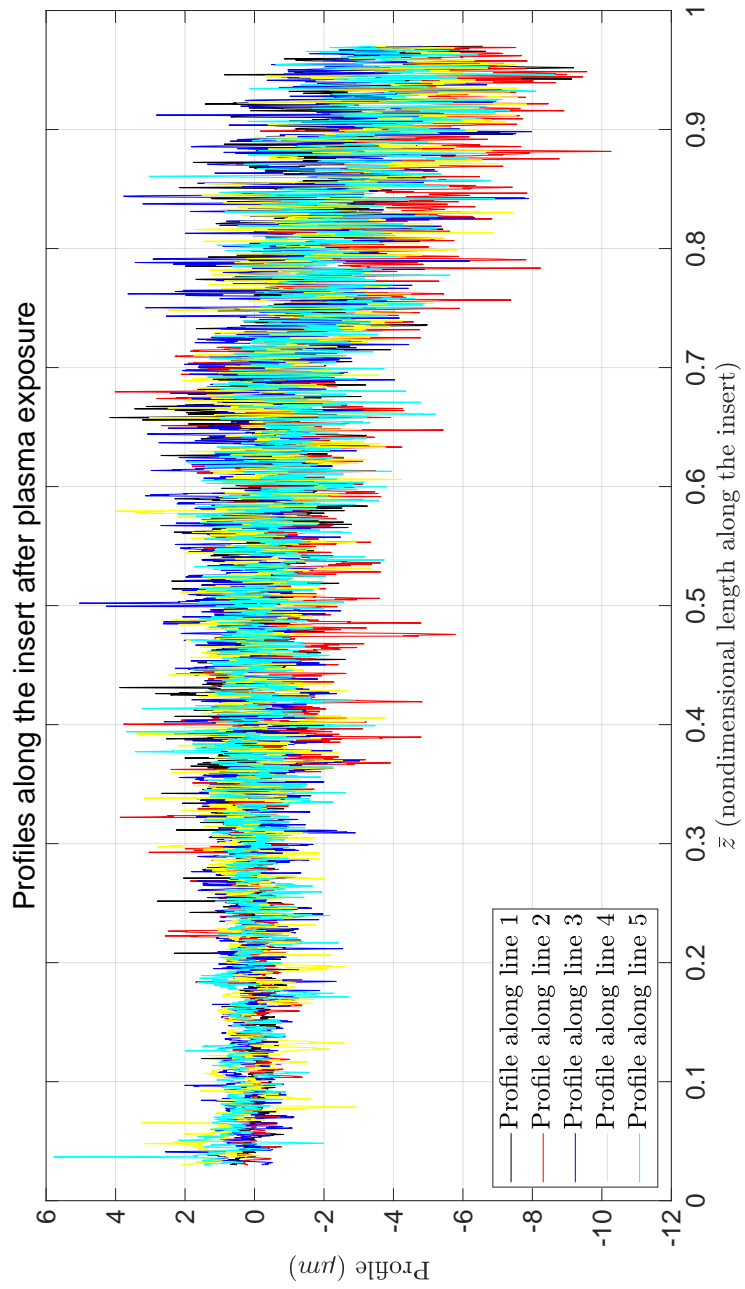


Figure 4.13: Surface profiles acquired after plasma exposure

the profiles deviating from the upstream flat region which correspond to the mass of insert lost due to the action of the downstream high density plasma. These results are in agreement with the morphology observed qualitatively in Fig. 4.11.

4.4.4 Direct Work function measurement – ultraviolet photoelectron spectroscopy

Results for the work function measurements are shown in Fig. 4.14. There are five color bands that correspond to the work function measurement obtained in the control sample in five randomly chosen locations. At every location, the work function measurements were acquired five times with increasing aperture size of the UPS.

4.4.5 X-ray powder diffraction results

XRD spectra before and after plasma exposure are shown in Figs. 4.15 and 4.16. In Fig. 4.15 it is obvious that the XRD profiles before and after the test sample was exposed to the cathode plasma are not aligned with the lines that represent the peak locations for LaB_4 . On the other hand, the match is significant when we compare the profiles with the peak locations for LaB_6 , see Fig. 4.16.

4.4.6 Electron backscatter diffraction results

The results from the EBSD analysis can be found in Fig. 4.17. The phase identification map on the left corresponds to a 1 mm^2 area in the upstream end of the test sample, whereas the one on the right corresponds to the downstream end. As can be seen, the Kikuchi patterns belong to crystalline LaB_6 . The patterns were also compared with La oxide, B oxide and LaB_4 . Similarly to the XRD results, EBSD did not detect the presence of crystalline LaB_4 .

4.5 Discussion

Work function measurement by UPS

UPS was employed to directly measure the differences in work function at plasma-

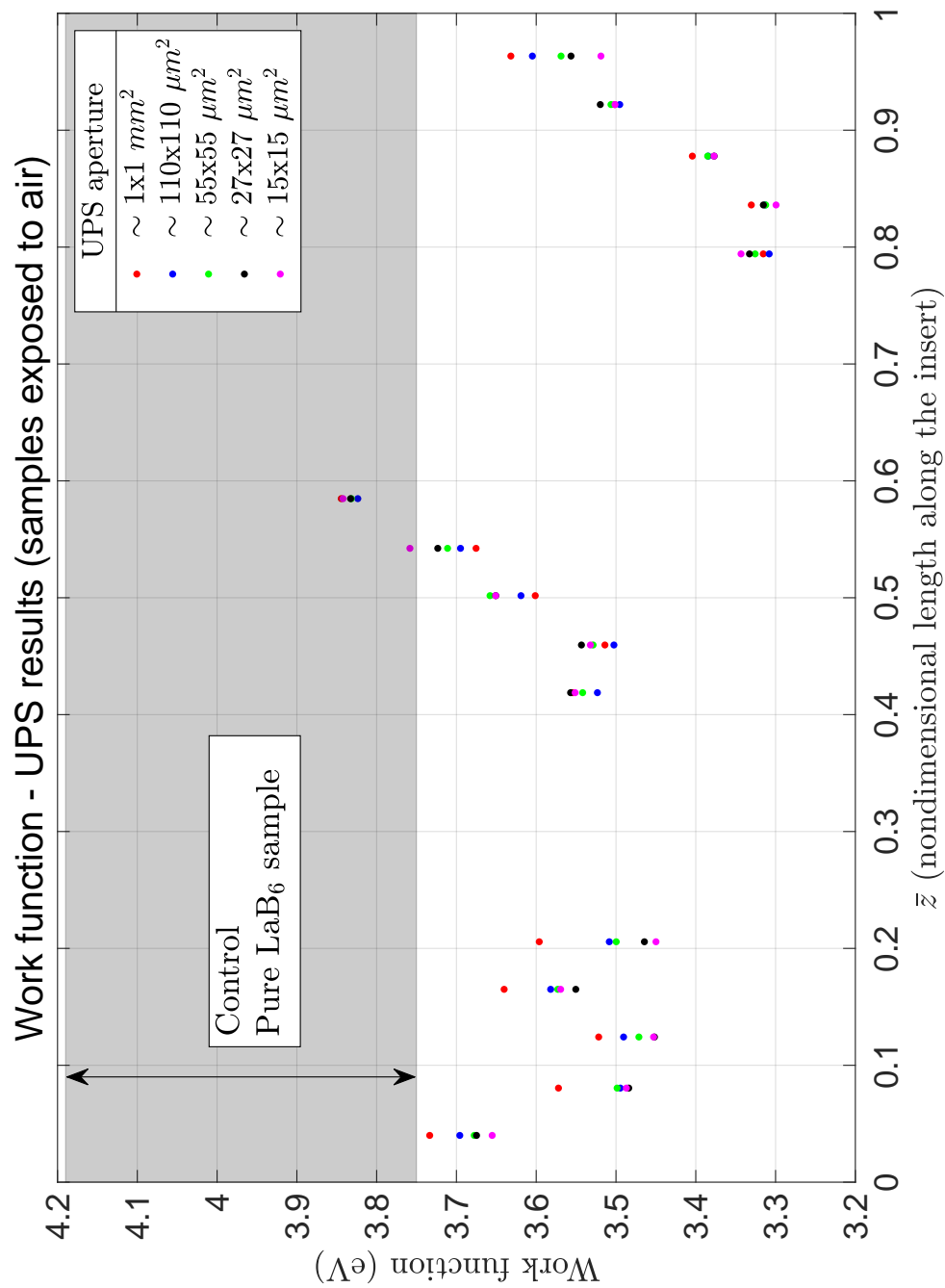
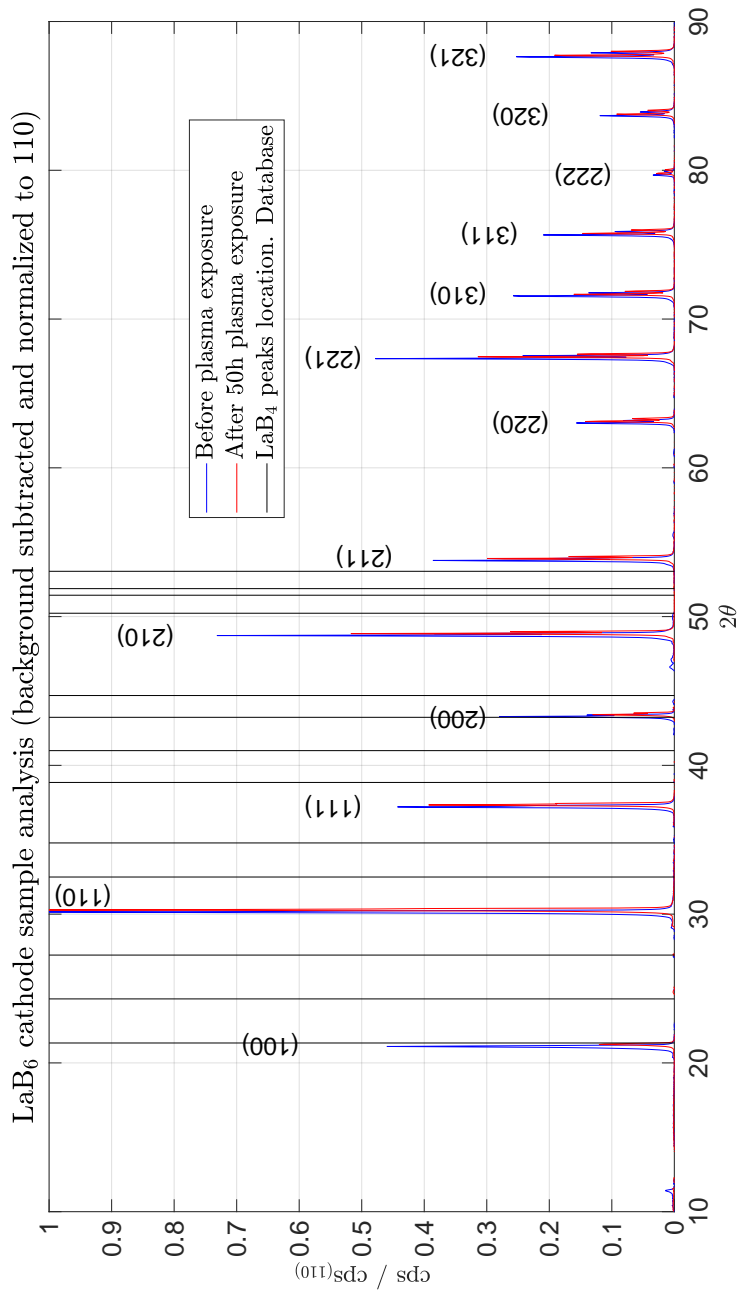
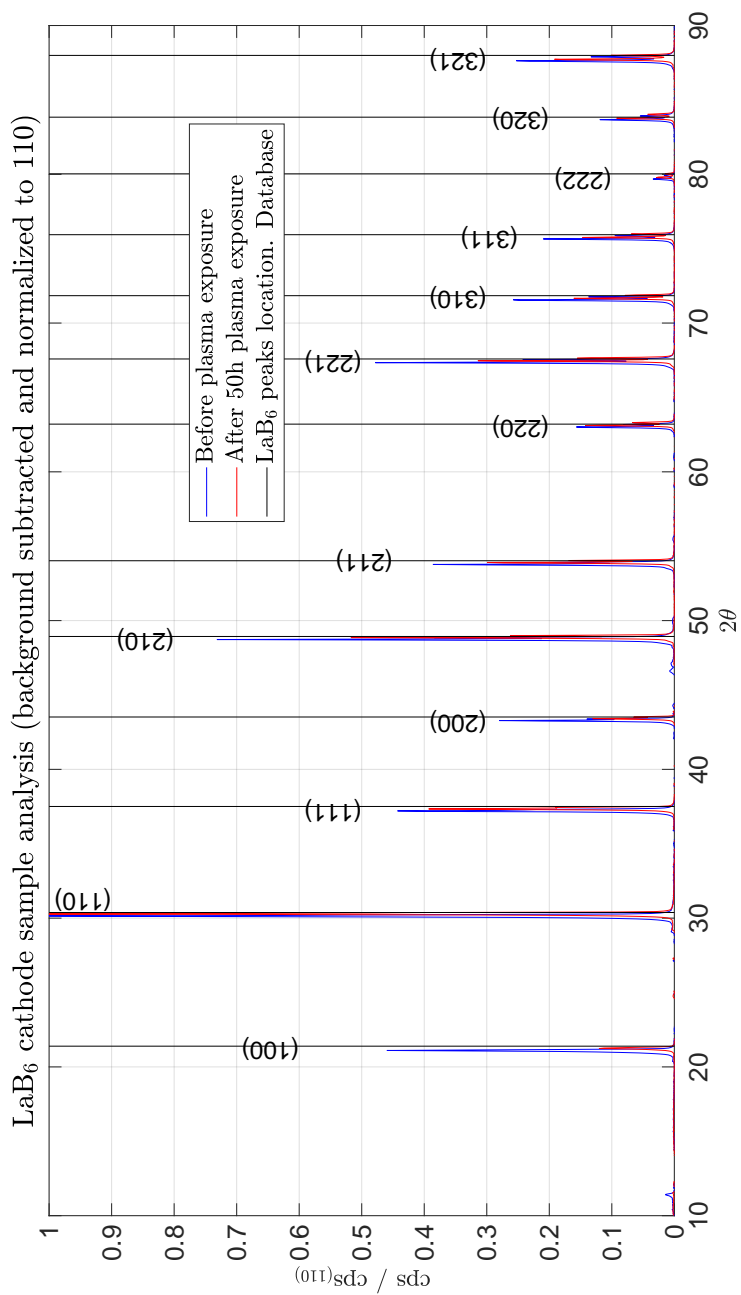


Figure 4.14: Work function measurements acquired with UPS.

Figure 4.15: Test sample XRD spectra results. Comparison with LaB₄ database ICDD 00-024-1015

Figure 4.16: Test sample XRD spectra results. Comparison with LaB₆ database ICDD 00-006-0401

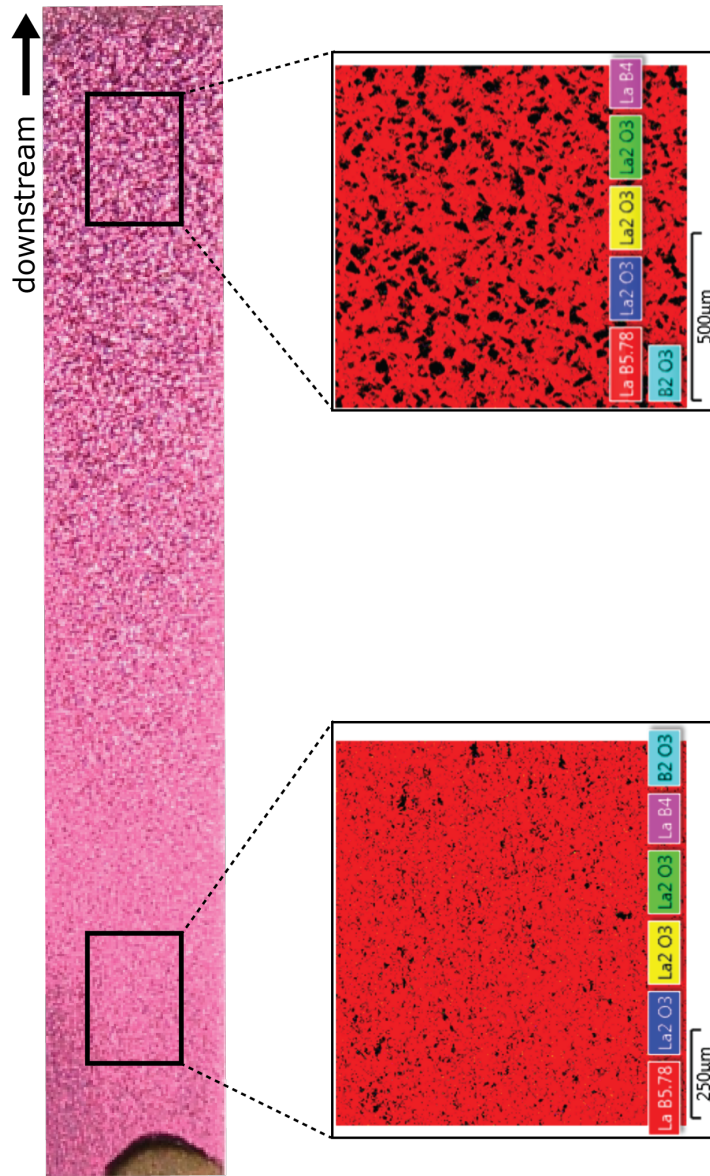


Figure 4.17: EBSD phase identification map of the sample in the upstream and downstream location of the test sample. The orientation of the test sample indicates the downstream end of the cathode (towards the orifice plate).

exposed and control areas of LaB₆ inserts by UPS (Fig. 4.14). First, it is important to note that all the measurements are above 3.3 eV, which is considerably higher than the value of 2.66 eV for polycrystalline LaB₆ obtained by Lafferty[4]. These differences are not unexpected given that in the work of Lafferty, work function was estimated using a LaB₆ sample in a vacuum cathode configuration at high temperature and results were extrapolated using the Richardson plot method. In contrast, we measured the photoemission work function by UPS of a LaB₆ sample at room temperature that has been exposed to the atmosphere. We propose that the observed differences in the absolute values of the work function measurements are likely due to adventitious carbon or oxidation of the surface from exposure to air after the experiment was concluded. Despite these differences, since putative atmospheric contaminants such as carbon are constant throughout the samples, the relative differences in work function measurements across the insert are still comparable.

The measurements for the control sample provided work functions ranging from 3.75 to almost 4.2 eV. However, in the case of the test sample, the work function measured at 15 locations along the emitter sample ranges from 3.3 to 3.86 eV. We believe this is a real trend in the work function of the sample, associated with exposure to Xe plasma. Consistent with this hypothesis, we note that the lowest values of the work function are found in the downstream region of the insert, about $\bar{z} \sim 0.8 - 0.9$. This is the region which was exposed to high density plasma and showed a faceted morphology, as can be seen in Fig. 4.11. It is reasonable to believe that the facets shown in Fig. 4.11 could correspond to the LaB₆ crystals which exhibit lower work function. Hence, the work function observed in the downstream end of the insert shown in Fig. 4.14 would be the effect of such texturing.

For each location, 5 apertures were used. The work function spread for each location can reach 0.15 eV in some of the measurements, and as small as 0.02 eV in other instances. It is unclear at this point the nature of this variability. In the sputtered gold sample, the range was 0.094 eV.

Crystallographic analysis by XRD

XRD showed that LaB_4 is not present in the crystalline form in the cathode sample before or after plasma exposure. However, it is possible that LaB_4 could be present in an amorphous state after the cathode cools. Nonetheless, amorphous substances are not faceted, as they lack lattice ordering. Given the faceted appearance of the downstream end of the insert surface in Fig. 4.11, we do not think that it is possible to find amorphous LaB_4 in this end of the cathode. Another possibility is that LaB_4 could be present while the cathode is running but it transitions to LaB_6 as the cathode cools down. The only locations where this might exist are in the crevices between the peaks shown in Fig. 4.11 and the upstream end of the insert. Fig. 4.18 shows a SEM picture of the surface, where crevices are easily distinguishable and hold an apparently amorphous substance. One possibility that explains the formation of amorphous substance in the crevices is quenching of melted material due to the fast cool down rates obtained at cathode shut down. The melting point of LaB_6 and LaB_4 are both above the cathode operating temperature, therefore, we do not believe this is the mechanism behind their formation. An alternative explanation is that the amorphous-looking structure in the crevices is not a sign of lack of crystallinity but is instead a result of ion etching. Crystals with high surface energy are more rapidly etched away than crystals with low surface energy (highly stable). The material in the valleys has lower chances of being impacted by returning plasma ions (as those ions can interact with the peaks on their way to the valleys) and therefore, it takes them longer to be etched away. If this mechanism is indeed the one occurring during the 50 hr test, it can explain the different temperature gradients observed in Chap. 2, Fig. 2.3 and Fig. 4.6.

The peaks before and after sample exposure to the cathode plasma are shifted relative to each other and do not align perfectly with the peak location from the database, see Table 4.1. Small shifts of this scale are either due to different stress states of the sample or lack of calibration in the instrument. The sample was manufactured by hot isostatic pressing (HIP) and after the exposure to the plasma the sample was subject to a fast cool down. It is then reasonable to believe that different stress states appear in the sample before and after plasma exposure, which could explain the peak shifts. Another feature worth mentioning is the double

Table 4.1: XRD diffraction peak location analysis. Table shows location values (in degrees) of XRD diffraction peaks for LaB_6 as reported in the literature, and as estimated in our measurements on the test sample before and after plasma exposure.

Crystal face	$PL_{\text{ICDD}}^{\text{mean}}$	$PL_{\text{ICDD}}^{\text{std}}$	PL_{bp}	PL_{ap}	$E(PL_{\text{bp}})$	$E(PL_{\text{ap}})$
(100)	21.37	0.0206	21.15	21.24	-0.220	-0.133
(110)	30.38	0.0035	30.15	30.28	-0.233	-0.103
(111)	37.46	0.0358	37.21	37.34	-0.255	-0.125
(200)	43.52	0.0069	43.28	43.41	-0.236	-0.106
(210)	48.95	0.0187	48.73	48.86	-0.224	-0.094
(211)	54.00	0.0173	53.77	53.91	-0.233	-0.093
(220)	63.22	0.0097	63.02	63.11	-0.197	-0.107
(221)	67.57	0.0166	67.34	67.50	-0.228	-0.068
(310)	71.78	0.0497	71.56	71.66	-0.223	-0.123
(311)	75.88	0.0514	75.65	75.75	-0.230	-0.130
(222)	79.92	0.0916	79.68	79.78	-0.243	-0.144
(320)	83.85	0.0075	83.67	83.77	-0.177	-0.077
(321)	87.86	0.1144	87.63	87.73	-0.229	-0.129

$PL_{\text{ICDD}}^{\text{mean}}$: peak intensity mean value based on ICDD_{006_0401}, ICDD_{034_0427} and ICDD_{065_1831}

$PL_{\text{ICDD}}^{\text{std}}$: peak intensity standard deviation value based on ICDD_{006_0401}, ICDD_{034_0427} and ICDD_{065_1831}

PL_{bp} : peak location before plasma exposure

PL_{ap} : peak location after plasma exposure

$E(PL_{\text{bp}}) = PL_{\text{bp}} - PL_{\text{ICDD}}^{\text{mean}}$

$E(PL_{\text{ap}}) = PL_{\text{ap}} - PL_{\text{ICDD}}^{\text{std}}$

peaks that appear at some peak locations, for example, in Fig. 4.19 at the (111) crystal location. This is most likely due to the lack of perfect monochromatic X-ray emission by the XRD X-ray source combined with the long integration times.

In Fig. 4.19 we show the comparison of the intensities of the three most significant crystal orientations in the XRD analysis for the sample before and after plasma exposure along with the three best quality database points we could find for LaB_6 in the ICDD database. Each set has been normalized to the peak

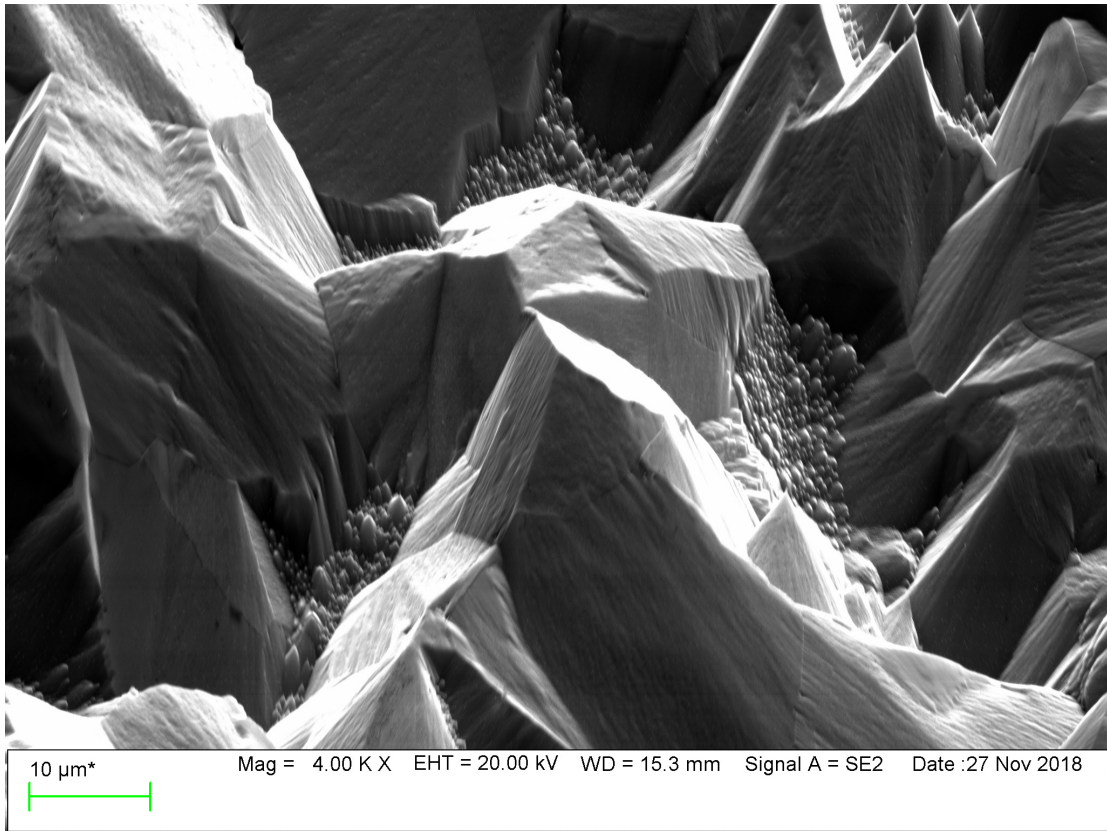


Figure 4.18: SEM picture of the test sample at the downstream end.

intensity of its own (110) peak. The XRD relative intensities between peaks for a powder sample that show no texture is a fingerprint for each material.

The relative intensity between crystals (111) and (100) based on data from the ICDD database is $I_{\text{ICDD}}^{\text{mean,(111)}}/I_{\text{ICDD}}^{\text{mean,(100)}} = 0.71$ (see Table 4.2), for the test article case prior to exposure is $I_{\text{bp}}^{(111)}/I_{\text{bp}}^{(100)} = 0.96$ and after is $I_{\text{ap}}^{(111)}/I_{\text{ap}}^{(100)} = 3.3$. The discrepancy of this ratio for the test sample before exposure is 36 % relative to the mean relative intensity from the ICDD data. In the case of the sample after the exposure it is 361%. The difference in this ratio between the sample after exposure and the ICDD data is a consequence of the development of a non random crystal distribution at the surface of the sample, in other words, a texture has developed. Similar results can be found by examining the rest of the XRD spectrum.

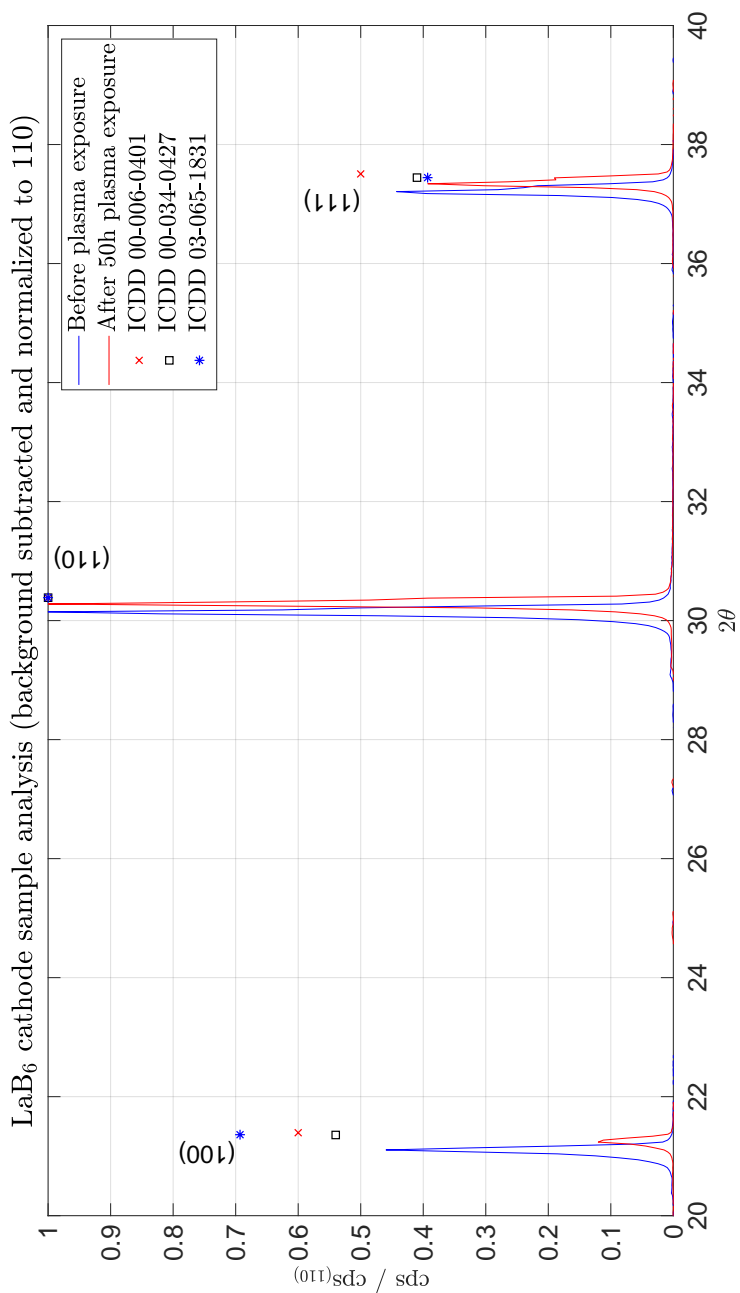


Figure 4.19: Test sample XRD spectra results. Intensity comparison.

Table 4.2: XRD diffraction peak intensity analysis. Table shows intensity values of XRD diffraction peaks for LaB₆ as reported in the literature, and as estimated in our measurements on the test sample before and after plasma exposure.

Crystal face	$I_{\text{ICDD}}^{\text{mean}}$	$I_{\text{ICDD}}^{\text{std}}$	$R_{\text{ICDD}}^{(100)}$	$\frac{I_{\text{bp}}}{I_{\text{bp}}^{(100)}}$	$\frac{I_{\text{ap}}}{I_{\text{ap}}^{(100)}}$	$E\% \left(\frac{I_{\text{bp}}}{I_{\text{bp}}^{(100)}} \right)$	$E\% \left(\frac{I_{\text{ap}}}{I_{\text{ap}}^{(100)}} \right)$
(100)	0.61	0.077	1.00	1.00	1.0	0	0
(110)	1.00	0.000	1.64	2.18	8.3	33	410
(111)	0.43	0.058	0.71	0.96	3.3	36	361
(200)	0.20	0.015	0.33	0.61	1.1	83	226
(210)	0.45	0.012	0.73	1.59	4.3	116	490
(211)	0.24	0.014	0.39	0.85	2.5	119	544
(220)	0.09	0.013	0.14	0.34	1.2	145	747
(221)	0.22	0.015	0.35	1.05	2.6	197	644
(310)	0.16	0.009	0.25	0.57	1.3	123	429
(311)	0.10	0.007	0.16	0.46	1.2	191	680
(222)	0.03	0.013	0.04	0.07	0.2	81	491
(320)	0.07	0.013	0.11	0.26	0.8	141	613
(321)	0.12	0.010	0.20	0.55	1.6	180	710

$I_{\text{ICDD}}^{\text{mean}}$: peak intensity mean value based on ICDD_{006_0401}, ICDD_{034_0427} and ICDD_{065_1831}

$I_{\text{ICDD}}^{\text{std}}$: peak intensity standard deviation value based on ICDD_{006_0401}, ICDD_{034_0427} and ICDD_{065_1831}

I_{bp} : peak intensity before plasma exposure

I_{ap} : peak intensity after plasma exposure

$$E(X) = \left(\frac{X - R_{\text{ICDD}}^{(100)}}{R_{\text{ICDD}}^{(100)}} \right) \times 100$$

$$R_{\text{ICDD}}^{(100)} = I_{\text{ICDD}}^{\text{mean}} / I_{\text{ICDD}}^{\text{mean},(100)}$$

EBSD

In the downstream area analysed (see Fig. 4.17), there is a higher portion of the data points (black areas on the image) that do not match any of the six crystalline structures listed, compared to the portion exhibit on the upstream area. There are three possible explanations for this phenomena: first, the pattern could belong to a crystalline phase that we are not aware of, and therefore, we are not comparing it with the correct pattern set from the database; second, there is no pattern due

to the presence of an amorphous substance at the surface. Third, this data could be due to the lack of flatness that we observed in the morphology of the surface on the downstream end of the sample, see Fig. 4.18. In this case, the Kikuchi patterns exist but cannot reach the EBSD detector, either because they are out of focus, or because the projection lies outside the detection area of the apparatus. We do not think the amorphous hypothesis is correct because the amorphous patches that appear in the crevices of the sample have a characteristic length on the order of $\sim 5\ \mu\text{m}$ and the size of the unidentified regions in the EBSD image data is on the other of $\sim 50\ \mu\text{m}$. We believe the effect of the surface morphology on the back-scattered pattern is the most promising explanation. The fact that the upstream map contains significantly fewer data points without match compared to the downstream one and the correlation with surface roughness, suggest that the change in morphology is behind the increase of unidentifiable data-points.

Morphology

The observed roughness at the downstream end of the insert suggests that the effective emissive area has increased. Cathode operating temperature depends on the total thermionic emission for the given cathode operating point, which in turn depends on the size of the emitting area. An increase in insert surface area could therefore result in a reduction of the cathode operating temperature. The change in temperature as a function of surface area is shown in Fig. 2.11, Chapter 2. To address the contribution of surface roughening to the observed lower operating temperature at steady state (Chapter 2), we sought to quantify the insert surface increase following plasma exposure. Based on the morphology at the roughest end of the insert observed by SEM, we assumed a simplified model where the surface is composed of square pyramids, see Fig. 4.20. The pyramid height (h in Fig. 4.20) is estimated from the distance between valleys and peaks detected by profilometry analysis Fig. 4.13. The maximum value for this distance is $12\ \mu\text{m}$. In order to dimensionalize the size of the pyramids (a in Fig. 4.20), we used the profile of the surface along line 3, Fig. 4.21. The profile of the downstream end of the insert

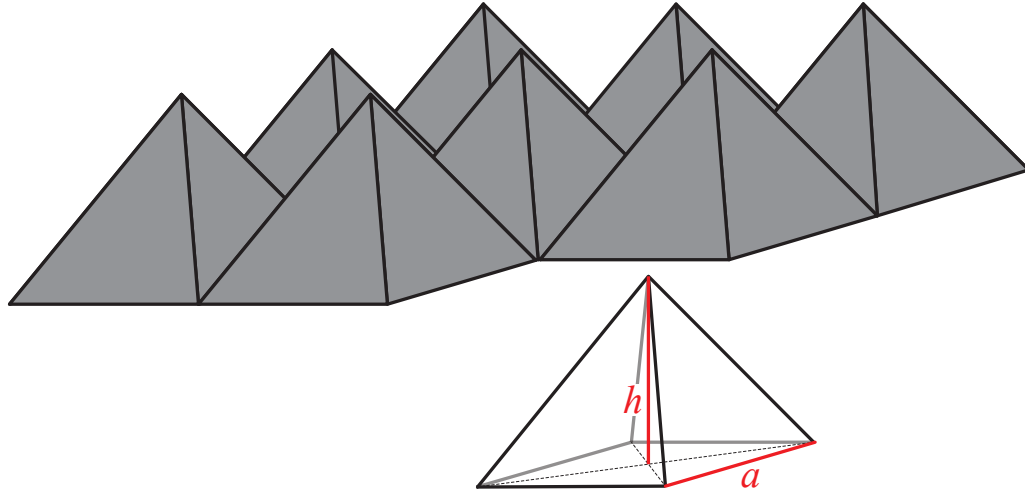


Figure 4.20: Idealized surface morphology for effective emissive area estimation

shows that the pyramids side length is bigger than $30\ \mu\text{m}$. Assuming $h=12\ \mu\text{m}$ and $a=30\ \mu\text{m}$, the surface area is 1.28 times the nominal area; $a=20\ \mu\text{m}$ and $h=15\ \mu\text{m}$ would result in a 1.8 times increase of the nominal area. The latter assumption is a large overestimation, especially given that sharp roughening is only present in the downstream end of the insert. As we showed in Chapter 2, Fig. 2.11, even when the effective area is doubled, the expected reduction of temperature is no more than $70\ ^\circ\text{C}$. Therefore, while surface roughening may contribute to lower operating temperatures, it cannot fully explain the cathode thermal behaviour at steady state.

4.6 Conclusions

Collectively, the temperature evolution of the LaB_6 hollow cathode and the work function measurements with UPS presented in this study suggest that 50 hr exposure to the internal plasma of a hollow cathode improves the work function of polycrystalline LaB_6 with respect to the work function of the material prior to the exposure. Specifically, the work function measurement was performed in the test article at room temperature after exposure to the atmosphere, which suggests

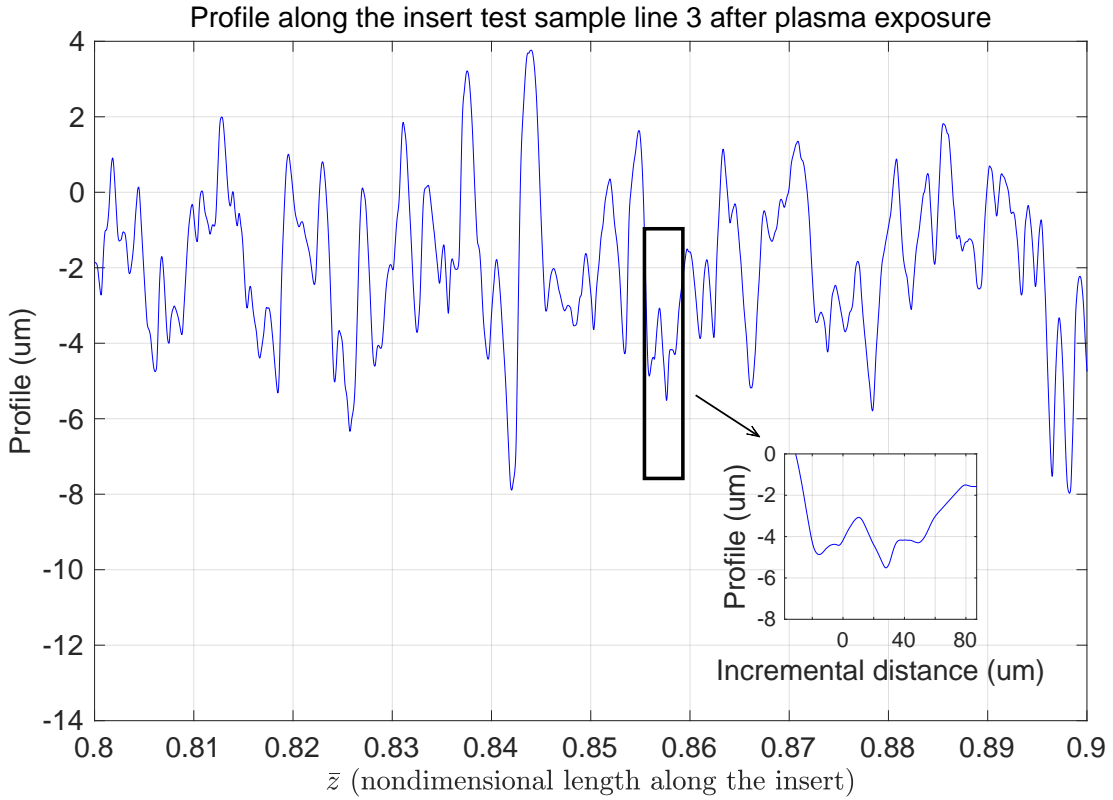


Figure 4.21: Test sample profile after plasma exposure along line 3

that the effect of the interaction of the plasma with the surface is permanent (the work function reduction is present even when the sample is not interacting with the plasma). The permanent reduction of the work function explains the different thermal transient behavior observed in our previous work [1] between a sample exposed to the plasma after manufacturing and a sample that has been exposed for a significant period of time.

In addition, we have learned that in the downstream end of the cathode, where the work function measured is the lowest, LaB_6 crystal faces have been exposed, as evidenced by SEM image of that area showing a faceted morphology. Furthermore, according to the XRD data Xe plasma creates a crystallographic texture at the LaB_6 surface. In summary, data showed that plasma-exposed insert surface consists of exclusively LaB_6 , displays a faceted morphology and a crystallographic texture,

and has a permanently reduced work function. Taken together, these results suggest that plasma-surface interaction induces a preferential exposure of LaB₆ crystal orientation associated with reduced work function (with respect to the vacuum value of 2.66 eV). From the thermodynamic point of view, given that those crystals survived the interaction with plasma ions, they should be among the most highly stable crystals of LaB₆. Therefore, we anticipate that these crystals correspond to the lowest surface energy crystals of LaB₆, which according to a DFT study [6] are the crystals which exhibit the lowest work function of the material. The results of our study are in agreement with that theory.

With respect to the presence of LaB₄ in the sample after plasma exposure, both EBSD and XRD analyses show no evidence of this compound. However, there is a possibility that LaB₄ exists while the cathode is in operation and it transitions to LaB₆ as the cathode cools down. In this work we cool down the cathode as fast as possible with the goal of freezing the chemistry at the surface of the insert. It will be of interest to model the kinetics of the transformation between LaB₄ and LaB₆ and compare it with the cool down rates of this work in order to understand the probability of the existence of LaB₄ prior to the cathode being shut down.

It is advisable to gain more insight into the La recycling hypothesis [1] in order to experimentally confirm that La gets recycled. In Fig. 2.6 (Chap. 2), we showed that short thermal transients occur as the operating condition of the cathode is changed. Since the timescale of these transients is only few minutes, it is unlikely that they are caused by the crystallographic evolution of the insert surface. However, these short transients could be explained by a dynamic redeposition of ionized lanthanum which depends on the transport of this species by the specifics of the plasma distribution for each operating point of the cathode. In this case, the forced cationic termination that the recycled La would exert in the crystals of LaB₆ could be behind the aforementioned short time scale thermal transients. Those terminations would not be stable without the constant recycling of La, as the naturally terminated boron crystals would reappear when the operating condition of the cathode changes the plasma structure in the internal domain of the cathode and therefore affect the recycling intensity. The formation of LaB₄ could also

explain the short thermal transients only if LaB_4 exhibits a lower work function than LaB_6 and at the same time, the kinetics of the transformation towards LaB_6 are on a short timescale, one that matches the observations of this discussion. Additional work should be done to confirm that La is effectively recycled in the insert plasma.

BIBLIOGRAPHY

- [1] Pablo Guerrero et al. “Work function reduction in lanthanum hexaboride hollow cathodes operated in gas discharges”. In: *35th International Electric Propulsion Conference*. Atlanta, GA, USA, 2017, pp. 2017–399. URL: https://iepc2017.org/sites/default/files/speaker-papers/iepc-2017_399.pdfhttp://erps.spacegrant.org/IEPC_2017/IEPC_2017_399.pdf (cit. on pp. 113, 114, 146, 147).
- [2] Robert G. Jahn and Edgar Y. Choueiri. “Electric Propulsion”. In: *Encyclopedia of Physical Science and Technology*. Vol. 5. 6. Elsevier, 2003, pp. 125–141. DOI: 10.1016/B0-12-227410-5/00201-5 (cit. on p. 113).
- [3] Dan M. Goebel and Ira Katz. *Fundamentals of Electric Propulsion: Ion and Hall Thrusters V0*. 2008, pp. 1–507. DOI: 10.1002/9780470436448 (cit. on p. 114).
- [4] J. M. Lafferty. “Boride Cathodes”. In: *Journal of Applied Physics* 22.3 (Mar. 1951), pp. 299–309. DOI: 10.1063/1.1699946 (cit. on pp. 114, 138).
- [5] Pablo Guerrero et al. “Hollow cathode thermal modelling and self-consistent plasma solution: work function evaluation for a LaB 6 cathode.” In: *AIAA-ASAE-ASEE Joint Propulsion Conference*. 2018 (cit. on p. 114).
- [6] M A Uijtewaal, G. A. de Wijs, and R. A. de Groot. “Ab Initio and Work Function and Surface Energy Anisotropy of LaB 6”. In: *The Journal of Physical Chemistry B* 110.37 (Sept. 2006), pp. 18459–18465. DOI: 10.1021/jp063347i (cit. on pp. 114, 115, 147).
- [7] Jian Wang et al. “Work functions of metal hexaborides: Density functional study”. In: *Modern Physics Letters B* 32.2 (2018), pp. 1–8. DOI: 10.1142/S0217984918500070 (cit. on p. 114).
- [8] S.A. Chambers et al. “Cesium and oxygen coadsorption on LaB6, single crystal surfaces”. In: *Surface Science* 118.1-2 (June 1982), pp. 75–92. DOI: 10.1016/0039-6028(82)90015-2 (cit. on p. 116).
- [9] R Thompson. “Production, Fabrication and Uses of Borides”. In: *The Physics and Chemistry of Carbides, Nitrides and Borides*. Ed. by Robert Freer. Dordrecht: Springer Netherlands, 1990, pp. 113–120. DOI: 10.1007/978-94-009-2101-6{_}8 (cit. on p. 116).

CONCLUSIONS AND FUTURE WORK

5.1 Conclusions

This thesis presents a comprehensive analysis of the thermal behavior of hollow cathodes with polycrystalline LaB₆ emitters operated in standalone configuration in vacuum.

We showed that these hollow cathodes exhibit transient behaviors that are not associated with the cathode plasma or thermal characteristics. Instead, these transient behaviors are associated with the chemical evolution of the electron emitter material, which affects the cathode plasma distribution and therefore the cathode thermal operation. This is a novel observation not previously reported in the literature, which opens a new paradigm on how hollow cathodes must be studied.

The transient behaviors are manifested in two distinct novel observations. First, when a newly manufactured electron emitter is used, the cathode exhibits a long timescale thermal transient (~50 hr) with a net effect of decreasing the operating temperature of the cathode until a stable thermal condition is obtained. Second, a shorter timescale thermal transient (~5-10 min) occurs when there is a change in the operating condition or the cathode is shut down and re-ignited. In this case, the transient depends on the depth of the cool-down before re-ignition. No previous knowledge of, or explanation for, these effects existed before this work was performed. We propose that these transients come from a chemical evolution of the cathode emitting surfaces due to the plasma impinging upon them. As a consequence of this chemical evolution, a reduction in the work function occurs.

In order to fully understand the thermal transients, the multiphysics nature of the hollow cathode was numerically simulated by combining plasma, thermal and chemical effects in a new platform. This platform integrates: a plasma solver

code OrCa2D that has been under development at JPL for about 15 years, and a novel 2D axisymmetric thermal model of the entire cathode which was developed using Comsol Multiphysics and has been experimentally validated for this work. Chemical and ion neutralization effects were input at the interface between both codes. Results suggested that the thermal loads from the cathode interior plasma were overestimated when the classically assumed mechanisms for the different physics were utilised. In particular, we identified that the neutralization model had a primary importance and should be reevaluated. We found that in order to find agreement between simulation results and the experimentally measured cathode operating conditions, a 2-step neutralization mechanism needs to be implemented. This neutralization model consists of resonant neutralization to the first excited state of Xe followed by Auger de-excitation to the Xe ground state. In addition, we studied the solution's dependence on both the energy accommodation factor and the work function variations along the insert. We concluded from these studies that the solution of the self-consistent cathode model is not perceptibly sensitive to work function variations. Finally, we quantified how much Auger emission and energy accommodation were necessary for the model to fit the empirical evidence.

For electric propulsion, this discovery means that LaB_6 used at the right operating point could exhibit a reduced working temperature, and therefore, greatly expand the lifetime of the hollow cathodes used for electric propulsion applications.

Lastly, in order to gain insight into the chemical mechanism behind the work function enhancement, we performed a series of experiments using a slightly modified electron emitter geometry to accommodate limitations imposed by the chemical analysis techniques. The analyses consisted of evaluating the chemical state of the emitter surface before and after exposure to the cathode plasma using ultraviolet photoelectron spectrometer (UPS), electron backscatter, and X-ray diffraction. The results from these analyses show that the cathode interior plasma improves the work function and that this enhancement is permanent. Additionally, we discovered the presence of a crystallographic texture to which we attribute the enhancement.

Together, this work provides an in-depth insight into the thermal behavior and effect of plasma exposure on polycrystalline LaB₆ inside a hollow cathode. Results revealing the unexpected phenomenon of work function enhancement upon plasma exposure on LaB₆ suggest that the LaB₆ hollow cathodes evaporation rates might be much lower than previously thought, and therefore their lifetime much longer. Given the importance of lifetime for EP components, LaB₆ might outperform current technologies and become the component of choice in EP thrusters for future space missions.

5.2 Future work

Although this thesis has demonstrated that thermal transients associated with chemical evolution of thermionic emitters in the hollow cathode configuration exist, and that they are most probably due to a mixture of crystallographic texturing and forced cationic termination,

- the lanthanum recycling hypothesis should be further investigated. There is no empirical evidence so far as to whether La is actually recycled in the interior plasma of a hollow cathode. Mass spectrometry and cavity ring down spectroscopy offer the potential to provide a deeper insight into this mechanism. With these techniques, it would be possible to detect the density of La inside the cathode. The existence of a La recycling mechanism can be tested experimentally by measuring enrichment of La in the inner region of the cathode and reduction of La density on the plume region as the cathode discharge is enabled.
- if lanthanum is indeed recycled, numerical simulations that explain the transport of this species inside the complex inner region of the cathode are needed to determine the flux of La coming back to the emitting surface of the insert. With those results, La return flux and coverage information could explain the observed short-term thermal transients and unexpected behavior when the cathode is shut down and re-ignited.

- the mechanism that produces the crystallographic texture should be further studied because it can be used in other polycrystalline materials to improve their behavior. The evidence presented in this work suggests that ions with energy below the sputtering threshold of the material against which they impinge can improve the work function of a polycrystalline sample and bring its performance close to that of single-crystal cathodes. This mechanism could be used to produce cheap enhanced thermionic emitters which are of interest across several industries.
- identification of the crystals preferentially exposed by the action of the plasma (texture) should be achieved as this information can be used to prove the relation between low work function and low surface energy crystal faces for LaB_6 . We could not find any technique that could straightforwardly provide us with such information. However, a more involved technique, such as extracting the surface grains with focus ion beam (FIB) and orienting them appropriately for electron backscattering diffraction (EBSD), could potentially aid in crystal identification. Additionally, it would be useful to obtain the orientation distribution function (ODF) using an XRD with sample-tilt capability. The ODF can identify the enriched crystal at the surface of flat and polished samples. However, plasma produces a rough surface, which increases the difficulty to obtain the ODF. To address this limitation, an XRD with parallel beam geometry should be considered.
- the energy accommodation coefficient (EAC) should be experimentally measured for the system $\text{LaB}_6\text{-Xe}$ in an environment similar to the one that exists in the interior of the cathode. Temperature of the LaB_6 target, ion incident angle and energy at impact should all be controlled in such an experiment. The motivation for this future work resides on the need to find the correct EAC to model cathodes operating at different conditions than the study in this work.
- the two step neutralization model for the ion-surface interaction should be experimentally confirmed for the system $\text{LaB}_6\text{-Xe}$ with an environment

similar to the one that exists in the interior of the cathode. The motivation for this future work is the same as for the EAC previously explained.

- efforts to achieve a better validation of the plasma modelling techniques should continue. We believe that uncertainty quantification could help in understanding the sensitivity on the thermal fluxes of the different parameters needed as inputs into the plasma model. Additionally, it would be of interest to study a cathode operating condition at which the heat fluxes are dominated by the electron return current (ion heat flux negligible). Such operating condition would be basically insensitive to the EAC. This type of operating condition can be found at high discharge currents where the insert sheath voltage is low.